

Designing Nano-Structural Composites as Advanced Anode Materials for Highly Efficient and Stable Lithium-ion Batteries

by

Elhadi Attia

A thesis

presented to the University of Waterloo

in fulfillment of the

thesis requirement for the degree of

Doctor of Philosophy

in

Chemical Engineering

Waterloo, Ontario, Canada, 2021

© Elhadi Attia 2021

Examining Committee Membership

The following served on the Examining Committee for this thesis. The decision of the Examining Committee is by majority vote.

External Examiner	Dr. Jiangning Wu Professor Department of Chemical Engineering, Ryerson University
Supervisor	Dr. Zhongwei Chen Professor Department of Chemical Engineering, University of Waterloo
Supervisor	Dr. Ali Elkamel Professor Department of Chemical Engineering, University of Waterloo
Internal-external Member	Dr. William Melek Professor Department of Mechanical and Mechatronic Engineering, University of Waterloo
Internal Member	Dr. Peter Douglas Professor Department of Chemical Engineering, University of Waterloo
Internal Member	Dr. Eric Croiset Professor Department of Chemical Engineering, University of Waterloo

Author's Declaration

This thesis consists of material all of which I authored or co-authored: see Statement of Contributions included in the thesis. This is a true copy of the thesis, including any required final revisions, as accepted by my examiners.

I understand that my thesis may be made electronically available to the public.

Statement of Contributions

The body of this thesis is based upon a combination of published work and manuscript under submission. Different chapters are adapted from the following list of publications.

Chapter 4 of this thesis consists of a paper published that was co-authored by myself, my supervisors, a post-doctoral fellow, Dr. F. Hassan and two PhD students, Matthew Li and Rasim Batmaz. I am the first author of this paper. Dr. Hassan and I designed the experiments. I carried out the experiments, collected and analyzed the data. Dr. Hassan helped with discussing the results and writing the manuscript. Matthew helped with some characterization and proofreading the manuscript. Rasim assisted with some electrochemical measurements.

“Tailoring the Chemistry of Blend Copolymers Boosting the Electrochemical Performance of Si-Based Anodes for Lithium-ion Batteries”, *J. Mater. Chem. A*, 2017, 5, 24159.

Chapter 5 of this thesis consists of a paper published that was co-authored by myself, my supervisors, a post-doctoral fellow, Dr. F. Hassan and PhD students, Matthew Li and Dan Lou. I am the first author of this paper. With Dr. Hassan’s help, I performed all the experiments, collected and analyzed the data, as well as wrote the manuscript. Dr. Hassan helped with discussing the results. Matthew helped with proofreading the manuscript. Dan assisted with some electrochemical measurements.

“Multifunctional Nano-Architecting of Si Electrode for High-Performance Lithium-ion Battery Anode”, *Journal of The Electrochemical Society*, **166** (13) A2776-A2783 (2019).

Chapter 6 of this thesis consists of an unpublished paper that was co-authored by myself, my supervisors, Dr. F. Hassan, Dr. Drew Higgins, and Matthew Li. I am the first author of this work, and Dr. Hassan provided general advice for this project. I performed all the experiments, collected and analyzed the data, as well as wrote the manuscript. Matthew helped with proofreading the manuscript. Dr. Drew Higgins helped with the TEM analysis and proofreading.

“Grape Wrapped by Graphene: A new Concept for Smart Anode Design for Anti-aging Lithium-ion Batteries”, under preparation for submission.

Abstract

With the continued increase in energy demand for portable electronics, grid storage, and electric vehicles, more attention is being placed on the development of advanced energy conversion and storage systems such as metal ion batteries and fuel cells. Recently, lithium-ion batteries (LIBs) have dominated the electronic applications market such as consumer electronics, power tools, and medical devices. Moreover, LIBs have been used in the transportation sector in electric vehicles (EV) and electric bicycles. High capacity retention and long cycle life are essential, especially for the EV market. However, due to the limited energy density and high cost of large LIBs packs, the current battery technology is not satisfactory for the widespread application in EVs. Therefore, development of battery technology with high-energy density and low-cost materials can lead to significant improvements in the performance and lifetimes of products that use LIBs.

To improve the energy density of LIBs, conventional anode materials (graphite) need to be replaced by novel electrode materials and improved electrode designs with a higher capacity and more reliable performance. Silicon (Si) is an exciting and promising candidate for use as active material in the negative electrode to develop the next generation LIBs due to its natural abundance, high safety, low-cost, environmentally friendliness, and high theoretical specific capacity reaching 4200 mAh g^{-1} compared with 372 mAh g^{-1} of graphite. However, the critical challenge with Si is the huge volume changes during the lithiation and delithiation processes, which causes mechanical fractures and delamination of the electrode. In addition, solid electrolyte interphase (SEI) formation disrupts the electrical contact between Si particles during cycling, which lead to

degradation of the electrode and rapid capacity fading. These issues limit the wide commercialization of Si as anode material for LIBs.

In this thesis work, different categories of advanced nanostructure materials have been designed and developed to serve as a conductive network for nanostructured Si morphologies with high capacity and better mechanical stability to enable the evolution of the next generation of LIBs. This thesis starts with a brief introduction to LIBs, followed by the objectives and approaches taken in this PhD project. A literature review on the main battery components and the operation principles of rechargeable LIBs with a focus on the development of the electrode materials will be discussed. A survey of the experimental procedures, characterization techniques, and performance testing procedures are provided. Specific research projects are proposed, and specifically demonstrated in the projects presented in this thesis. This will provide readers with a comprehensive overview of the field of study, and detailed project plans in order to successfully develop novel advanced electrode materials for high energy density and reliable rechargeable LIBs.

The first approach of my PhD thesis is focused on developing flexible and conductive carbon networks to improve the stability of Si-based anodes. At this stage, we have designed a polymer blend of polyvinylpyrrolidone (PVP) and polyacrylonitrile (PAN) which was self-assembled onto the surface of Si nanoparticles (SiNPs) allowing for the generation of a very intimate coating of Si dioxide and nitrogen-rich carbon shell upon slow heat treatment. This methodology capitalizes on the surface interaction of PVP with SiNPs to provide a sturdy nanoarchitecture. The addition of PVP improves the stability and adhesion of PAN to the carbon-based matrix which surrounds the Si particles, leading to enhance the stability of the Si anode. In addition to being a very scalable

fabrication process, our novel blend of PVP and PAN allowed for an electrode with high reversibility. When compared with a standard electrode Si/PVDF framework, this material of PVP/PAN demonstrated a significantly superior first discharge capacity of 2736 mAh g⁻¹, high Coulombic efficiency, and excellent rate capability, as well as excellent cycle stability for 600 cycles at a high rate of 3000 mA g⁻¹.

Even though we achieved considerable improvements to the Si-based anode, we still need to improve the electrode capacity with long cycle stability and high areal capacity. In the second part of this thesis, a multifunctional composite binder was developed by cross-linking a poly(acrylic acid) (PAA) and carboxymethyl cellulose (CMC) spine with PAN through a slow heat treatment process. The composite binder strongly interacts with Si, providing a sturdy structure with efficient pathways for both Li-ion and electron transport. The cross-linked carboxyl groups from PAA and CMC offered a robust 3D cross-linked network, anchoring SiO₂ coated Si nanoparticles onto a highly-porous carbon scaffold, forming stable a solid electrolyte interphase. This composite anode not only exhibits a high initial capacity of 3472.6 mAh g⁻¹ with an initial Coulombic efficiency of 89.1%, but also provides excellent cycling stability for 650 cycles at a high current density of 3000 mA g⁻¹.

While excellent rate performance and dramatic enhancement of Si-based anode were obtained using cross-linking of CMC-PAA with g-PAN, we looked to further improve the cycle life with high capacity using reinforcement additives. In the last part of this thesis, a novel multi-leveled design of webs-like morphology is reported as a robust and highly stable 3D interconnected network to mass-produce nanostructured Si composite anode. This sturdy composite consisting of nano-size Si particles (NSi), nitrogen-doped carbon nanotubes (N-CNTs), and graphenized

polyacrylonitrile (g-PAN) is prepared via a simple and low-cost method as a negative electrode for LIBs. The NSi@N-CNT/g-PAN composite integrates the benefits from its components, where NSi-interactive materials deliver high capacity, N-CNTs with nitrogen functionalizations act as electron highways and flexible network to connect NSi particles, and g-PAN with nitrogen-rich provides nitrogen-doped graphene sheets, which wrapped the whole structure network of NSi@N-CNTs. The stable interaction between the Si particles and N-CNTs enhances electron transport, while g-PAN effectively improves the capacity and conductivity of the whole electrode and provides a porous skeleton allowing convenient ion diffusion leading to longevity in battery operations. We found that only when all three components are introduced will significant enhancement in performance be observed. This nanocomposite anode exhibits superior cycling stability with a reversible capacity of $\sim 1361 \text{ mAh g}^{-1}$ for a remarkably long-life of 1100 cycles when cycled at a high current density of 3000 mA g^{-1} . Moreover, high loading cycling of up to 3 mAh cm^{-2} at $\sim 1 \text{ mgSi cm}^{-2}$ was achieved at a current density of 500 mA g^{-1} . This effective strategy could potentially be applied to prepare large-scale production of a high-performance electrode for LIBs.

Acknowledgements

I would like to express the greatest appreciation to my supervisors, Professor Zhongwei Chen and Professor Ali Elkamel, for their meticulous guidance and tremendous assistance throughout my PhD studies as well as for giving me the freedom to pursue my own ideas in this thesis.

I would like to thank my supervisor Professor Chen for giving me the opportunity to join his group and to learn more about electrochemistry, lithium-ion batteries, and energy storage.

I would like to express my great thanks to Dr. Fathy Hassan for his time, effort, and valuable discussions. Thank you for the fruitful discussions and advice whenever it was required.

I would also like to thank Professor Jiangning Wu, Professor William Melek, Professor Peter Douglas, and Professor Eric Croiset for being my Ph.D. examining committee members and for their time and effort.

Also, thanks to our group members such as Matthew Li, Dan Lou, Rasim Bazam, and Pan Xu for their support and assistance.

I am also grateful to the administrative staff in the Chemical Engineering department who helped me with any administrative issues.

Special thanks to my family, wife and my kids for their patience and support.

Finally, I would like to acknowledge the financial support of the Ministry of Higher Education and Scientific Research, Libya for providing five years Doctoral Scholarship.

Table of Contents

Examining Committee Membership.....	ii
Author’s Declaration	iii
Statement of Contributions	iv
Abstract.....	vi
Acknowledgements.....	x
List of Figures.....	xiii
List of Tables	xix
List of Abbreviations	xx
Chapter 1: Introduction	1
1.1 Motivation and Challenges.....	1
1.2 Thesis Objectives and Approaches.....	3
1.3 Thesis Outlines	5
Chapter 2: Background and Literature Review.....	8
2.1 Battery Technology	8
2.2 Lithium-ion Batteries.....	9
2.3 Cathode Materials.....	12
2.3.1 Layered Structure	13
2.3.2 Spinel Structure	13
2.3.3 Olivine Structure	14
2.4 Anode Materials	15
2.4.1 Lithium Anode	15
2.4.2 Graphite Anode	16
2.4.3 Silicon Anode.....	17
2.5 Electrolytes for Li-ion Batteries	20
2.6 Binders for Li-ion Batteries.....	21
Chapter 3: Characterization Techniques	24
3.1 Morphological and Compositional Analyses	24
3.1.1 Scanning Electron Microscopy	24
3.1.2 Transmission Electron Microscopy.....	25
3.1.3 Energy Dispersive X-ray Spectroscopy.....	25
3.1.4 X-ray Diffraction.....	26

3.1.5 X-ray Photoelectron Spectroscopy	27
3.1.6 Raman Spectroscopy	27
3.1.7 Differential Scanning Calorimetry	28
3.2 Electrochemical and Performance Characterization.....	29
3.2.1 Fabrication of Coin Cell	29
3.2.2 Charging and Discharging Processes	30
3.2.3 Cyclic Voltammetry	30
Chapter 4. Tailoring the Chemistry of Blend Copolymers Boosting the Electrochemical Performance of Si-based Anodes for Lithium-ion Batteries	31
4.1 Introduction	31
4.2 Experimental Section.....	33
4.3 Results and Discussion	35
Chapter 5. Multifunctional Nano-Architecting of Si Electrode for High-Performance Lithium-Ion Battery Anode.....	51
5.1 Introduction	51
5.2 Experimental Work.....	53
5.2.1 Preparation of Si Electrode:	53
5.3 Results and Discussion	54
Chapter 6. Grape Wrapped by Graphene: A new Concept for Smart Anode Design for Anti-aging Lithium-ion Batteries	73
6.1 Introduction	73
6.2 Experimental Section.....	76
6.2.1 Synthesis of N-doped CNT	76
6.2.2 Fabrication and Testing of Composite Electrodes.....	76
6.3 Results and Discussion	77
Chapter 7. Conclusions and Future Work.....	101
7.1 Conclusion and Summary.....	101
7.2 Suggestions for Future Work.....	104
References.....	107
Appendix A:.....	117

List of Figures

Figure 1.1 Schematic illustration of the thesis workflow.....	7
Figure 2.1 Diagram comparing the volumetric and gravimetric energy densities of several common energy storage technologies.....	9
Figure 2.2 A schematic illustrations of the operation principle of a conventional lithium ion battery.....	12
Figure 2.3 A schematic illustration of the layered structure of LiMO_2	13
Figure 2.4 A schematic illustration of spinal structure of spinel, LiMn_2O_4	14
Figure 2.5 A schematic illustration of olivine structure, LiFePO_4	15
Figure 2.6 A schematic illustration of the graphite crystal structure with the the graphene sheets stacking and the unit cell.....	16
Figure 2.7 Comparing the gravimetric and volumetric capacities of different anode materials	18
Figure 2.8 Schematic of volume change of silicon particle and the failure mechanism of silicon nanoparticles during cycling and unstable SEI formation.....	19
Figure 3.1 Illustration of the Bragg's law	26
Figure 3.2 Diagram of energy level showing the states involved in Raman signal	28
Figure 3.3 Schematic showing the coin cell (type 2032) components.....	29
Figure 4.1 The materials slurry before and after casting on the copper foil.....	36
Figure 4.2 A schematic showing the fabrication procedure of the electrode: (a) synthesis of the electrode from SiNP, PVP, PAN, and GO before coating on Cu foil, (b) electrode before SHT, (c) SHT process, and (d) electrode after SHT.. ..	36
Figure 4.3 (a-b) TEM image of Si particles coated of PVP, (C) a schematic of PVP layer coated the Si particle, (d-f) TEM images of the Si/PVP/PAN electrode before SHT, (g-i) TEM images of the Si/PVP/PAN electrode treated at 450 °C, and (j-l) TEM images of the Si/PVP/PAN electrode treated at 750 °C.	36
Figure 4.4 (a) Higher magnification TEM image of several SiNPs before SHT, (a1-a3) corresponding elemental mapping of Si, C and O of the area selected in the image (a), (b) TEM image of the electrode surface treated at 450 °C, (b1-b3) corresponding EDS mapping of Si, C, and O of the image (b), (c) TEM image of Si particles treated at 750 °C, (c1-c3) corresponding EDS mapping of Si, C, and O of the area marked in the image (c), (d) EELS elemental mapping of Si (red), C (green), and O (blue), (d1-d3) the elements mapping by EELS for the area selected in the image (c), (e) high-resolution XPS of Si 2p spectra of the electrode materials before and after SHT, and (f) a schematic showing the core Si particle with the surrounding layers of SiO_2 and N-doped graphene.....	37

Figure 4.5 DSC analysis of the electrode materials, pure PVP, pure PAN, PVP/PAN, and Si/PVP/PAN in nitrogen.....	40
Figure 4.6 Raman spectrum of three electrode materials, Si/PVP/PAN-untreated, Si/PVP/PAN treated at 450 C, and Si/PVP/PAN treated at 750 C.....	42
Figure 4.7 High-resolution XPS spectra of the electrode materials for (a) C 1s and (b) N 1s, and (e) schematic of the cyclization mechanism for PAN.....	42
Figure 4.8 Electrochemical characterization of the Si electrodes: (a) CV curve for a coin cell was treated at 750 °C and measured at scan rate of 0.05 mV s ⁻¹ between 0.01 and 1.5 V (vs Li ⁺ /Li), (b) Cycling stability of the electrodes treated at 450 and 750 oC at 100 mA g ⁻¹ and 500 mA g ⁻¹	43
Figure 4.9 Electrochemical characterization of the Si electrodes: (a) Rate capability of the electrodes treated at 450 and 750 °C, (b) voltage profile of Si electrode treated at 450 C and tested at different current rates....	45
Figure 4.10 Electrochemical impedance measurements of the Si/PVP/g-PAN treated at 450 and 750 C, Si/PVP/PAN non treated, and Si/PVDF/Super P after 50 cycles.....	46
Figure 4.11 Cycling behavior of the Si/PVP/PAN electrodes treated at 450 and 750 °C at 100 mA g ⁻¹ for the first five cycles and 2000 mA g ⁻¹ for the following cycles with Si/PVDF/Super P.....	48
Figure 4.12 Long-term cycling stability of Si/PVP/PAN treated at 750 °C and cycled at 100 mA g ⁻¹ for five cycles and at 3000 mA g ⁻¹ for another 600 cycles.....	49
Figure 4.13 Characterization of the electrode material before and after cycling for 600 cycles: (a) HRTEM image of the surface electrode treated at 750 °C and before cycling with corresponding to the elements (O, C, N, and Si) mapping by EELS for the area marked in the image (a), and (b) HRTEM image of the electrode after cycling corresponding EELS mapping of the elements (O, C, and Si) for the area marked in the image (b).....	50
Figure 5.1 A schematic illustration of the design procedure of the nanostructured electrode materials; (a) NSi particles covered by PAA/CMC layer after freeze-drying, (b) NSi/PAA/CMC covered by PAN polymer before SHT process, (c) cross-linking of PAA-CMC <i>via</i> the condensation reaction between CMC and PAA. Covalent binding between PAA-CMC binder and NSi is formed during the SHT process; (d) graphenization of PAN during the SHT, and (e) NSi/PAA-CMC/g-PAN composite after SHT process.....	55
Figure 5.2 A Schematic showing optical images for the electrode surface before and after the slow heat treatment.....	55
Figure 5.3 (a) TEM image of pure Si nanoparticles, (b) HRTEM image of the crystalline Si particle before coating with size of 50 to 70 nm showing a thin layer of SiO ₂	57
Figure 5.4 (a) TEM image of SiNPs covered by PAA/CMC polymers after freeze-drying, (b,c) HRTEM images of close Si particles wrapped by PAA/CMC layer, (d) TEM image of Si particles coated by	

PAA/CMC with PAN before the TIN, (e,f) HRTEM images of the NSi/PAA/CMC/PAN before SHT, (g) TEM image of NSi/PAA-CMC/g-PAN after SHT showing the Si particles wrapped by graphene nanosheets, and (h,i) HRTEM images of SiNPs coated by SiO ₂ layer and graphenized PAN.....	59
Figure 5.5 (a) HAADF-STEM image of the NSi/PAA/CMC/PAN material before SHT with its corresponding EELS mapping of (C, Si, O, and overlap elements) for the area selected in the red square in (a), (b) STEM image of NSi/PAA-CMC/g-PAN material after SHT with its corresponding EELS mapping for (C, Si, O, N and overlap elements), (c) a schematic illustration the composite layers around the SiNPs.....	60
Figure 5.6 FTIR spectra of the composite materials, CMC, PAA, CMC-PAA, NSi/PAA-CMC/PAN, and NSi/PAA-CMC/g-PAN.....	62
Figure 5.7 DSC analysis of the composite materials, CMC, PAA, PAN, and NSi/PAA-CMC/g-PAN.....	62
Figure 5.8 High-resolution XPS spectra of the composite materials at different stages: (a) C 1s, (b) Si 2p, and (f) N 1s.....	63
Figure 5.9 (a) Discharge/charge voltage profile of the NSi/PAA-CMC/g-PAN electrode tested at 100 and 500 mA g ⁻¹ , (b) the corresponding cycling stability of the NSi/PAA-CMC/g-PAN electrode.....	65
Figure 5.10 (a) Rate capability test of the NSi/PAA-CMC/g-PAN electrode at different current rates, (b) areal capacity for the NSi/PAA-CMC/g-PAN electrode with Si mass loading of 1.2 mg cm ⁻²	66
Figure 5.11 (a) Cycling voltammetry curves of a coin-type half-cell of the NSi/PAA-CMC/g-PAN, (b) EIS test of the NSi/PAA-CMC/g-PAN in comparison with the non-treated NSi/PAA/CMC/PAN and NSi/PAA/CMC treated at 450°C.....	67
Figure 5.12 Long-term cycling stability for the electrodes of NSi/PAA-CMC/g-PAN, non-treated NSi/PAA/CMC/PAN, and NSi/PVDF/Super P tested at current rates of 100 and 2000 mA g ⁻¹ for the first six cycles and 3000 mA g ⁻¹ for the subsequent cycles.....	69
Figure 5.13 Cycling behavior of the reference electrodes compared to our electrode of NSi/PAA-CMC/g-PAN (red color). These electrodes were prepared and subjected to the same conditions of the SHT (450 C) and tested at the same conditions of the current densities (100, 2000, and 3000 mA g ⁻¹). The electrode of NSi/PAA-CMC (blue color) was prepared using (60%) of NSi with (40%) of PAA/CMC. The electrode of NSi/g-PAN (green color) was prepared using NSi (60%) with PAN (40%).....	69
Figure 5.14 (a) HAADF-STEM image of Si electrode surface after 650 cycles with its corresponding EELS mapping of (C, Si, N, and O), and (b) a schematic showing the structure change of Si particles before and after cycling.....	71
Figure 6.1 A schematic illustration of the design procedure of the NSi@N-CNT/g-PAN composite.....	78
Figure 6.2 (a) TEM image of few Si particles shows the average diameter of about 50 to 70 nm, (b) HRTEM	

image of the crystalline Si particle shows the oxide layer (b) XPS of Si 2p of pure Si shows the SiO _x peak.....	79
Figure 6.3 (a) SEM image of long N-CNTs, (b) TEM image of N-CNTs, (c) HR-SEM image of NSi@N-CNT shows Si particles connected to the N-CNTs, (d) TEM image of NSi@N-CNT shows the Si particles connected to the N-CNTs (e) HR-SEM image shows g-PAN covered the NSi@N-CNT network, and (f) TEM image of NSi@N-CNT/g-PAN nanocomposite shows the g-PAN covered the NSi@N-CNT.....	81
Figure 6.4 (a) TEM image of N-CNT with its corresponding EDX elemental mapping for (C, O, N and overlap elements).....	82
Figure 6.5 (a) HR-SEM image of NSi@N-CNT/g-PAN electrode with its corresponding EDS mapping of Si, N, C, and O.....	82
Figure 6.6 Digital photos of the NSi@N-CNT/g-PAN electrode before and after bending showing keep adhered with no detachments.....	82
Figure 6.7 XRD patterns of g-PAN, N-CNT, NSi@N-CNT, and NSi@N-CNT/g-PAN nanocomposite....	84
Figure 6.8 Raman spectrum of pure Si, N-CNT, NSi@N-CNT, g-PAN, and NSi@N-CNT/g-PAN nanocomposite.....	85
Figure 6.9 (a) Raman spectra of D and G bands of N-CNT, g-PAN, NSi@N-CNT and NSi@N-CNT/g-PAN with their relative shifts and (b) Raman spectra Si peak of NSi@N-CNT and NSi@N-CNT/g-PAN composites shows the shift of Si peak.....	85
Figure 6.10 XPS spectrum of the PAN, N-CNT, N-CNT/g-PAN, NSi@N-CNT/PAN, and NSi@N-CNT/g-PAN nanocomposite.....	88
Figure 6.11 (a) The high-resolution XPS of N 1s of CNT, N-CNT, N-CNT/g-PAN, and NSi@N-CNT/g-PAN nanocomposite, (b) cyclization reaction of PAN, (c) XPS of C 1s of NSi@N-CNT/g-PAN nanocomposite, and (d) XPS spectrum of Si 2p of NSi@N-CNT/g-PAN nanocomposite.....	89
Figure 6.12 (a) Discharge/charge profile of the NSi@N-CNT/g-PAN nanocomposite tested at low current rate of 500 mA g ⁻¹ , (b) Cycling stability and the areal capacity of the NSi@N-CNT/g-PAN composite in (a).....	91
Figure 6.13 Rate capability of NSi@N-CNT and NSi@N-CNT/g-PAN tested at different current rates (100 to 6000 mA g ⁻¹).....	92
Figure 6.14 Long-term cycling stability of NSi@N-CNT, NSi/g-PAN, and NSi@N-CNT/g-PAN composites tested at current rates of 100 and 2000 mA g ⁻¹ for the first ten cycles followed by 3000 mA g ⁻¹ for the subsequent cycles.....	94

Figure 6.15 Cycling performance of our NSi@N-CNT/g-PAN electrode (red color) compared with the electrode of NSi@N-CNT/g-PAN electrode without SHT.....	94
Figure 6.16 Voltage profile and corresponding the cycling stability of N-CNT/g-PAN electrodes (a-b) cycled at low current rate of 100 mA g ⁻¹ for 400 cycles, and (c-d) cycled at high current density of 3000 mA g ⁻¹ for long cycling of 1000 cycles.....	96
Figure 6.17 Cycling voltammetry curves of a coin-type half-cell: (a) for the NSi@N-CNT/g-PAN electrode, and (b) for the NSi@N-CNT electrode.....	97
Figure 6.18 Electrochemical impedance of the NSi@N-CNT, NSi/g-PAN, NSi/PVDF/Super P, and NSi@N-CNT/g-PAN electrodes after 10 cycles.....	99
Figure 6.19 TEM images of the NSi@N-CNT/g-PAN nanocomposite before cycling, after 50 cycles, and after more than 1100 cycles.....	100
Figure S4.1 Optical images of the Si electrode before and after SHT.....	117
Figure S4.2 (a) SEM image shows the SiNPs with PVP are embedded in the matrix of PVP polymer and self-assemble in a leaf morphology, (b) SEM image of the Si electrode treated at 450 oC shows the carbon layer shielding the SiNPs and formting breathable shell and their distribution around the SiNPs, and (c) SEM image of Si electrode treated at 750 oC shows the distribution the carbon layers around the SiNPs.....	117
Figure S4.3 HAADF-STEM across Si particles of the untreated electrode and its associated EDS elemental line scan across the particles as marked line, (a) treated at 450 C, (b) treated at 750 C.....	118
Figure S4.4 Rate capability behavior of Si/PAN electrode without PVP treated at 750 C.....	118
Figure S4.5 Cycling behavior of Si/PVP electrode without PAN treated at 750 C.....	119
Figure S4.6 Cycling behavior of Si/PVP/PAN electrode without SHT.....	119
Figure S5.1 SEM images of the Si electrode: (a) SiNPs coated by PAA/CMC copolymer after freeze drying, (b) SiNPs coated by the PAA/CMC/PAN before SHT, and (c, d) SiNPs after SHT wrapped by nanosheets of graphenized PAN (g-PAN).....	120
Figure S5.2 (a) Low magnification TEM images of the NSi/PAA-CMC/g-PAN electrode treated at 450 °C showing a few Si particles well-wrapped by graphenized nanosheets and (b) digital image of the Si electrode after SHT. Even the electrode wound by lab tweezer, there is no any physical cracks are observed.....	121
Figure S5.3 (a) HAADF-STEM image of another electrode of NSi/PAA-CMC/g-PAN after SHT with its corresponding EELS mapping for (Si, C, O, N and overlap elements) for the image (a).....	121
Figure S5.4 Thermogravimetric analysis curves (TGA) analysis for pure PAN, pure CMC, and pure PAA in nitrogen atmosphere with a ramp rate of 10 °C min ⁻¹	122
Figure S6.1 XPS spectrum of CNT materials.....	123

Figure S6.2 DSC analysis for pure PAN in nitrogen shows a sharp peak at ~ 300 °C, which corresponding to the cyclization reaction of the nitrile group (C≡N) in PAN structure.....	124
Figure S6.3 Thermogravimetric analysis (TGA) curves of pure PAN, N-CNT, and NSi@N-CNT/g-PAN in nitrogen atmosphere with a ramp rate of 10 °C min ⁻¹	124
Figure S6.4 High-resolution XPS spectra of N 1s in pure PAN showing the nitrile groups (C≡N) in PAN structure.....	124
Figure S6.5 Long cycling performance of our NSi@N-CNT/g-PAN electrode compared with N-CNT/g-PAN cycled at the same current rates of at 100, 2000 mA g ⁻¹ then continued at 3000 mA g ⁻¹	125

List of Tables

Table (2.1) List of various solvents generally utilized within the electrolyte of Li-ion batteries and their physical properties.....	20
Table (6.1) Elemental compositions of N-CNT/g-PAN composite from XPS analysis.....	88

List of Abbreviations

Ar	Argon
CMC	Sodium carboxymethylcellulose
CNT	Carbon nanotube
CV	Cyclic voltammetry
DDI	Distilled de-ionized
DMC	Dimethyl carbonate
DMF	Dimethylformamide
DSC	Differential scanning calorimetry
EC	Ethylene carbonate
EELS	Electron energy loss spectroscopy
EIS	Electrochemical impedance spectroscopy
FHT	Flash heat treatment
FTIR	Fourier-transform infrared
g-PAN	Graphenized polyacrylonitrile
GO	Graphene oxide
HRTEM	High-resolution transmission electron microscope
Li	Lithium
LIBs	Lithium-ion batteries
LiCoO ₂	Lithium cobalt oxide
LiFePO ₄	Lithium iron phosphate
LiMn ₂ O ₄	Lithium manganese oxide
LiPF ₆	Lithium hexafluorophosphate
N	Nitrogen
N-CNT	Nitrogen-doped carbon nanotube
NG	Nitrogen-doped graphene
NMP	N-methylpyrrolidinone
PAN	Polyacrylonitrile
PAA	Polyacrylic acid
PVDF	Polyvinylidene fluoride
PVP	Polyvinylpyrrolidone
SAED	Selected area electron diffraction

SEI	Solid electrolyte interphase
SEM	Scanning electron microscope
SHT	Slow heat treatment
Si	Silicon
SiNP	Silicon nanoparticle
SiMP	Silicon microparticle
SiO ₂	Silicon dioxide
TEM	Transmission electron microscope
TGA	Thermogravimetric analysis
V	Voltage
XRD	X-ray diffraction
XPS	X-ray photoelectron spectroscopy

Chapter 1: Introduction

1.1 Motivation and Challenges

Fossil fuels are currently the world's major energy source for electrical productions and transportation despite the fact this source of energy is non-sustainable and results in significant carbon emissions that cause health problems and climate challenges. Therefore, clean energy research and development is becoming one of the world's prime topics of concern. On the other hand, the worldwide market size of clean energy from wind and solar has increased over the years, leading to an increasingly greater demand for highly energy storage systems. Furthermore, with the rising demand for high performance and economically feasible energy storage systems in applications, considerable efforts have driven the development of the next-generation sustainable energy developments and storage systems. Rechargeable batteries are more efficient, clean, and sustainable energy storage, and they are considered as one of the most promising techniques to solve these issues. Among present battery systems such as nickel metal hydride, nickel-cadmium, and lead acid, lithium ion batteries (LIBs) are the strongest candidates to be used in the near future to store electrical energy from clean sources. This is because of their high volumetric and gravimetric density, high power density, long cycle life, no memory effect, low self-discharge, and good environmental benignity.¹⁻⁸ Moreover, LIBs have demonstrated to be the most efficient energy storage strategy for portable devices like cellular phones, laptops, and digital electronics.⁹⁻
¹² However, due to the insufficient energy density of LIBs, current batteries are not suitable for use in electric vehicles due to their limited mileage per charge compared to vehicles powered by combustion engines. Therefore, great volume of research efforts has been focused on developing

next-generation LIBs possessing high energy and power density. These studies include developing new active materials for both electrodes (anode and cathode), electrolytes, and overall cell design. The active material in the electrodes is considered the most important component when determining the power density, energy density, and the cycle stability of LIBs. Therefore, the major challenge of LIBs is a selection of acceptable anode materials that can supply high capacity and smooth the diffusion of Li ions into the anode along with excellent cycling life and high safety. To increase the capacity on the anode side, silicon-based materials have been investigated owing to their extraordinarily high capacity. Silicon (Si) has been the subject of attention for researchers because it has a higher theoretical specific capacity of around 4200 mAh g⁻¹, more than ten times higher when compared to the widely used graphite anodes (372 mAh g⁻¹). Therefore, Si can be used as an active material to provide improved densities over commercial graphite electrode materials. In addition, Si is naturally abundant, low-cost, non-toxic, and environmentally friendly.¹³⁻¹⁵ However, the practical applications of the Si material suffers from rapid capacity loss upon cycling mainly due to the huge volume change of Si particles during lithium insertion and extraction processes. Upon full lithiation, a Si particle can expand up to 300% of its original volume by forming a Li₂₂Si₅ alloy. This huge volume change usually leads to the pulverization of the Si particle itself due to the stress generated through the lithiation. Moreover, this volume change may also cause the dissociation of the active material from the substrate and deteriorate the electric contact between the active material and the current collector. Additionally, an unstable solid electrolyte interphase (SEI) layer forms on the Si particle surface by the side reaction between the electrolyte and exposed Si surface upon expansion and contraction, which leads to instability in the SEI, short cycle life, and largely irreversible capacities during cycling.¹⁶⁻²⁰ The continuous growth of unstable SEI will prevent the electron conductive diffuses between the active material

and current collector.²¹ Several research efforts have been investigated to overcome these challenges in the last few years. This thesis focuses on developing advanced electrode materials to enhance the energy density of rechargeable LIBs.

1.2 Thesis Objectives and Approaches

To address the loss of electrode integrity of the Si anodes during battery charging and discharging, this thesis research focuses on developing facile and scalable methods to fabricate advanced nanostructured negative electrode to boost the energy density of future energy storage applications of LIBs. Si nanoparticles (SiNPs) greatly improve the capacity of the electrodes in LIBs. However, it has been shown that the nanosized Si still has some issues with cycle stability and reaction kinetics of the electrode. The vital components of the electrodes apart from the active material are the binder and conductive additives. The harmony between the three components determines the electrode capability for performing the reversible lithiation and delithiation for a large number of cycles. The ultimate goal is to generate conductive scaffolds that nest the active Si material and are flexible enough to compensate for the stresses due to the volume changes during the reaction of lithium with Si. Therefore, the approaches proposed in this thesis are designed to focus on the polymeric binder and reinforcement additives while eliminating the addition of conducting material. In brief, we use *in situ* manipulation of polymeric materials to generate a core-shell-cage structure that hosts and protects the SiNPs from pulverization. This process uses inexpensive raw materials with easy synthesis procedures. Following this, we develop a programmed heat treatment that modified and partially carbonized the binder leading to the formation of a conductive skeleton. This will help to host the Si particle while maintaining an elastic structure that is breathable for volume changes within the electrodes and improves the

conductivity of the whole electrode. The following strategies have been investigated to develop and improve the electrode performance:

1) Preparation of blend polymer chemistry for high performance of Si/PVP/g-PAN composite:

We investigated a copolymer blend such as polyvinylpyrrolidone (PVP) and polyacrylonitrile (PAN) polymers, that have rich oxygen and nitrogen atoms in their chains. Since the electrode preparation considers a critical step to achieve the homogenous distribution of the electrode materials, therefore, the mixing techniques and freeze-drying help to generate a core-shell and cage nature of PVP/PAN polymers around the SiNPs. This sequence of application of this polymer mix could promote the formation of an intimate coating of oxygen layer with nitrogen-rich carbon shell over Si nanoparticles through heat treatment. Also, investigate the impact of different temperatures of heat treatment on the synthesis of this blend polymer.

2) Cross-linking and graphenization for high performance of Si/PAA-CMC/g-PAN composite:

The success of the previous project encourages us to use commercially available binders to simplify the fabrication techniques of the Si anode. Therefore, using water-soluble polymers that involve condensation chemistry and their nanoengineering can form the stable electric skeleton which can hosts the Si particle. The example of this is to determine the effect of a cross-linking system of carboxymethyl cellulose (CMC) and polyacrylic acid (PAA) on Si anodes. Apart from the solubility of the PAA and CMC mixture in water, which undergoes a condensation reaction by coupling together upon heating and forming an ester linkage. Also, from the previous work, we found that the modified PAN can form a nitrogen-doped graphene structure after heat treatment, which can be used as a binder and conductive additive to improve the electrical conductivity of the electrode. Therefore, this integrates the cross-linking polymers into the conductive elastic network can stabilize the lithiation of Si and compensate for the volume changes.

3) Based on the previous studies, we found that the nitrogen content delivered from g-PAN within the electrode structure has a critical role in improving the long cycling performance of Si anodes. Therefore, in this study, we will investigate the integration of nitrogen-doped carbon nanotube (N-CNT) materials as a reinforcement additive with graphenized PAN to Si active material. This is because the N-dopant has a higher electronegativity than carbon, which produces permanent dipoles on the graphitic surfaces, greatly improving the surface energy. At the same time, involving the graphenized PAN, which is considered a secondary source of nitrogen at a low cost, could minimize the pulverization of Si particles and improve the electrical conductivity of the electrode due to their conjugated structure.

1.3 Thesis Outlines

This thesis contains seven chapters presented in the following sequences:

Chapter 1 provides a brief introduction, which includes the motivation and challenges followed by the objectives of this thesis. **Chapter 2** provides the necessary background information and a literature review of LIBs with their principles presented and discussed. Also, a brief introduction to various components for LIBs is surveyed in this chapter. Cathodes and anodes materials are reviewed with a focus on Si anodes and related research, then electrolytes and binders for lithium ion batteries are presented. **Chapter 3** provides background information on the physicochemical characterization techniques with a brief operation principle that is involved in this study including transmission electron microscopy, X-ray diffraction, X-ray photoelectron spectroscopy, energy dispersive X-ray spectroscopy, and Raman spectroscopy. Also, this chapter describes the electrode fabrication and assembly of coin-type cells. Details of the electrochemical characterization techniques used in this thesis will also be described. **Chapter 4** describes the development of a

copolymer blend of PVP and PAN as a flexible network for advanced negative electrode through slow heat treatment. This chapter presented the experimental work of Si electrode fabrication and results and discussion followed by a brief summary. **Chapter 5** focuses on designing multi-functional binders of cross-linking with graphenization system through a one-pot thermal treatment. The engineered system possesses enough flexibility and conductivity to be coupled with Si material. This architecture provides high capacity with excellent cycling battery performance. **Chapter 6** highlights the development of a scalable approach that depends on the binding of the surface of Si particles to nitrogen-doped carbon nanotubes followed by wrapping them with nitrogen-doped graphene sheets delivered by graphenized polyacrylonitrile. This structure with a high content of nitrogen led to improved material property that can provide long cycling with high capacity at a high current rate. **Chapter 7** concludes all the works presented in this thesis along with recommendations for future research directions to advance the development of Si anode towards practical applications on a large scale.

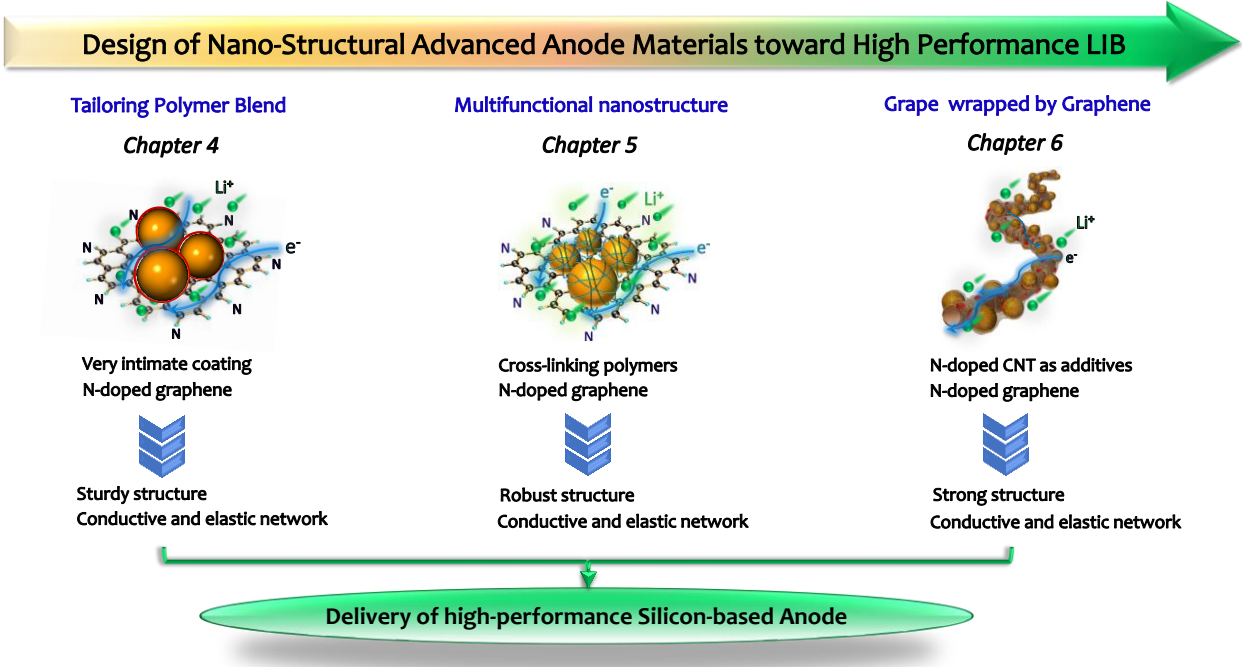


Figure (1.1) Schematic illustration of the research topics through thesis workflow.

Chapter 2: Background and Literature Review

2.1 Battery Technology

Battery, invented by Alessandro Volta in 1800,²² is an electrochemical device that converts the chemical energy into electrical energy and is often used to store energy. The battery is a device consisting of two electrochemically active couples, a negative electrode, and a positive electrode. The electrodes are separated by an electrolyte which is either a liquid or a gel containing dissociated salts, which allows in transferring the ions between the electrodes. Due to differences in the chemical potentials between these electrodes, the electrons are forced to pass through one electrode to the other electrode. There are two types of batteries, primary and secondary batteries. The primary batteries can be used once and discarded because the chemical reactions of these batteries are not reversible. For example, the types of primary batteries are alkaline batteries, zinc-carbon batteries, and lithium metal batteries.²³ The secondary batteries, which are rechargeable batteries that can be charged and discharged for many times. The common secondary batteries include lithium-ion, nickel cadmium (NiCd), nickel metal hydride (Ni-MH), and lead acid systems. Nowadays, rechargeable batteries are considered among the most successful techniques that can provide clean electricity from stored materials through coupled redox reactions. Lithium ion batteries are considered the most promising candidate's energy storage currently available due to their high volumetric and gravimetric energy densities in comparison with other battery chemistries such as nickel metal hydride (Ni-MH) and lead-acid batteries as shown in **Figure (2.1)**. However, reducing the cost and the increasing energy density are two impediments that prevent the widespread application of LIBs for electric vehicles (EVs) and renewable energy storage.

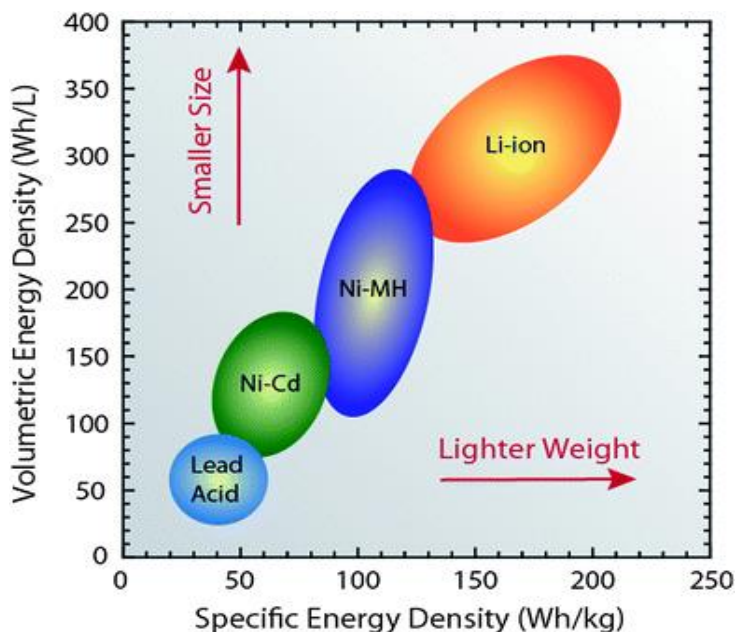
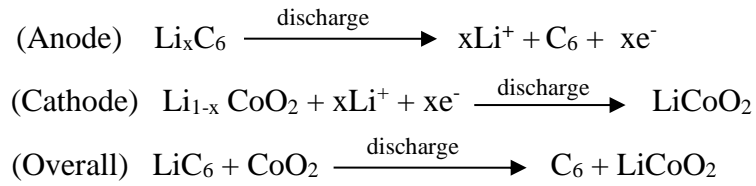


Figure (2.1) Diagram comparing the volumetric and gravimetric energy densities of several common energy storage technologies.²⁴

2.2 Lithium-ion Batteries

Lithium-ion batteries currently are becoming a more common part in consumer electronic devices due to their high energy density and high charge and discharge rate capabilities. The main principle of LIBs is the insertion and extraction of lithium ions to and from the two electrodes. Lithium (Li), which has the highest electropositive potential of 3.04 V versus standard hydrogen electrode (SHE) when alloyed or compounded with other elements can form large open-circuit voltages such as ~ 3.7 V of commercial LIBs. In addition, Li is considered the lightest metal in the world (atomic mass of Li is 6.94, and its density is 0.53 g cm⁻³) and it has a 3860 mAh g⁻¹ of specific capacity for a charge in comparison with only 260 mAh g⁻¹ for lead (Pb).^{25, 26} These characteristics encourage the implementation of Li as a base material in energy storage as it can simplify the design of batteries with exceptionally high energy densities.

Generally, the traditional LIBs contain three functional components which are an electrolyte, a graphite-based material as an anode (negative electrode), and lithiated transition metal oxide (Li source) as a cathode (positive electrode). Copper foils and aluminum foils are used as both substrates and current collectors for anodes and cathodes, respectively, which are usually separated by a polymer membrane. The membrane works as a barrier to prevent the physical contact between the negative and positive electrodes.²⁷ The liquid electrolyte used in LIBs is usually a Li-ion enriched solution composed of a Li salt such as lithium hexafluorophosphate (LiPF_6) dissolved in a mixture of organic solvents e.g. ethylene carbonate (EC), and dimethyl carbonate (DMC). The electrolyte plays a significant role as a medium for transporting the Li-ions between the anode and cathode during the battery operation. The general material used as a positive electrode (cathode) is one of these materials: a layered oxide such as LiCoO_2 , LiFePO_4 , and LiMn_2O_4 , which are formed by the insertion of Li ions between the slabs of the host materials. Graphite is the most common material used as an anode material in commercialized LIBs. During the discharging process, an oxidation reaction takes place at the negative electrode. The Li ions are deintercalated and transferred from the anode through the porous separator in the electrolyte, which has a high chemical potential to be re-intercalated into the cathode, which has a low chemical potential. Meanwhile, the electrons transfer through the external circuit from the anode to the cathode. Therefore, the differences in chemical energy is released as electricity. In the charging process, which is a reverse process, the current passes from an external electrical power source in the reverse direction to the battery. This current causes the Li ions to migrate from the cathode to the anode. Cathode reaction, anode reaction, and overall reaction for a LiCoO_2 /graphite-based LIBs are as follows:



Even though LIBs are currently the most developed energy storage technology for a multitude of electronic applications, researchers are still faced with many critical challenges to apply LIBs to electric vehicles. This greater challenge is low energy density. The urgent demand for high energy density and high-power density of LIBs is growing, especially for electric vehicles to carry sufficient energy comparable to current combustion engine-based vehicles. All LIBs currently still use a graphite material as an anode, which has a limited capacity of 372 mAh g⁻¹. Therefore, to improve the energy density of LIBs would require searching for new anode materials that have a higher capacity than graphite. In addition, anode materials with higher charge capacity can increase the energy and power densities of LIBs, thereby making them smaller in size and lower in cost. Moreover, the difference between the anode and the cathode materials in terms of the voltage and the capacity is that the anode materials have lower potential whereas the cathode materials have higher potential. This difference between two electrodes in a cell constitutes the cell voltage. Therefore, the LIBs system has high cell voltage, which can reach up to 4.5 V. This voltage is the highest among all types of batteries, which is a great advantage for LIBs.

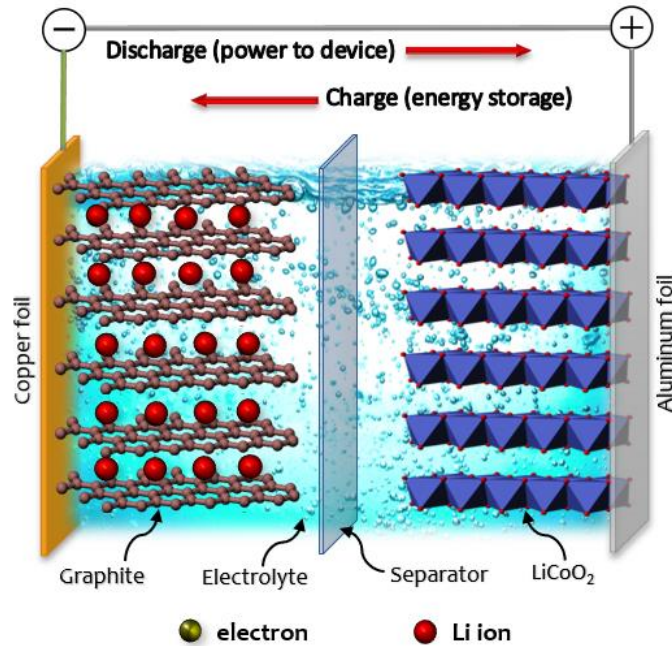


Figure (2.2) Schematic illustrations of the main components and operation principles of a conventional LIB.

2.3 Cathode Materials

Cathode materials have been playing important roles in the development of LIBs as mentioned in the introduction. To be used in LIBs, cathode materials should have a significantly higher potential than the anode materials. In addition, to be an ideal candidate, cathode materials should have electronic conductivity, simple Li diffusion, and structural stability. Researchers have studied intensively several transition metal compounds such as Mn, Fe, Co, and Ni. These transition metal oxides are common cathode materials along with the inclusion of chalcogens group elements, especially oxygen, give more structural stability than halogens. These transition metal oxides can be classified based on their structure to layered, spinel, and olivine structures.

2.3.1 Layered Structure

The general formula of the layered structure is LiMO_2 (where M is Co, Ni, etc). Lithium cobalt oxide materials (LiCoO_2) are used as the common layered structure cathode materials in commercialized LIBs by Sony since 1991.²⁵ The LiCoO_2 atoms are arranged in cubic close packing, in which Li and cobalt ions occupy octahedral sites in alternating layers (**Figure 2.3**). LiCoO_2 has a theoretical capacity of 272 mAh g^{-1} . However, the effective capacity is only 145 mAh g^{-1} . This difference stems from the fact that the crystalline structure of LiCoO_2 collapses upon the complete Li extraction. However, there are several concerns of the LiCoO_2 structure such as toxicity and the high price of cobalt on the other metal oxides as well as the safety hazard, especially when the battery is overheated.

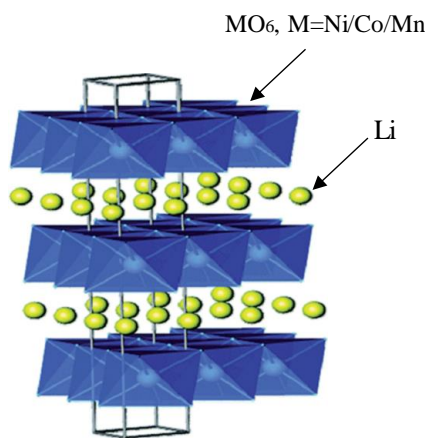


Figure (2.3) Schematic illustration of the layered structure of LiMO_2 , e.g. LiCoO_2 .²⁸

2.3.2 Spinel Structure

The common spinel cathode material is lithium manganese oxide (LiMn_2O_4) as shown in **Figure (2.4)**. In LiMn_2O_4 , the oxygen atoms have a cubic close packing structure, in which lithium and manganese atoms are distributed to the available tetrahedral and octahedral sites, respectively.

The theoretical capacity of LiMn_2O_4 is 148 mAh g^{-1} . In this case, the practical capacity is limited to around 120 mAh g^{-1} which is about 10% less than that of LiCoO_2 . In addition, upon prolonged cycling at 4.0 V attributed to the dissolution of manganese ions and strain generation on the crystal which forms a capacity fading problem. To improve the cycle stability, doping of other transition metals such as Ni, Fe, Ti, Cu, Zn were studied.^{29, 30}

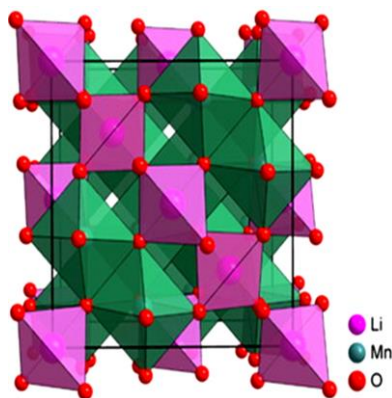


Figure (2.4) Schematic illustrations of the spinel structure of LiMn_2O_4 .^{31, 32}

2.3.3 Olivine Structure

The most common cathode material possessing the olivine structure is lithium iron phosphate (LiFePO_4) as shown in **Figure (2.5)**.³³ In LiFePO_4 crystal, Li and Fe ions are surrounded by six oxide ions in an octahedral structure whereas the phosphate group (PO_4) has a tetrahedral structure. This structure of LiFePO_4 has a capacity of 170 mAh g^{-1} , which is higher than LiCoO_2 . In addition to its capacity, LiFePO_4 is low-cost, non-toxic, possesses excellent cycle stability, and environmentally friendly, which makes it a promising cathode material. However, the strong bonding of oxygen to Fe and P leads to a low electrical conductivity and ion diffusivity at room temperature. The carbon coating and reducing the particle size are used to improve the performance of the olivine structure as cathode materials.^{34, 35}

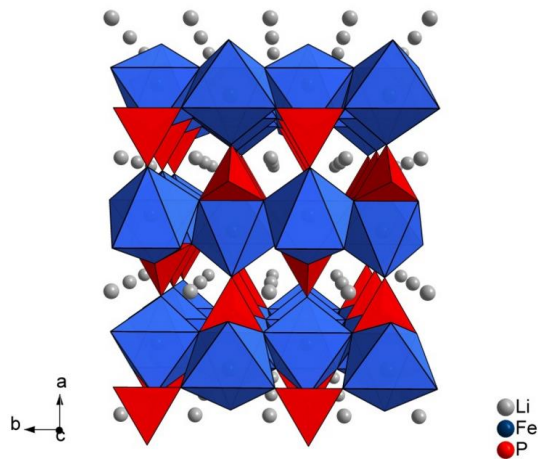


Figure (2.5) Schematic illustrations of the olivine structure of LiFePO_4 .³³

2.4 Anode Materials

2.4.1 Lithium Anode

The anode is considered one of the major components of a Li-ion battery. Early, lithium metal was used as an anode material for the rechargeable batteries, especially during the 1970s and 1980s due to its high theoretical capacity (3860 mAh g^{-1}) and low density.³⁶ However, due to its safety issues, there are some challenges that made the lithium metal not successful as an anode for the commercial application of LIBs. First, lithium forms dendrites on the surface of the lithium electrode during charging and discharging processes, which causes an internal short circuit of the battery. Second, changing the volume of the lithium anode during the plating/stripping process. Third, the continuous growth of unstable solid electrolyte interface (SEI) on the surface of the lithium metal electrode.^{26, 37} Therefore, intensive researches have been focused to find alternative anode materials for LIBs.

2.4.2 Graphite Anode

Nowadays, graphite has been commonly utilized as anode material for commercial LIBs. Graphite is a carbonaceous structure composed of several layers of graphene (**Figure 2.6**). Also, graphite has many advantages that explain its domination in the market of LIBs anodes. First, graphite is abundant in nature and cheap to obtain. Second, graphite shows capability in storing lithium by forming LiC_6 upon full lithium intercalation. Third, graphite anodes can form a stable SEI, which will help graphite anodes maintain good stability over extended cycling. In addition, the low working potential (0-0.3V vs. Li/Li^+) of graphite can help contribute to the overall high energy density of LIBs. However, the theoretical capacity of graphite is only 372 mAh g^{-1} , which cannot meet the increasing demand for the requirements of future advanced electric vehicles which require batteries with much higher energy density. Therefore, intensive efforts have been devoted to find a new anode material with a higher specific capacity and can appropriate satisfy all the requirements.

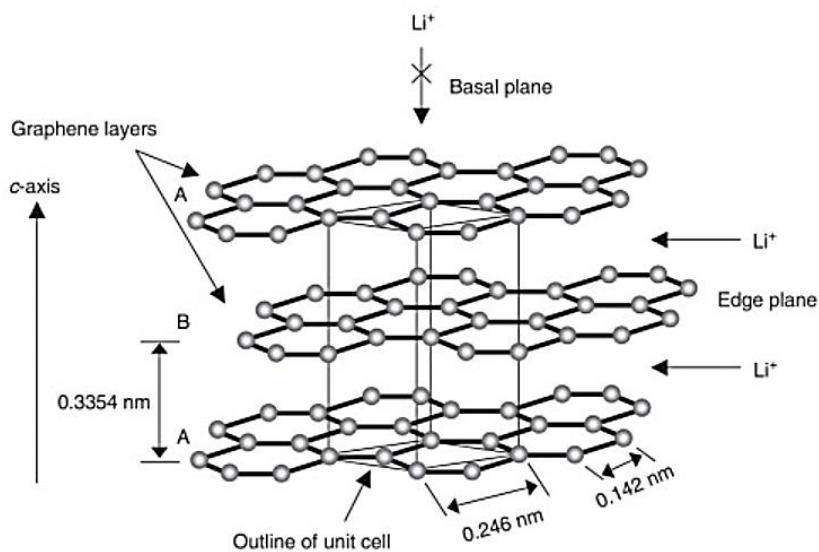


Figure (2.6) A schematic illustration of the graphite crystal structure with the stacking of graphene sheets and the unit cell.³⁸

2.4.3 Silicon Anode

Different anode materials such as pure Tin (Sn), silicon (Si), antimony (Sb), magnesium (Mg), aluminum (Al) and their alloys have been extensively investigated as candidates for the next generation of LIBs due to their higher capacity compared to graphite (**Figure 2.7**).^{7, 39} Among these materials, Si has attracted tremendous attention from the battery community as an excellent material for the negative electrode in the next generation of LIBs. This advantage is due to its high theoretical capacities of up to 4200 mAh g⁻¹ by forming the Li₂₂Si₅ phase, 4008 mAh g⁻¹ for Li₂₁Si₅ phase, and 3579 mAh g⁻¹ for Li₁₃Si₄ phase, which is more than ten times that of the current widely used commercial graphite anodes (372 mAh g⁻¹).^{40, 41} In addition, in the charge state, one silicon atom can coordinate with 4.4 lithium ions by alloying mechanism, which provides a high capacity of Si up to 4200 mAh g⁻¹, while the graphite anode with its structure that every six carbon atoms can accommodate only one lithium ion by intercalation mechanism. Moreover, Si is the second most abundant element in the Earth's crust. Furthermore, Si has low discharge potential (~ 0.5 V vs. Li/Li⁺), good environmental compatibility, low toxicity, and high safety.^{7, 13-15} One of the most important parameters of Si is the small size of its particles which is imperative to reduce stress particle cracking during the lithiation and delithiation processes which will enhance the electrochemical performance of the Si electrodes.^{42, 43} Huang et al. reported that a critical particle diameter of Si is about 150 nm. They found that when the diameter of Si particles is below 150 nm, the Si particles will neither fracture nor crack at the first lithiation.⁴⁴

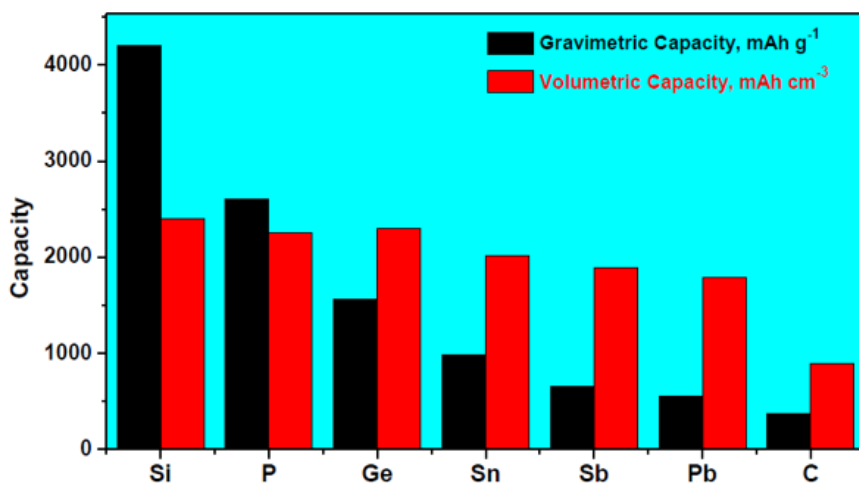


Figure (2.7) Comparing the volumetric and gravimetric capacities of different anode materials.⁴⁵

However, several drawbacks of Si anodes are hindering the material from wide employment in commercial LIBs. As shown in **Figure (2.8)**, the major challenge is that the volume of the Si particle expands by more than $\sim 300\%$ during the lithiation and delithiation processes. Meanwhile, the huge volume change tends to crack and pulverize the particle which leads to loss of the electric contact points between Si particles and the current collector or the conductive network in the electrode, leading to mechanical degradation of the battery. Moreover, the pulverization of Si particle forms fresh surfaces that are exposed to the electrolyte, and reformation of the solid electrolyte interface (SEI) layer continues to form on the fresh surfaces of the Si particles, which results in the consumption of the electrolyte and capacity fading as well as limited cycle life.¹³ In addition, the low ionic and electrical conductivity of Si may hinder the Si rate performance.⁴⁶ Meanwhile, Si particles that are small enough to be able to accommodate the volume change still suffer from continuous SEI growth on the surface due to the volume expansion of Si particles, resulting in the breaking of the SEI that formed. Also, as Si is a semiconductor, it is a challenge

for electrons to transfer quickly from the core of large Si particles to the current collector. Additionally, the complicated synthesis procedures and expensive raw materials prevent practical applications of Si anodes. Several intensive efforts have been devoted to solving these problems. Since the first introduction of Si as an anode material by Boukamp et al. in 1981,⁴⁷ Si has received considerable research attention, especially after the commercialization and broad use of LIBs in the 1990s. These efforts investigated using different materials and different designs of Si electrode nanostructures. To achieve a long cycling stability and excellent electrical conductivity of Si anodes, use of conductive binders and conductive additives is important.

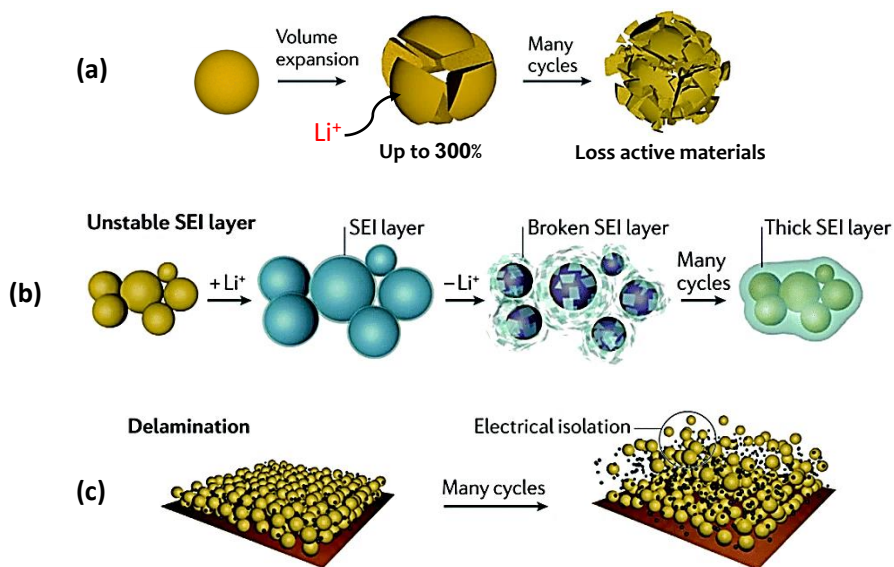
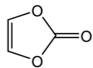
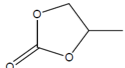
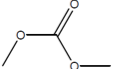
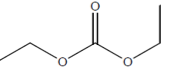
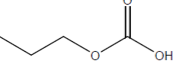


Figure (2.8) A schematic depicting (a) the volume change and the failure mechanism of Si nanoparticles during cycling, (b) unstable SEI layer formation during repeating cycling, and (c) electrical isolation of Si particles during cycling.⁴⁸

2.5 Electrolytes for Li-ion Batteries

In Li-ion batteries, the electrolyte plays an important role as a medium for transporting the lithium ions between the two electrodes during battery operation. Therefore, the electrolyte must be an excellent ionic conductor and stable at high voltages (up to 4.5 V). The electrolyte is typically prepared by dissolving a lithium salt in an organic solvent. The most common salts used in LIBs are lithium hexafluorophosphate (LiPF_6), lithium tetrafluoroborate (LiBF_4), and lithium perchlorate (LiClO_4).⁴⁹ Currently, there are a number of carbonate solvents in use: ethylene carbonate (EC), ethyl methyl carbonate (EMC), dimethyl carbonate (DMC), and diethyl carbonate (DEC).^{49, 50} The solvents that are usually used for LIBs with their properties are shown in **Table (2.1)**. In the proposed research, fluoroethylene carbonate (FEC) is added to commercial electrolytes with 1M LiPF_6 in EC/DMC or EC/DEC which is the most commonly used in today for Si electrodes.⁴⁹

Table (2.1) List of various solvents generally utilized within the electrolyte of Li-ion batteries and their physical properties.⁵⁰

Structure	Melting Point (°C)	Boiling Point (°C)	Viscosity (cP at 25 °C)	Dielectric Constant (at 25 °C)
 ethylene carbonate	36.4	248	1.9 (40 °C)	89.78
 propylene carbonate	- 48.8	242	2.53	64.92
 dimethyl carbonate	4.6	91	0.59 (20 °C)	3.11
 diethyl carbonate	- 74.3	126	0.75	2.81
 ethylmethyl carbonate	- 53	110	0.65	2.96

2.6 Polymeric Binders for Li-ion Batteries

In Li-ion batteries, binders are composed of polymer materials that bind the active materials together and with the current collectors to allow the electrons to transfer in the electrodes. In addition, adding these materials could help to improve the adhesion and mechanical strength of the electrode materials.^{51, 52} The polymer binders are components that are used in the electrode preparation to keep the integrity of the electrodes in LIBs. The distribution of the binder material with the active material may play an important role which affects the electrode morphology. As mentioned above, Si nanoparticles expand during the charge and discharge processes in LIBs. In recent years, adding binder components to the Si material to form a composite has been the most successful strategy to improve the cycling performance of Si-based anodes. Therefore, the binder materials used for the Si anode play a critical role to minimize the side reactions with the electrolyte and to form a stable SEI that extends the cycle life of the Si anode.^{53, 54} In addition, the ratio of the active material to the binder is a significant factor that can determine the performance of the electrode. Moreover, although the mass ratio of binder materials in the electrode is lower than that of the active material, they play a crucial role in controlling the structural integrity of the electrode.⁵⁵⁻⁵⁷ To improve the cycling performance of Si anodes, a chemical reaction must occur between the binder and the Si surface to form a covalent bond between the binder and the Si materials.⁵⁸ In addition, various conductive binders can improve the performance of the Si anode with limited additional conductive additive.⁵⁹ Therefore, conductive binders work to minimize the need for conductive additives with the electrode materials which would increase the gravimetric capacity and energy density as well as reduce the weight of the battery. As a result, different polymers have been investigated as possible binder candidates for the Si-based anode materials of LIBs.⁶⁰⁻⁶⁶ Polyvinylidene fluoride (PVDF) is one of the conventional binders, which has been

commonly used as a binder for graphite electrode in LIBs for the previous three decades. However, PVDF is not a suitable binder for Si anode because it cannot accommodate the silicon's volume extension during cycling. Several experiments have reported that PVDF binder can barely provide capacities around 1000 mAh g^{-1} only for a few cycles.^{64, 67, 68} For instance, Liu et al. (2005) showed that using PVDF binder with Si anodes leads to rapid capacity fading.⁶⁹ Compared with the PVDF, several studies have recently shown that a carboxymethyl cellulose (CMC) binder has a better rate capability, cycling stability, and forms a more stable SEI than PVDF.⁷⁰⁻⁷² Hochgatterer et al. (2007) showed that using CMC as a binder can enhance the chemical bonding between the binder and Si-OH groups on the surface of Si particles, which improve the cycling performance of Si-based anodes compared with PVDF.⁷³ Magasinski et al. (2010) demonstrated that using poly(acrylic acid) (PAA) as a binder could improve the rate performance of the Si anodes more than other binders such as CMC and PVDF due to its large amount of carboxylic groups.⁶⁴ Another work by Birdel et al. (2011) showed a positive impact of the hydrogen interaction between the carboxyl functional group of CMC and the Si-OH groups on the surface of Si particles.⁷⁴ Kovalenko et al. (2011) reported that using sodium-alginate polymer as a binder with Si anodes showed significant improvements over the NaCMC binder.⁷⁵ Ling et al. (2014) used gum arabic (GA) as a binder which leads to stable cycling for Si-based anodes in LIBs.⁷⁶ Hassan et al. (2015) discovered a robust electrode using cyclized polyacrylonitrile (PAN) as a binder with sulfur-doped graphene. The prepared Si electrode showed superior capacity of more 1000 mAh g^{-1} for 2275 cycles of Si-based anodes.⁷⁷ Recent researches have investigated that polymeric binders with high electric conductivity can provide high areal capacity for the Si-based anode.⁷⁸⁻⁸¹ Therefore, the effect of binders on the cycling performance of Si-based anodes reveals that a strong connection exists between the binder matrix and Si particle's surface can limit electrode fragmentation.

In summary, all reported results from the literature showed that although there is a small amount of polymeric binders in the electrode, they play a significant role in solving the problematic application of the Si anodes and improving the total performance of the battery. Rate properties and cycle stability of Si-based anodes can be improved by using various polymeric binders and making modifications of Si particles.⁵⁹ Therefore, designing polymeric binders that have carboxylic functional groups can improve the cycling performance of the Si anodes by having a strong interaction between the binder functional groups and the Si surface. As a result, this thesis will focus on exploring novel binder materials to improve the electrochemical performance of Si-based anodes in LIBs.

Chapter 3: Characterization Techniques

This chapter discusses measurements for both physicochemical and electrochemical characterization techniques that are utilized for this thesis. Physicochemical characterizations are mainly utilized to investigate the morphology and crystal structures of the nanomaterials that developed in this thesis, while electrochemical characterizations are utilized to reveal the electrochemical performance of Si electrodes.

3.1 Morphological and Compositional Analyses

3.1.1 Scanning Electron Microscopy

Scanning electron microscopy (SEM) is a powerful magnification technique used to investigate the topography and morphology features of micro and nanoscales. SEM uses an electron beam to take images on the sample surface to obtain information. The electron beam travels through an electromagnetic field followed by a set of lenses to hit on the sample to produce secondary electrons and backscattered electrons. The backscattered electrons are most useful in illustrating the composition contrasts in multiphase samples, and the secondary electrons are helpful in showing the morphology and topography of the samples. The detector then converts the interacted electrons into a signal, which produces the final image. The sample preparation for SEM imaging includes spreading a tiny amount of solid conductive material powder onto a conductive carbon tape on the specimen holder. For the purpose of this work, SEM was used to investigate the surface morphology of the electrode materials before and after annealing.

3.1.2 Transmission Electron Microscopy

Transmission electron microscopy (TEM) is another imaging technique using the electron beam to provide high-resolution images for nanostructured samples on the nanometer scale that can approach atomic scale. While SEM uses electron signals that reflect back to the direction opposite of the incident beam, TEM uses signals, which are transmitted through the specimen then converted to an electric signal to obtain the final image with a very small site of interest. A major advantage of TEM is the capabilities to observe physical details below the atomic level since the size of electrons are smaller than that of atoms. In this thesis, TEM technique was used to investigate the morphology of the Si nanoparticles with the surrounding coating layers in the electrodes. Samples are prepared by gently scratching a small amount of materials from the surface electrode coating then dispersing the material in pure methanol and drop-casting it onto the TEM grid.

3.1.3 Energy Dispersive X-ray Spectroscopy

Energy dispersive X-ray spectroscopy (EDS or EDX) is a common analysis technique that allows identifying the elemental composition of individual points of a sample. This technique is commonly incorporated into SEM and TEM devices to be conducted simultaneously with microscopic analysis. The EDS signal is achieved by detecting X-rays emitted from a sample during the interaction with the electron beam. The binding energy of the emitted x-ray is unique to each element, which provides a blue print for elemental identification and quantification in a sample. Furthermore, the elemental mapping can be used by analyzing the X-rays emitted from localized areas on a specimen surface. EDS can be applied to provide an elemental map, which displays the distribution of localized elements over a selected area of a sample. In this work, EDS

is applied to map the elements and their distribution in the electrode such as carbon, nitrogen, oxygen and silicon.

3.1.4 X-ray Diffraction

X-ray diffraction (XRD) is a common characterization tool used to determine the composition of a crystal structure of materials. To identify the material by XRD, the diffraction pattern of a specific crystal structure of a material can be achieved depending on the X-ray wavelength, which is linked to the distance between atoms in the crystalline material. The X-rays interact with the material to provide diffraction patterns at range of angles, and diffracted X-rays at specific angles are collected and counted by the detector. The diffraction angle is related to the specific crystal orientation of a sample by Bragg's law as shown by Equation (3.1) below,

$$n \lambda = 2d \sin \theta \quad \dots\dots\dots (3.1)$$

Where d , θ , n , and λ represent the spacing between diffracting planes, the incident angle, the order of the spectrum (any integer), and the wavelength of the X-rays, respectively. To identify the material structure, the diffraction pattern at specific angles which are achieved by the XRD can be compared to the theoretical diffraction pattern that is determined by crystal planes.

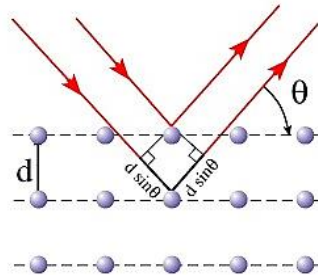


Figure (3.1) Illustration of the Bragg's law.

3.1.5 X-ray Photoelectron Spectroscopy

X-ray photoelectron spectroscopy (XPS) is a tool used to analyze and understand the chemical composition of the electrode materials, electronic states, and to certify the chemical bonding environments of the elements. In this technique, X-rays with known energy irradiate on the sample, causing emission of electrons by a photoelectric effect. The detected kinetic energy and number of electrons that escape from the surface of the sample (top 1 to 10 nm) are analyzed based on the electron binding energy. The binding energy spectrum versus the number of electrons can determine the elements on the surface of the sample and supply the related amounts of each element. In this work, XPS is mainly used to identify the elements in the electrode materials before and after heat treatment.

3.1.6 Raman Spectroscopy

Raman spectroscopy is a practical technique which is used to obtain information about rotational and vibrational modes of a molecule. This technique can be used for both quantitative and qualitative purposes.^{82, 83} When a specimen is radiated by a monochromatic laser beam, both inelastic scattering (Stokes and Anti-stokes) and elastic scattering (Rayleigh scattering) are generated. Meanwhile, the inelastic scattering is used in Raman spectroscopy to obtain the Raman signals as shown in **Figure 3.2**. When the molecule relaxes, a photon is emitted, and the molecule returns to a different vibrational state. The energy difference between the ground state and this final vibrational state causes a shift in the emitted photon's frequency from the excitation wavelength. A stoke shift happens if the final vibrational state is more vibrant than the ground state. Thus, the shift in energy supply information about vibrational modes in the sample. In this

study, Raman spectroscopy is used as principle characterization tool to determine the changes in chemical structure of the electrode materials before and after heat treatment.

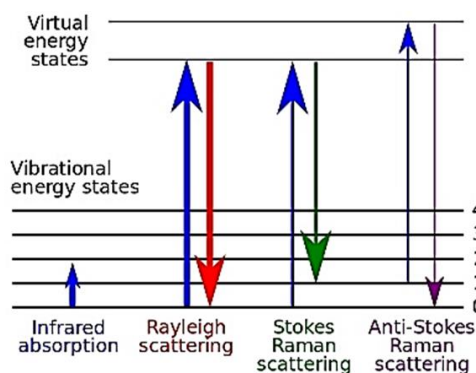


Figure (3.2) Diagram of energy level showing the states involved in Raman signal.

3.1.7 Differential Scanning Calorimetry

Differential scanning calorimetry (DSC) is an useful thermal analysis technique that is used to investigate the phase transformations of materials with heating. DSC can be used to determine the melting point of a crystalline material or glass transition temperatures. The glass transition is a method to determine the property of a material. In addition, the glass transition (T_g) is the temperature at which a polymer material goes from a rigid state to a more flexible state. DSC determines the glass transition as a change in the heat capacity when the polymer matrix goes from the glass state to the rubber state. In DSC, the sample is heated and the amount of heat that is required to raise the temperature is measured and compared to a reference. Endothermic reactions absorb energy and the heat flow decreases. On the other hand, exothermic reactions release heat and the heat flow increases. In this proposal, DSC was used to determine the amount of heat absorbed and released by the electrode materials.

3.2 Electrochemical and Performance Characterization

3.2.1 Fabrication of Coin Cell

To estimate the electrochemical properties of the electrode materials before and after annealing, we fabricated the Li-ion coin cells. **Figure (3.3)** shows the components of the coin-type half-cell. The coin-type half cells (2032 type) with lithium foil (Aldrich, USA) used as a counter electrode were fabricated in an Ar-filled glove box (MBRAUN 10, USA). The electrolyte was composed liquid of lithium hexafluorophosphate (LiPF_6) (1M) in 30wt% ethylene carbonate (EC), 60wt% dimethyl carbonate (DMC), and 10wt% fluorinated ethylene carbonate (FEC). A polypropylene membrane was used as a separator between the negative and positive electrodes. Each coin cell contained $\sim 40\mu\text{l}$ of the electrolyte.

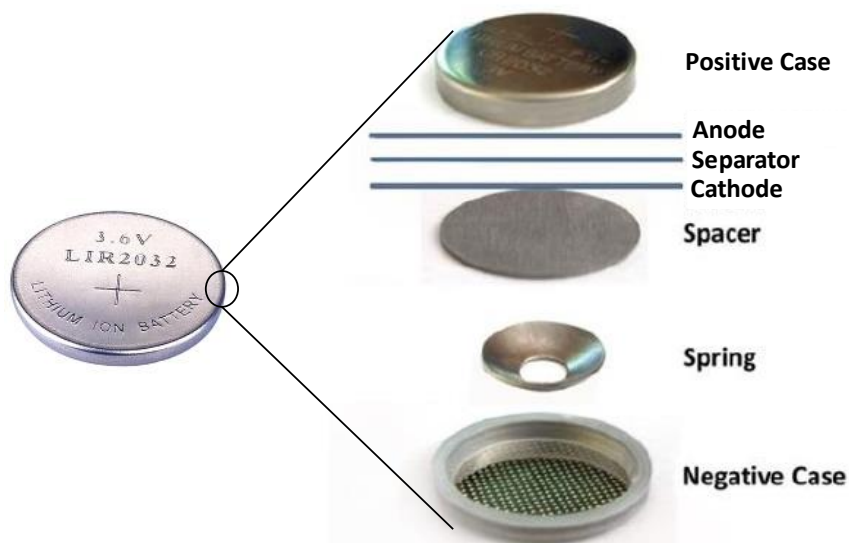


Figure (3.3) Schematic showing the coin cell (type 2032) components.

3.2.2 Charging and Discharging Processes

Electrochemical analyses include the galvanostatic charge and discharge, which can obtain the cycling performance of the batteries. In a single cycle, the battery is charged and discharged using a constant current within a voltage range. Since the time elapsed during the operation is measured by the instrument, it is possible to determine the amount of charge stored and released by the cell at each cycle. The rate capability data of an electrode can be obtained when different currents are applied in the charge and discharge tests. The Coulombic efficiency of an electrode can be monitored for each cycle using this equation:

$$\text{Coulombic Efficiency} = \frac{C_{\text{charge (dilithiation)}}}{C_{\text{discharge (lithiation)}}} \times 100 \dots \dots \dots (3.2)$$

3.2.3 Cyclic Voltammetry

Cyclic voltammetry (CV) is a potentiodynamic electrochemical technique used to investigate the electrochemical properties of the electrodes. CV measurements are done by sweeping the potential of the working electrode linearly at a specific scan rate within a desired potential window (0.01 to 1.50 V). CV curves can expose more information about the electrochemical behavior of the electrodes. The measured current over a potential window is characteristic of the material's redox property (lithium insertion and extraction in this case), which can be compared to the theoretical values. These enable the identification of redox reactions in an electrode and the degree of reversibility. During the first cycles, CV is very important because it shows the differences in patterns after the activation of the material with Li, and in this case, the Si converts from crystalline to amorphous.

Chapter 4. Tailoring the Chemistry of Blend Copolymers Boosting the Electrochemical Performance of Si-based Anodes for Lithium-ion Batteries

This chapter is based on a previously published manuscript by Elhadi N. Attia. et al, *J. Mater. Chem. A*, 2017,5, 24159-24167.

“Tailoring the chemistry of blend copolymers boosting the electrochemical performance of Si-based anodes for lithium-ion batteries”

Reproduced with permission.

4.1 Introduction

In recent years, the intensification of climate change has led to an increasing level of interest for the improvement of green-renewable energy systems to replace the fossil fuels.⁸⁴ Energy storage devices used to buffer the intermittent nature of solar and wind energy has become one of the key limiting factors. Comparing with other energy storage technologies, rechargeable Li-ion batteries are commonly implemented for different applications such as mobile devices, electric vehicles, hybrid electric vehicles, and medical microelectronic devices due to their high specific and volumetric energy densities as well as their lower production costs.^{24, 84, 85} However, current LIBs are reaching their theoretical limits and can no longer be further improved/optimized, prompting researchers to look for next-generation technologies. Fabrication of such a battery technology with the low-cost electrode materials and high-energy density can lead to significant improvements in the performance and lifetimes of products that use LIBs, effectively combating against climate change.^{7, 86, 87}

Among the many candidates for anode materials for high-energy density LIBs, Si has shown great promise as the next generation negative electrodes of LIBs due to its natural abundance, low toxicity, environmentally friendliness, relatively low working potential, and safety. Moreover, compared to the graphite anode materials of commercial LIBs, Si has a high theoretical specific capacity reaching 4200 mAh g⁻¹ when fully lithiated representing a ten-fold increase in potential capacity.^{7, 13-15} For these reasons, many researchers have been intensively studying Si as an anode material in the last few years. However, Si experiences an excessive volume expansion which leads to poor cycling stability, rapid capacity loss and overall degradation of electrochemical performance due to the severe cracks and fast pulverization of the active material.^{13, 15-17, 88-90} Additionally, the continuous volume expansion (lithiation) and contraction (delithiation) results in the detrimental continuous forming of a SEI layer on the Si particle surface by a side reaction between the electrolyte and exposed lithiated Si. This phenomena leads to an unstable SEI, short cycle life, and large irreversible capacities during cycling.¹⁶⁻¹⁹ In addition, Si suffers from low electrical conductivity compared to the graphite, and the diffusion coefficient of Li in Si is low ($\sim 10^{-13}$ cm² /s).⁹¹

To overcome the practical operational problems associated with the Si materials that mentioned above, several strategies have been investigated by researchers. Recent work in the development of a Si anode for LIBs has focused on the incorporation of flexible/breathable conductive support for Si particles of some form with varying degrees of success.⁹² However, the lack of an intimate contact between the conductive support and Si particles limits the potential of such a concept. In addition, complicated synthesis techniques significantly reduce any commercial viability of such concepts. In this chapter, we implement the scalable slow heat treatment (SHT)⁷⁷ on an electrode composed of a rational blend of commercially available polymers:

polyvinylpyrrolidone (PVP) and polyacrylonitrile (PAN) in addition to Si nanoparticles (SiNPs). The interaction between PVP and the hydroxyl groups of Si allows for the extremely intimate contact between the conductive support and SiNPs, as well as the formation of a thin layer of SiO₂ over the surface of SiNPs. In combination with the large PAN derived nitrogen-rich graphene nanosheets, this electrode was able to deliver high capacity with excellent cycle stability and high Coulombic efficiency.

4.2 Experimental Section

Graphene oxide (GO) is one of the electrode materials which was prepared first from graphite powder by the modified Hummer's method.⁹³ In brief, about 2 g of graphite powder was added to 400 mL of a 9:1 volumetric mixture of concentrated H₂SO₄/H₃PO₄. Then, about 18 g of potassium permanganate (KMnO₄) was slowly added to the mixture, and the reaction was heated to 50 °C for about 16 hours. After that, in an ice container, the reaction mixture was cooled down to 10 °C and 400 mL of distilled de-ionized (DDI) water was added in a dropwise method. Finally, to complete the oxidation reaction, about 15 mL of hydrogen peroxide H₂O₂ (30%) was added to the mixture, and then the final mixture was centrifuged to separate out the solids, which were washed exhaustively with water, ethanol, and HCl (30 %); then followed by drying.

Si nanoparticles with an average diameter of 50 to 70 nm were bought from Nanostructured & Amorphous Materials, Inc. (Houston, TX), we fabricated the electrodes for LIBs testing. Typically, about 20% of PVP (M_w = ~ 1300,000, Sigma-Aldrich Co) was used as a binder, which dissolved in DDI mixing for about 20 minutes at room temperature. Then, 80% of SiNPs were added to the PVP solution and mixed by stirring and ultrasonication for about 90 minutes to achieve a homogeneous dispersion and freeze-dried. For working electrodes, the slurry contains

78% of Si/PVP composite, and 20% of PAN solution ($M_w=150.000$, Sigma-Aldrich Co, dissolved in DMF at 5wt% PAN) and 2% of GO that used as oxidizing agent. The mixture was mixed under magnetic stirring and ultrasonication at room temperature for 30 minutes to achieve a homogeneous distribution of the electrode components. The slurry was coated on a copper foil current collector by doctor-blading (**Figure 4.1**) and dried in a convection oven at 80 °C for 1hour, followed by drying in a vacuum oven at 85 °C for overnight. Electrodes were cut into circular discs of 1.2 cm diameter and the Si mass loading was typically 0.2 - 1.3 mg cm⁻². The electrodes were exposed to the SHT process using a quartz tube at two different temperatures, 450 and 750 °C, by slowly heating in Argon atmosphere and holding for 10 minutes, then followed by cooling. This treatment technique could form coherent shells that stabilized the SEI and improved the conductivity of the electrode materials by partially carbonizing the PAN binder leading to a flexible shell providing flexibility and porosity.⁷⁷ The optical images of the electrode before and after SHT with changing in the electrode color from brown to black color as shown in the **Figure S4.1, Appendix A**). The coin cells - type half cells (2032 type) with lithium foils (Aldrich, USA) was used as a counter electrode fabricated in the Ar-filled glove box (MBRAUN 10, USA) in argon atmosphere with water and oxygen content both under 0.5 ppm. The electrolyte composed of LiPF₆ (1M) in 30 wt% ethylene carbonate (EC), 60 wt% dimethyl carbonate (DMC), and 10 wt% fluorinated ethylene carbonate (FEC). A polypropylene separator was used to separate the positive and negative electrodes. Each coin cell contained ~ 40µl of the electrolyte.

4.3 Results and Discussion

Electrode fabrication and design are schematically shown in **Figure (4.2)**. To achieve an intimate contact between the carbon shell and the SiNPs, it is critical to ensure the intimate mixing and coverage of the carbon precursor with the SiNPs. By dispersing the PVP in water with SiNPs, an extremely stable suspension is obtained with PVP self-assembled into an intimate shell around the Si particles. After freeze-drying and homogenizing with a PAN solution in DMF and a small portion of GO, the slurry was cast onto a copper foil and dried. Then, the electrodes were inserted into the smaller tube and heated by SHT at temperatures of 450 °C and 750 °C. The SHT induces a chemical modification in the intimately wrapped PVP/PAN polymer blend and transforms it into a coherent, flexible, and conductive shell nesting the SiNP inside.

Figure 4.3 shows the morphology of the electrode materials at different stages which analyzed by TEM. **Figure 4.3b** reveals a thin layer over the Si nanoparticles, indicating that our envisioned intimate wrapping of PVP over Si particles was successful after freeze drying as schematically shown in **Figure 4.3c**. In addition, SEM images showing the morphology of Si/PVP after freeze drying which reveals that Si particles are embedded in the matrix of PVP polymer, and self-assembled in a leaf-like morphology (**Figure S4.2, Appendix A**). After mixing with PAN, the composite is shown in **Figure 4.3d-f** with little change in morphology. However, upon closer investigation, the new composite possesses a thicker shell of about 3 nm (**Figure 4.3f**) indicating the proper assembly of PAN over PVP/SiNP. After SHT at 450 °C, the TEM images of the treated electrode are shown in **Figure 4.3g-i** and after 750 °C are shown in **Figure 4.3j-l**.

Surprisingly, little morphological difference is found between the electrodes with or without heat treatment indicating that the as-designed structure is maintained after heat treatment at both 450 °C and 750 °C. Moreover, a thicker coating (~ 4 nm) as shown in **Figure 4.3i** was found on

the surface of all SiNPs after heat treatment at 750 °C when compared to the only about 3 nm coating of the 450 °C sample, which we believe is a result of more SiO₂ layer.

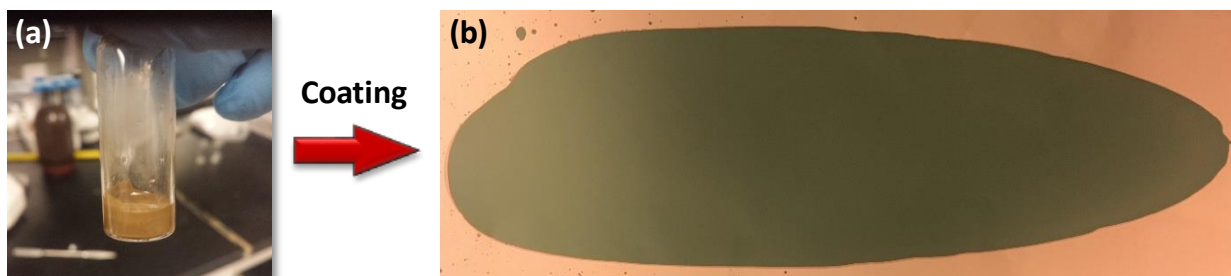


Figure (4.1) The materials slurry before and after casting on the copper foil.

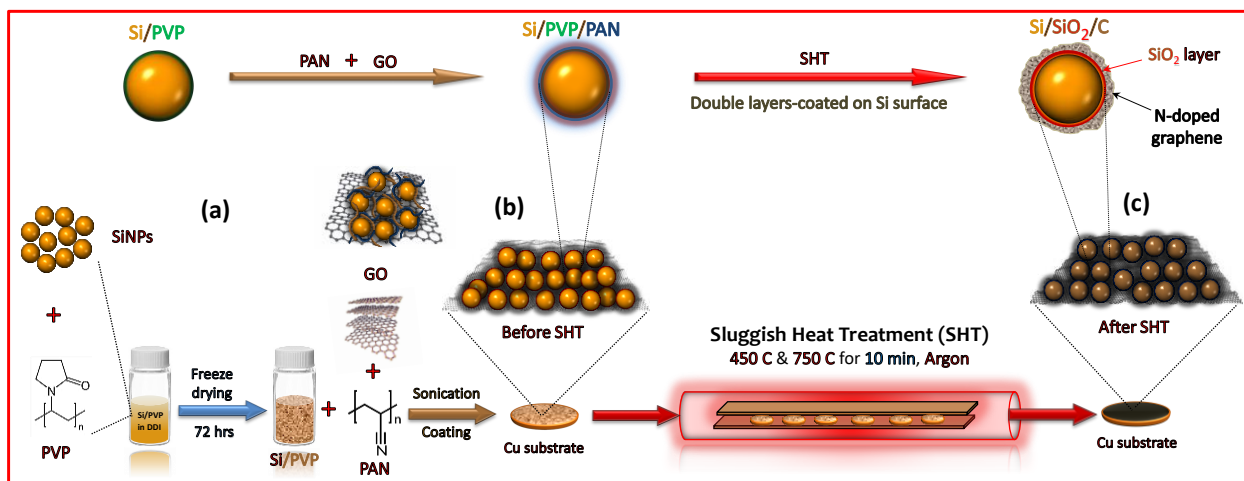


Figure (4.2) A schematic showing the fabrication procedure of the electrode: (a) synthesis of the electrode from SiNP, PVP, PAN, and GO before coating on Cu foil, (b) electrode before SHT, and (c) electrode after SHT.

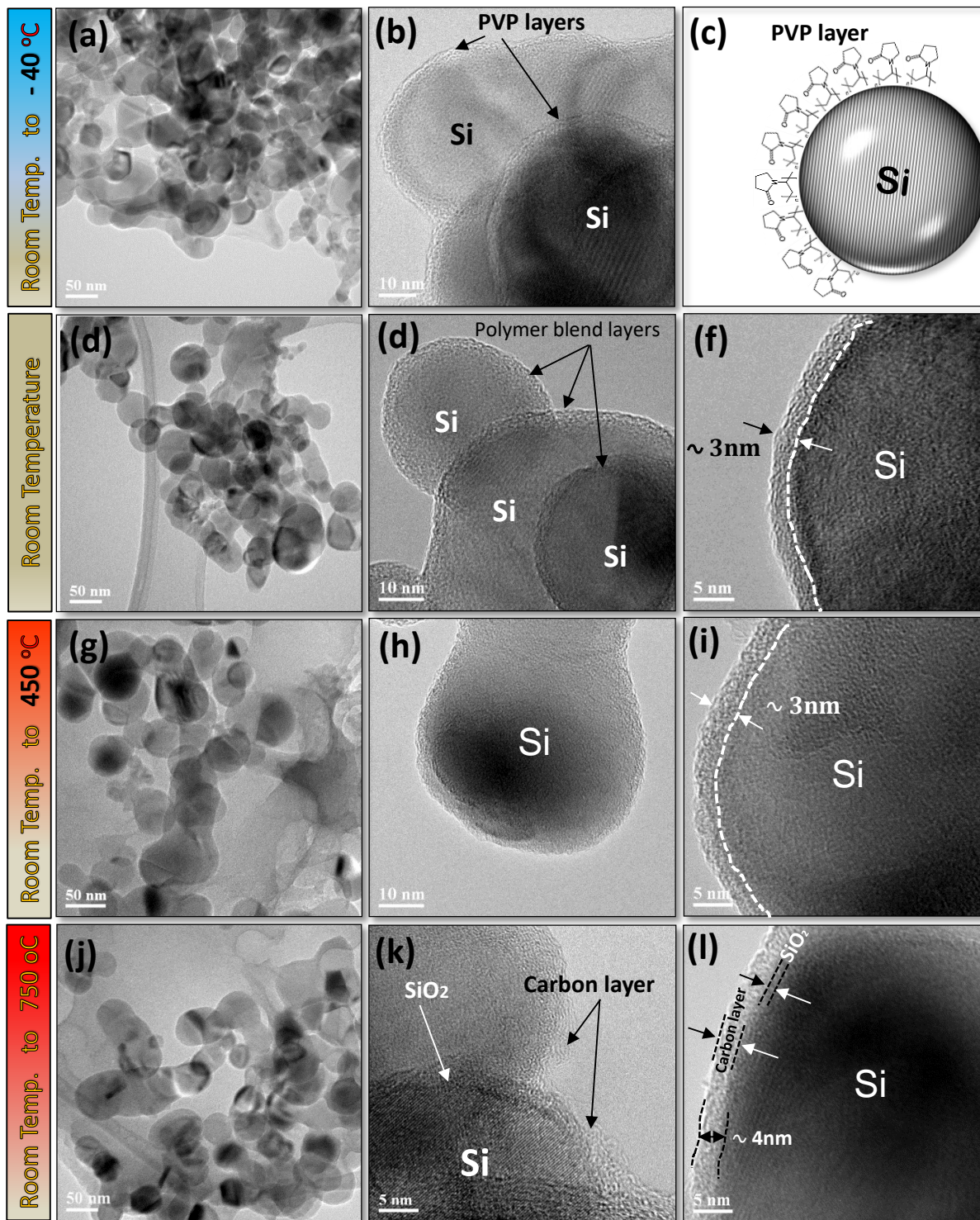


Figure (4.3) (a-b) TEM image of Si particles coated of PVP, (C) a schematic of PVP layer coated the Si particle, (d-f) TEM images of the Si/PVP/PAN electrode before SHT, (g-i) TEM images of the Si/PVP/PAN electrode treated at 450 °C, and (j-l) TEM images of the Si/PVP/PAN electrode treated at 750 °C.

Energy dispersive spectroscopy (EDS) elemental mapping was performed on the electrodes at all conditions. Without heat treatment, **Figure 4.4 (a1 -a3)** reveals that the carbon and oxygen distribution is not well defined with respect to the Si mapping for the area marked in **Figure 4.4a**. However, when the sample is treated at 450 °C (**Figure 4.4b**) and 750 °C (**Figure 4.4c**), the distribution of both carbon (**Figure 4.4 (b2)** and (**c2**)) and oxygen (**Figure 4.4 (b3)** and (**c3**)) appears to be abundant in places where there is no Si (**Figure 4.4 (b1)** and (**c1**)). In addition, the EDS line scan results confirm the presence of the C, O, and N elements within the coating for both electrodes treated at 450 and 750 C as shown in **Figure S4.3, Appendix A**. Furthermore, when the 750 °C heat treated electrode is mapped with electron energy loss spectroscopy (EELS), a very clear concentration of both carbon (**Figure 4.4 (d2)**) and oxygen signals (**Figure 4.4 (d3)**) can be found at the edge of the Si particles for the area marked in **Figure 4.4 (3c)**. This indicates that Si particles have a double coating of amorphous carbon and possibly an oxygen-rich, thin Si film. Moreover, x-ray photoelectron spectroscopy (XPS) of Si 2p (**Figure 4.4e**) shows that the Si in the sample treated at 750 °C is significantly more oxidized with stronger peaks at the higher binding energy levels compared to the untreated and 450 °C heat treated samples. The combination of a carbon and the SiO₂ shell around the Si particles as illustrated in **Figure 4.4f** will mitigate the negative effects of Si pulverization during cycling leading to improved cycling stability.⁹⁴

DSC results (**Figure 4.5**) indicate that PVP has a melting point around 100 °C which is much lower than 450 °C. As expected, pure PAN did not have any endothermic peak, but showed a sharp exothermic peak at 300 °C corresponding to the cyclization of nitrile groups in PAN structure by a free radical reaction of the nitrile group ($C\equiv N$). However, pure PVP did not have any exothermic peak but showed a small melting peak at around 100 °C and what appears to be another endothermic peak starting at ~ 380 °C, which is associated with the decomposition of PVP.⁹⁵ After incorporating PAN in the electrode materials, the DSC results show some changes in endothermic peaks with the samples. Samples with PAN displayed clear exothermic peaks in the range from 297 to 302 °C due to the free radical cyclization reaction of the nitrile group ($C\equiv N$) present in the structure of PAN.⁹⁶⁻¹⁰⁰ Interestingly, the endothermic peaks of samples with both PVP and PAN are delayed to a higher temperature. This is mostly because PVP is miscible with PAN polymer and a result of interaction between the proton acceptor of PVP and α -hydrogens of PAN.^{97, 101, 102} This is clearly demonstrated by the carbon layer in TEM images after adding PAN to the electrode materials as shown in **Figure 4.3d** with no phase separation appearing. From the DSC curve, it is clear that the cyclization peak of PVP/PAN is much broader than that of pure PAN which is in alignment with previous studies.¹⁰³

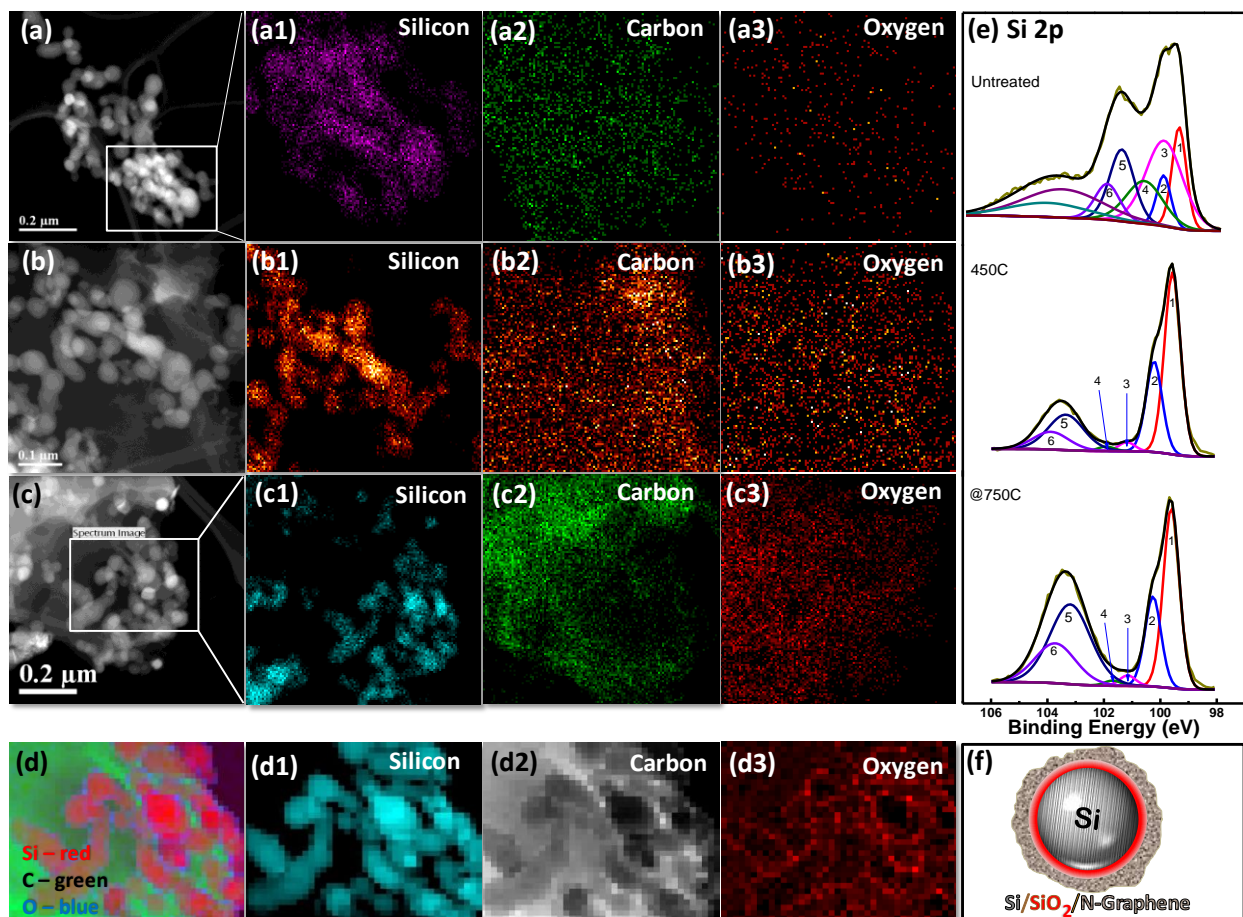


Figure (4.4) (a) Higher magnification TEM image of several SiNPs before SHT, (a1-a3) corresponding elemental mapping of Si, C and O of the area selected in the image (a), (b) TEM image of the electrode surface treated at 450 °C, (b1-b3) corresponding EDS elemental mapping of Si, C, and O of the image (b), (c) TEM image of Si particles treated at 750 °C, (c1-c3) corresponding EDS elemental mapping of Si, C, and O of the area marked in the image (c), (d) EELS elemental mapping of Si (red), C (green), and O (blue), (d1-d3) the elements mapping by EELS for the area selected in the image (c), (e) high-resolution XPS of Si 2p spectra of the electrode materials before and after SHT, and (f) a schematic showing the core Si particle with the surrounding layers of SiO₂ and N-doped graphene.

Raman spectroscopy was performed on electrodes before and after SHT to identify the chemical structure of the electrode materials (**Figure 4.6**). A clear difference between the samples can be recognized. The characteristic carbon peaks appeared at 1342 and 1576 cm^{-1} after SHT, which match well to the ‘D’ and ‘G’ bands, respectively. As expected, the D and G band intensities increase with increasing temperature indicating a higher degree of the carbonization. These graphitized carbon are related to the cyclization of PAN during SHT.⁷⁷ Interestingly, the Si peak was found to be shifted towards a smaller wave number, which stems from the surface stresses induced by the formation of a shell of SiO_2 and the carbon materials.^{77, 104, 105} Two small peaks at 290 and 930 cm^{-1} were also found which we believe is associated with Si–O–Si banding and Si–OH stretching on the Si surface, respectively.^{94 104, 106, 107} Furthermore, **Figure 4.7a** shows the high-resolution XPS binding energy spectra of carbon C 1s before and after SHT at both temperatures. Peak (1) located at 284.9 eV corresponding to the sp^2 hybridization of PAN into a graphitic type carbon.^{77, 108-113} On the other hand, peak (2) is centered at 286.5 eV may be assigned to the carbon atoms bonded to nitrogen in C–N bonds.¹¹⁴ With temperature increase, the intensity of peak (2) is decreased, which reveals a significant transformation of the polymer structure. Peaks (3-5) centered at range of 287.5 to 290.5 eV, are attributed to oxygenated carbon in the polymer matrix.¹¹⁵⁻¹¹⁹ The high-resolution spectra of N 1s (**Figure 4.7b**) was divided into main three components of nitrogen differentiated by their binding energies at 398.7, 400, and 401.3 eV which are associated with the pyridinic-N, pyrrolic-N, and graphitic-N forms of nitrogen, respectively.^{120, 121} The relative content of the pyridinic-N, graphitic-N, and graphitic-N structures likely increased during the heat treatment due to the relative thermal stability of each form. However, the existence of nitrogen groups after high temperature (750 °C) heat treatment allows for these groups to act as electronegative sites for electrostatically hindering any migration of SiNP during cycling. These

results are in good alignment with the cyclization mechanism of PAN and its transformation into a N-rich graphene-like structure (**Figure 4.7c**).

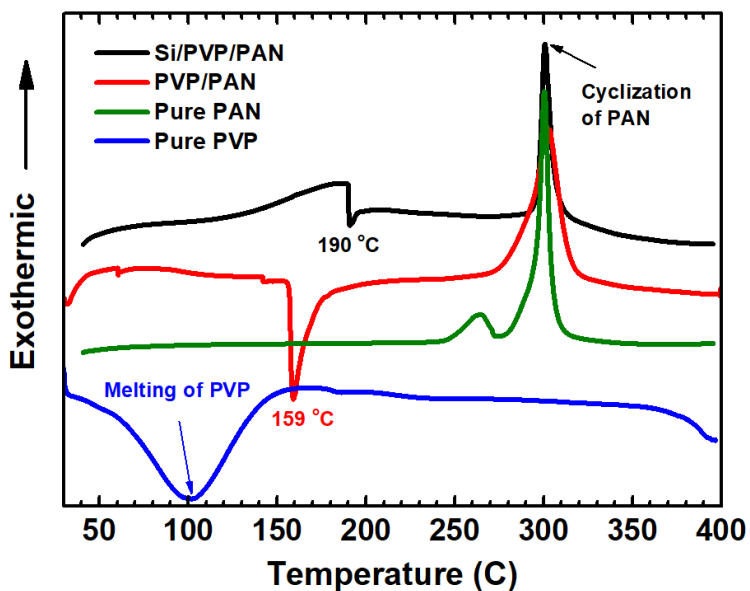


Figure (4.5) DSC analysis of the electrode materials, pure PVP, pure PAN, PVP/PAN, and Si/PVP/PAN in nitrogen.

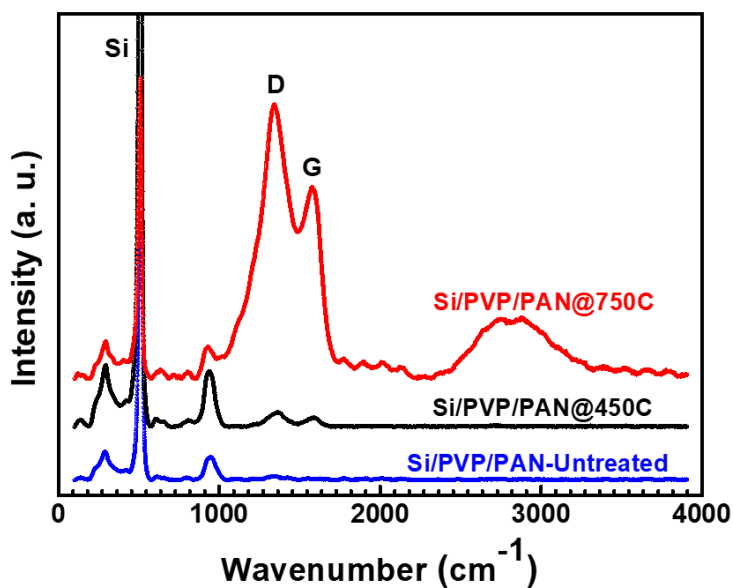


Figure (4.6) Raman spectrum of three electrode materials, Si/PVP/PAN-untreated, Si/PVP/PAN treated at 450 C, and Si/PVP/PAN treated at 750 C.

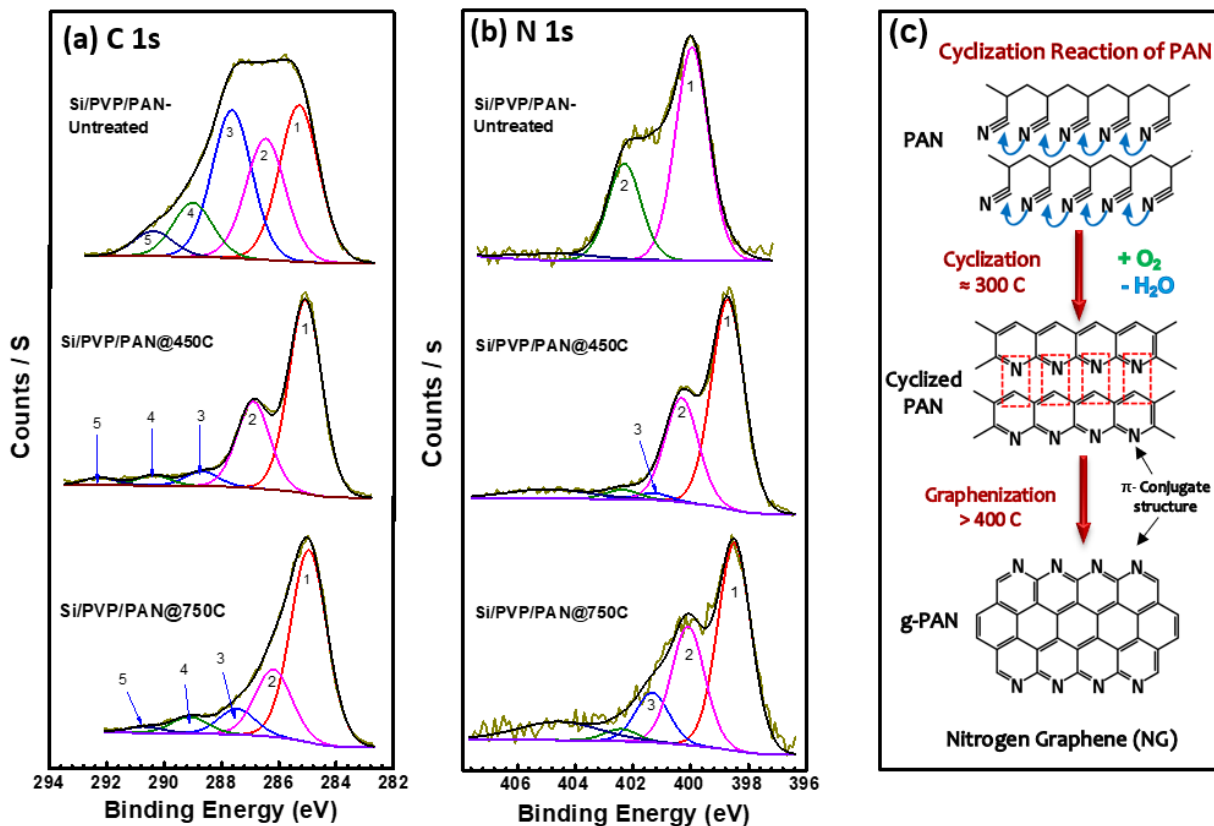


Figure (4.7) High-resolution XPS spectra of the electrode materials for (a) C 1s and (b) N 1s, and (e) a schematic of the cyclization mechanism for PAN.

To illustrate charge storage performance, the coin cells that were made with treated electrodes characterized by cyclic voltammetry (CV) as shown in **Figure 4.8a**. The CV curves for the electrode treated at 750 °C reveal the activation process of the electrode for five cycles within the voltage window of 0.01 V and 1.5 V at a scanning rate of 0.05 mV s⁻¹. The CV curve of the first cycle (black line) is apparently dissimilar to the following cycles. Two oxidation peaks are observed at 0.38 and 0.53 V (versus Li⁺/Li) during the charging branch, which indicate the lithium extraction process in Si.⁷⁷ During the discharging branch, the peak at 0.2 V starts at the second cycle, which is absent in the first cycle, which suggests the transformation from crystalline Si to amorphous phase Li_xSi.^{24, 77} With cycling, all peaks become stronger and sharper, which is a

common property for the transition from crystalline Si to amorphous Si due to lithiation/delithiation processes.^{13, 94, 122} The electrochemical performances of the treated electrodes were tested using galvanostatic cycling at room temperature with lithium metal as the counter electrode. In all the electrochemical tests, the potential range was set to 0.01–1.10 V (versus Li⁺/Li). **Figure 4.8b** displays the discharge/charge cycling behavior of the electrodes treated at 450 and 750 °C tested at a low current rate of 100 mA g⁻¹ for the first five cycles before shifting to the current of 500 mA g⁻¹ for 70 cycles. Under 100 mA g⁻¹, the electrodes at 450 and 750 °C delivered initial charges of 3128 and 2476 mAh g⁻¹, which correspond to a respective Coulombic efficiency of 82% and 80%, respectively. After the second cycle, the Coulombic efficiency rapidly increases up to ~98% and remains stable for 70 cycles. The capacity retention of the electrodes at 750 °C possessed a superior cycle retention when compared to the higher capacity of 450 °C, which demonstrates the importance of our designed layer of SiO₂. In addition, we investigated the rate capability of Si electrodes treated at 450 and 750 °C at different current rates from 100 to 4000 mA g⁻¹ as shown in **Figure 4.9a** with corresponding galvanostatic charge/discharge profile showing capacity dependence on cycle numbers (**Figure 4.9b**). Both electrodes have an excellent rate capability even at a high current rate of 4000 mA g⁻¹. They were cycled at a rate of 100 mA g⁻¹ for the first five cycles followed by rate capability at different current densities. The electrode treated at 450 °C displayed highly stable reversible capacities of about 3096, 2836, 2633 and 2270 mAh g⁻¹ obtained at current rates of 1000, 2000, 3000 and 4000 mA g⁻¹, respectively. Moreover, a flat voltage plateau in the discharge/charge curves were also observed even at a high current density of 4000 mA g⁻¹, then the electrode was able to regain a capacity of 2723 mAh g⁻¹ at a current density of 2000 mA g⁻¹. In contrast, the electrode treated at 750 °C also displayed a good rate capability but at lower capacities due to our designed partial conversion of Si into SiO₂. This

drastic stability and capacity difference between the 450 °C and 750 °C treated electrodes indicates the significance of the surface oxidation of Si in SiO₂ through the incorporation of an intimate layer of oxygen-containing PVP. The decrease in capacity of the 750 °C electrode is most likely due to the previously mentioned oxidized Si (i.e. SiO₂).

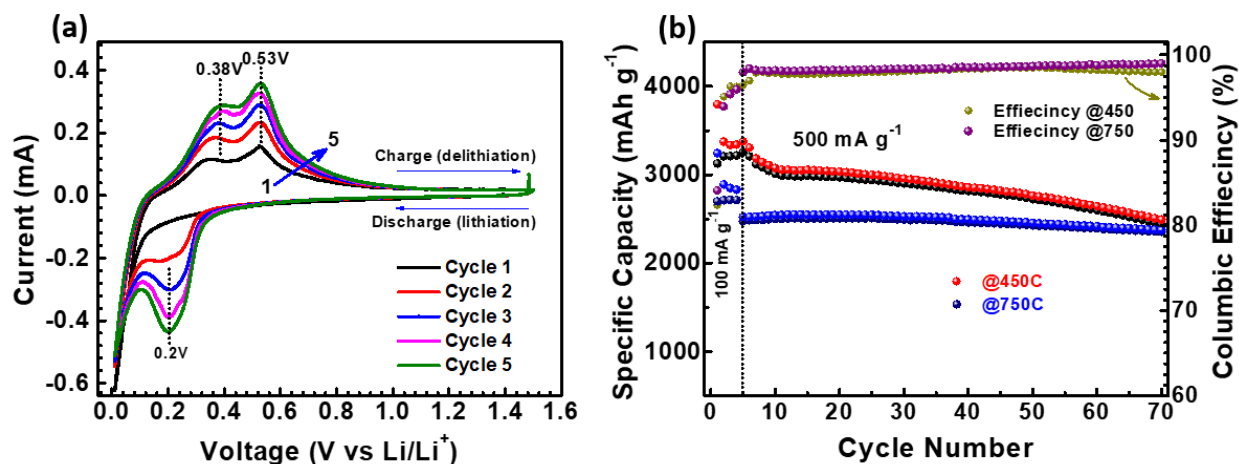


Figure (4.8) Electrochemical characterization of Si electrodes: (a) CV curve for a coin cell was treated at 750 °C and measured at scan rate of 0.05 mV s⁻¹ between 0.01 and 1.5 V (vs Li⁺/Li), (b) Cycling stability of the electrodes treated at 450 and 750 °C at 100 mA g⁻¹ and 500 mA g⁻¹.

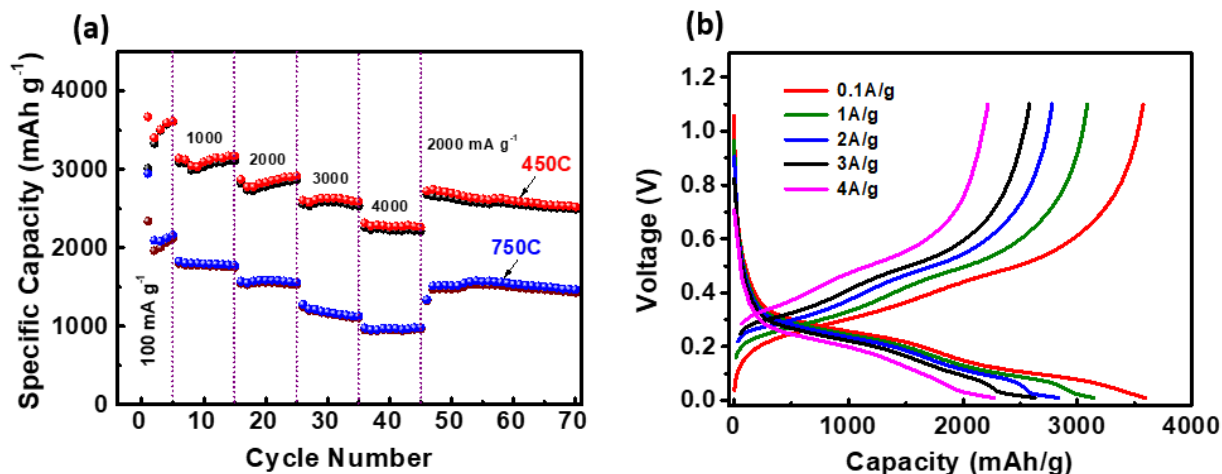


Figure (4.9) Electrochemical characterization of the Si electrodes: (a) Rate capability of the electrodes treated at 450 and 750 °C, (b) voltage profile of Si electrode treated at 450 C and tested at different current rates.

As shown in **Figure 4.10**, the impedance of the electrode treated at 450 °C has a higher impedance than that of the electrode treated at 750 °C, which suggests that the difference in capacity is independent of the impedance of these cells. Since the electrode treated at 750 °C possessed a low impedance, this suggests that the difference in specific capacity is truly due to the transformation of Si into SiO₂. Additionally, it is worth noting that the charge transfer resistance of the nontreated Si/PVP/PAN and the traditional SiNPs (60%), PVDF (20%), and Super P (20%) electrodes without SHT was significantly higher than of our modified electrodes and illustrates the main advantage of SHT on electrodes.

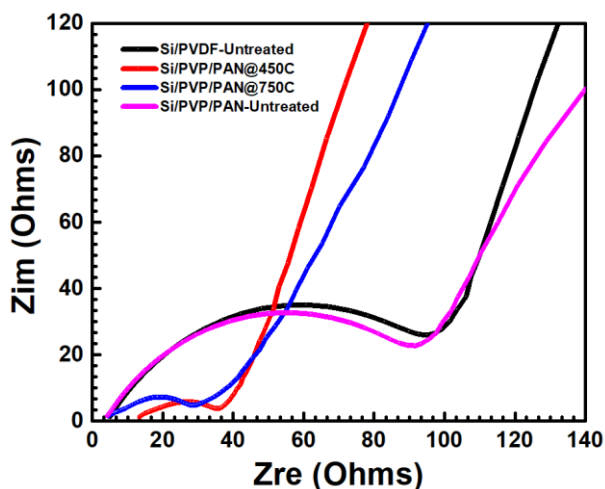


Figure (4.10) Electrochemical impedance measurements of the Si/PVP/g-PAN treated at 450 and 750 C, Si/PVP/PAN non treated, and Si/PVDF/Super P after 50 cycles.

We also further compared the cycling behavior of the Si/PVP/PAN electrode based on different temperatures at 450 and 750 °C to the SiNP/PVDF/Super P electrode as shown in **Figure 4.11**. The reference electrode of the SiNP/PVDF/Super P demonstrated lithiation capacity of 3004 mAh g⁻¹ in the initial cycle at 100 mA g⁻¹ which shows a poor cycling performance suffering fast capacity decay to almost zero capacity at a current 2000 mA g⁻¹ (green line). This fast decay is associated with the fracturing of the Si layer caused by expansion of Si particles during repeating cycling. Although the reversible capacity for the electrode treated at 450 °C exhibits a better cycling performance than the reference electrode, it still shows a capacity loss from an initial reversible capacity of 2746 mAh g⁻¹ fading to 1781 mAh g⁻¹ at 2000 mA g⁻¹ for 200 cycles with 99.8% of coulombic efficiency and with a capacity retention of 65%. Once again, the electrode treated at 750 °C observed excellent cycling stability at 2000 mA g⁻¹ for 200 cycles after first five cycles at a low current rate of 100 mA g⁻¹ with a capacity retention of 85% while possessing a relatively lower capacity compared to the 450 °C electrode. Both treated electrodes exhibited almost similar coulombic efficiency (99.8%) up to 200 cycles at current 2000 mA g⁻¹. Furthermore, **Figure 4.12** showed the long-term cycle performance and Coulombic efficiency of another treated electrode at 750 °C and cycled at high current rate 3000 mA g⁻¹ for 600 cycles after an activation process at 100 mA g⁻¹ for the first five cycles. As is observed, the Si electrode treated shows initial charge and discharge capacities of 2209 and 2736 mAh g⁻¹, respectively with a Coulombic efficiency of 80% in the first cycle. This improvement of the lithium storage properties of the electrode treated at 750 °C is mainly related to the formation of the SiO₂ film and the N-doped graphene on the Si particles surface.

The SiO₂ film coating can be played to provide a mechanically strong structural coating over the Si particles, while the lithium ions are still allowed to cross through during the lithiation processes. To further confirm the effect of PVP, battery performance of electrode without PVP were fabricated and tested (**Figure S4.4, Appendix A**). It is evident that without the incorporation of PVP, the Si/PAN electrode had a significantly poorer performance with severe cycle decay. In addition, Si/PVP electrode was fabricated without PAN and treated at 750 °C, which tested at the same conditions. This electrode also delivers poor performance as shown in **Figure S4.5, Appendix A**. This, in combination with the drastic differences in cycling performance between the 450 and 750 °C provides strong evidence that the blend of PVP with PAN as carbon precursor played a crucial role in improving the electrochemical performance of the Si electrode.

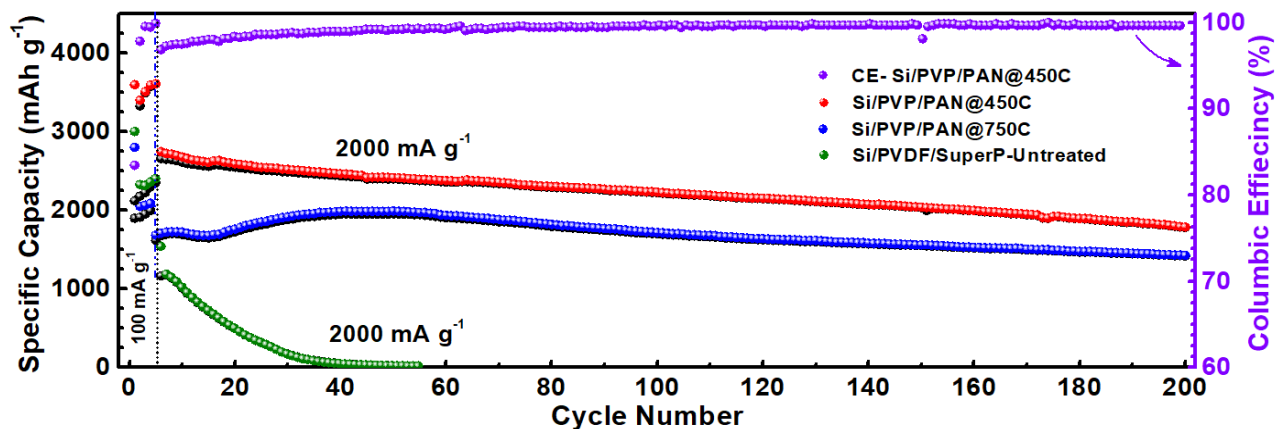


Figure (4.11) Cycling behavior of the Si/PVP/PAN electrodes treated at 450 and 750 °C at 100 mA g⁻¹ for the first five cycles and 2000 mA g⁻¹ for the following cycles with Si/PVDF/Super P.

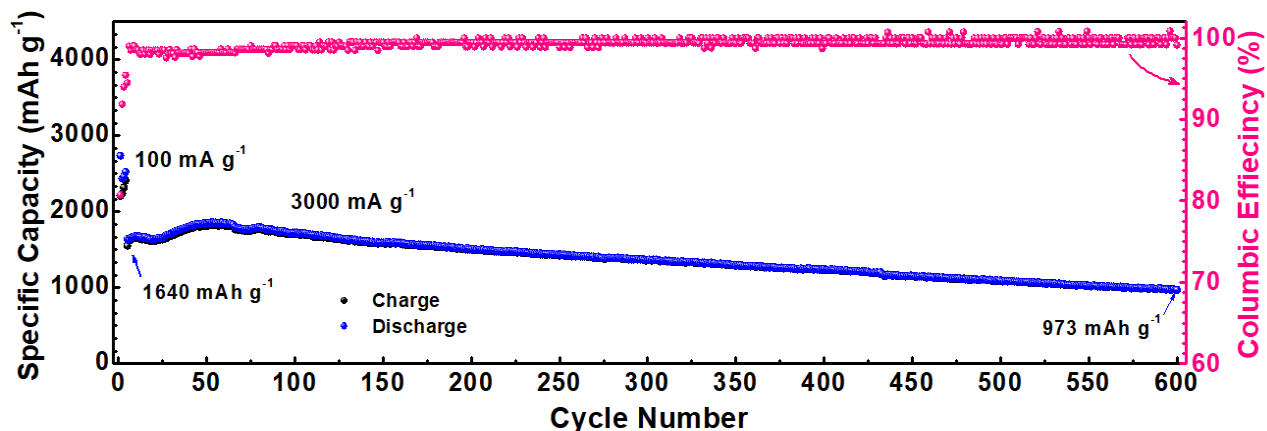


Figure (4.12) Long-term cycling stability of Si/PVP/PAN treated at 750 °C and cycled at 100 mA g⁻¹ for five cycles and at 3000 mA g⁻¹ for another 600 cycles.

Figures 4.13 a and b show HRTEM with corresponding the EELS elemental mapping for the Si, C, and O elements before and after 600 cycles, respectively. Before cycling, a clear concentration of O and C signal is found surrounding the Si particles. After cycling, the coating of O and C appeared to have disappeared which is to be expected after extended cycling. However, no aggregation of Si was found, and the scattered amorphized SiNPs are still hosted in the nitrogenized carbon framework. The SiNPs are still uniformly hosted in a cage of nitrogenated carbon after polymer carbonization. This suggests the strategy at which the electrode keep cycling with minimal loss in capacity.

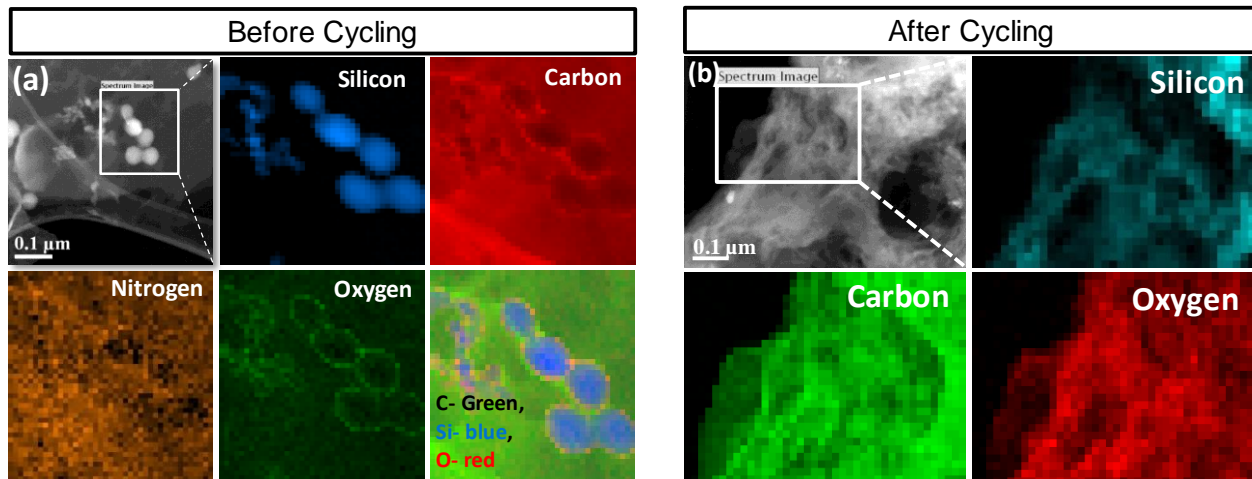


Figure (4.13) Characterization of the electrode material before and after cycling for 600 cycles: (a) HRTEM image of the surface electrode treated at 750 °C and before cycling with corresponding to the elements (O, C, N, and Si) mapping by EELS for the area marked in the image (a), (b) HRTEM image of the electrode after cycling corresponding to the elements (O, C, and Si) EELS mapping for the area marked in the image (b).

In summary, a high-performance Si anode was synthesized by adopting a PVP/PAN polymer blend followed by a facile and economical slow heat treatment process. Different characteristics of the samples with and without PVP elucidated interesting mechanism of the formation of the coatings on Si. The self-assembled PVP shell around the Si allowed for an amplified oxidation of Si producing a robust SiO₂ shell while the decomposition of PAN introduced a nitrogen rich carbon coating over the SiO₂. When combined with a conductive graphene network, this material was able to deliver excellent cycle stability with average capacity of 1306 mAh g⁻¹ and a cycle retention of 60 % over 600 cycles at a higher current density of 3000 mA g⁻¹ as well as excellent rate capability.

Chapter 5. Multifunctional Nano-Architecting of Si Electrode for High-Performance Lithium-ion Battery Anode

This chapter is based on published manuscript to JMCA by Elhadi Attia et al.

Journal of The Electrochemical Society, 166 (13) A2776-A2783 (2019).

“Multifunctional Nano-Architecting of Si Electrode for High-Performance Lithium-ion Battery Anode”

5.1 Introduction

The realization of energy storage devices with high energy density and low cost is among the world’s greatest scientific challenges. As introduced in chapter two, lithium-ion batteries are considered to be one of the most powerful energy storage technologies owing to their high gravimetric energy density.^{123, 124} Also, Si is a promising anode material candidate for increasing the energy density of the LIBs due to its high output voltage and theoretical specific capacity when compared to the commercial graphite materials.^{69, 125-127} However, Si anodes still suffer from rapid capacity decay upon cycling, which can be attributed to the immense volume change upon lithiation and the subsequent structural deformation and loss of electrical contact.¹²⁸⁻¹³⁰ Furthermore, this also results in the constant exposure of fresh surfaces of Si particles to the electrolyte, causing an unstable SEI during cycling.^{131, 132} These issues result in the rapid degradation of Si electrodes, nullifying any benefits of Si for LIBs.¹³³

Over the past decade, several efforts have been devoted to overcoming the problems associated with the volumetric changes of silicon materials. Surface coatings of silicon and the use of Si-interactive binders have been the focus of a large volume of research.¹³⁴⁻¹³⁸ Specifically,

physical coatings are believed to mitigate the pulverization problem of silicon by limiting the contact of a newly formed silicon surface with the electrolyte in addition to mostly preserving the electrical network. Additionally, Si-interactive binders such as polyacrylic acid (PAA) and sodium carboxymethylcellulose (CMC) are preferable for Si-based anodes. This is due to the large quantity of -OH and -COOH groups in CMC and PAA, which can strongly interact with the oxide layer on the Si surface.^{139, 140} This results in Si-based electrodes which are more capable of maintaining contact with Si particles and the conductive network over cycling i.e. holding the electrode together.¹³⁹⁻¹⁴¹ However, with increasing binder content and subsequent better mechanical robustness of the electrode, the lesser the contact the Si has with the conductive network (both ionic and electronic). While surface coating techniques can offer Si with direct contact to a conductive surface, the network once again lacks an overall medium to hold the electrode together throughout its volume expansion cycles. Interestingly, these separate strategies have been long accepted by the research community. However, a single solution that encompasses all of these design strategies into one system have yet to be demonstrated with high performance.

In this chapter, we have developed a method of Si anode nano-architecting where all of the aforementioned strategies (Si surface coating, strong Si interactive network, conductive network) are simultaneously achieved. Through a carefully designed slow heat treatment process (SHT), a 3D cross-linked robust structure (PAA-CMC) is formed *via* the condensation reaction between the PAA and CMC over the Si nanoparticles followed by its carbonization. Meanwhile, the SHT modify PAN polymer which provides graphenized PAN that formed a 2D architecture of nitrogen-doped graphene-like nanosheets (NG) which significantly improved the ionic and electronic conductivity of the electrode. The blending of these materials formed a stable synthetic SEI layer, providing a flexible surface passivation of the Si particles throughout the volume fluctuation over

cycling. Using this design strategy, the as-obtained robust electrode architecture formed by the cross-linking (PAA-CMC) with graphenized PAN (g-PAN) yielded significantly improved cycling stability of 650 cycles.

5.2 Experimental Work

5.2.1 Preparation of Si electrode:

To fabricate the electrode for LIB testing, the commercial nanosize silicon (NSi) with 50 to 70 nm of diameter was purchased from Nanostructured & Amorphous Materials, Inc. (Houston, TX). PAA polymer ($M_w = \sim 1,250,000 \text{ g mol}^{-1}$), CMC polymer ($M_w = \sim 250,000 \text{ g mol}^{-1}$), and PAN polymer ($M_w = \sim 150,000 \text{ g mol}^{-1}$) were bought from Sigma-Aldrich Co. **Figure 5.1** schematically shows the electrode fabrication technique and binder design. To achieve a good dispersion between PAA and CMC copolymers, first, we dissolved 50 wt.% PAA and 50 wt.% CMC polymers in about 15 ml of deionized distilled water (DDI) under sonication with stirring at 45 °C with rpm of 250 for about 10 h to achieve a gel-like well-mixed solution. Second, SiNPs as active materials were added to PAA/CMC mixture and mixed well using ultrasonication and stirring for 1h to achieve self-assembly onto the surface of SiNPs. Subsequently, the mixture was frozen directly in liquid nitrogen under vacuum for about 72h, which can conserve the original morphology of Si particles with coating polymers to make a core-shell Si. Then, for the working electrodes, the slurry contained 75% of NSi/PAA/CMC composite and 25% of PAN dissolved in DMF solution without any conductive additives. To achieve an excellent distribution of PAN polymer around the composite of NSi/PAA/CMC, the slurry was mixed using a planetary centrifugal mixer (THINKY, AR-100) at a high speed of 10000 rpm at room temperature for 10 min followed by 10 min of ultrasonication. The slurry was then spread on Cu foil as a current collector by a doctor blade and

dried in the air at room temperature for 60 min to remove the water, followed by drying in convection oven at 75 °C for 60 min, then heating in vacuum oven at about 80 °C for about 10 h. Next, the electrodes were punched with 12 mm diameter disks. The average mass loading of Si material was 0.6 – 1.2 mg cm⁻². Finally, the Si electrodes were subjected to the SHT process by slow heating with a ramp rate of ~ 1.3 °C min⁻¹ and held at 450 °C for 10 min in Argon atmosphere, then followed by slow cooling as shown in **Figure 5.2**. This SHT technique could change the chemical structure of polymers leading to generate a coherent structure, which can stabilize the SEI layer and improve the electrical conductivity of Si anode. Similar procedures of SHT process to fabricate reference electrodes of NSi/PAA-CMC (6:4) and NSi/PAN (6:4). Another electrode fabricated from NSi/PVDF/Super P (6:2:2) as a conventional binder for LIBs.

5.3 Results and Discussion

Figure 5.1 presents a schematic of the design and fabrication technique of the SHT process. The mixing technique of the electrode materials is considered a critical step to achieve proper coverage of the Si particles and to ensure the intimate coating on the SiNPs. During the gradual heating of SHT, a 3D cross-linked structure was formed between the hydroxy moieties of CMC and the carboxylic acid groups of PAA polymeric materials by a condensation reaction.¹⁴⁰ In addition, the free carboxylic acid groups of PAA react with the hydroxy groups of the SiO₂ layer on the Si surface to form a covalent ester bond. This strong chemical bonding forms an effective network, which could effectively prevent the mechanical deterioration of the electrode structure by the volume change of Si particles.¹³⁹⁻¹⁴¹

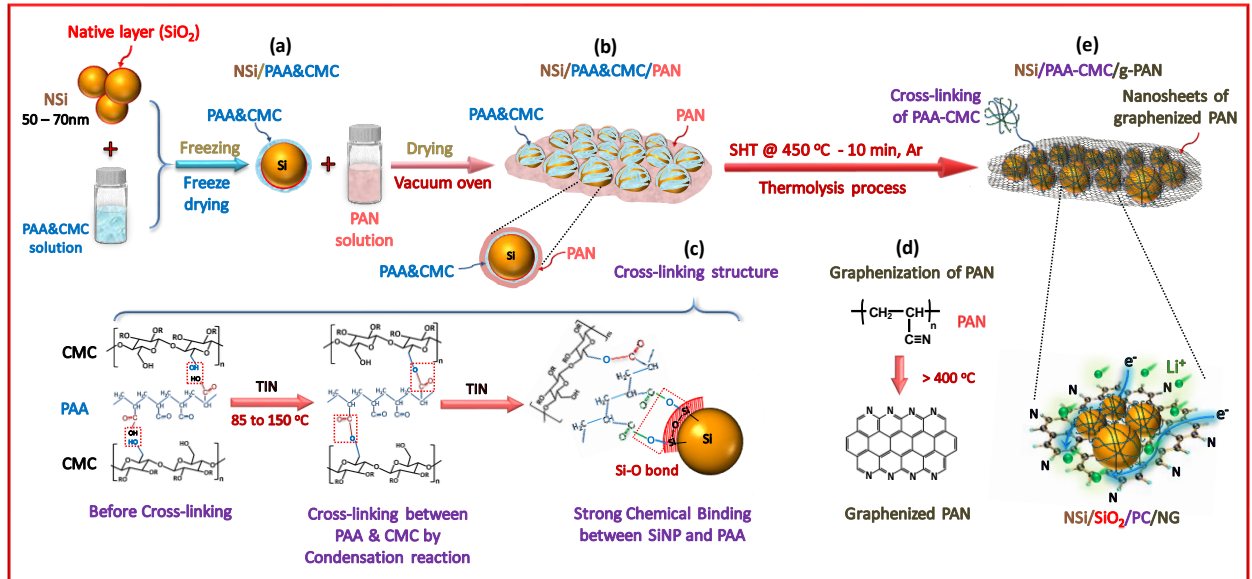


Figure (5.1) A schematic illustration of the design procedure of the nanostructured electrode materials; (a) NSi particles covered by PAA/CMC layer after freeze-drying, (b) NSi/PAA/CMC covered by PAN polymer before SHT process, (c) cross-linking of PAA-CMC *via* the condensation reaction between CMC and PAA. Covalent binding between PAA-CMC binder and NSi is formed during the SHT process; (d) graphenization of PAN during the SHT, and (e) NSi/PAA-CMC/g-PAN composite after SHT process.



Figure (5.2) A Schematic showing optical images for the electrode surface before and after the slow heat treatment.

The morphology and the surface structure of the Si composite were observed at different stages by SEM and TEM. The magnified image (**Figure 5.3b**) shows a native oxide layer (SiO_2) on the surface of Si particles with a thickness of approximately 3 nm. As shown in **Figure 5.4a**, the low magnification TEM image for an overview of a few SiNPs displays well dispersed in PAA/CMC copolymers after freeze drying. Moreover, the high-resolution transmission electron microscopy (HRTEM) images (**Figure 5.4b-c**) confirm that SiNPs are very well encased by an outer coating of PAA/CMC layer, which indicates that our coating by PAA/CMC after freeze-drying was successful. After mixing with PAN, Si particles are completely covered by PAN precursor (**Figure 5.4d**). Interestingly, the thickness of the shell around the Si particles was increased, which indicates that the PAN is coated over the PAA/CMC layer on SiNPs surface (**Figure 5.4e-f**). SEM images (**Figure S5.1a-b, Appendix A**) reveal that there was no apparent morphology change before the SHT. However, after SHT process, an interconnected structure is formed, which contains conductive NG nanosheet network wrapped the Si particles, as shown in **Figure S5.1c-d, (Appendix A)**. In addition, the TEM image is presented in **Figure S5.2a, (Appendix A)** clearly illustrates that SiNPs were well-wrapped by NG nanosheets, which can act as conductor matrix to enhance the conductivity and a cushion to accommodate the huge volume change of Si particles during cycling. As shown in **Figure S5.2b, (Appendix A)** the post SHT electrode of NSi/PAA-CMC/g-PAN is flexible and remained integral under bending. More interesting, closer TEM images (**Figure 5.4h-i**) show that SiNPs are thoroughly coated by a thin layer of amorphous SiO_2 (~ 4nm in thickness) and wrapped by graphenized PAN nanosheets. This strategy suggests that the slow thermolysis technique successfully modified the chemistry of the polymers without any deterioration of the initial morphology of the electrode materials.

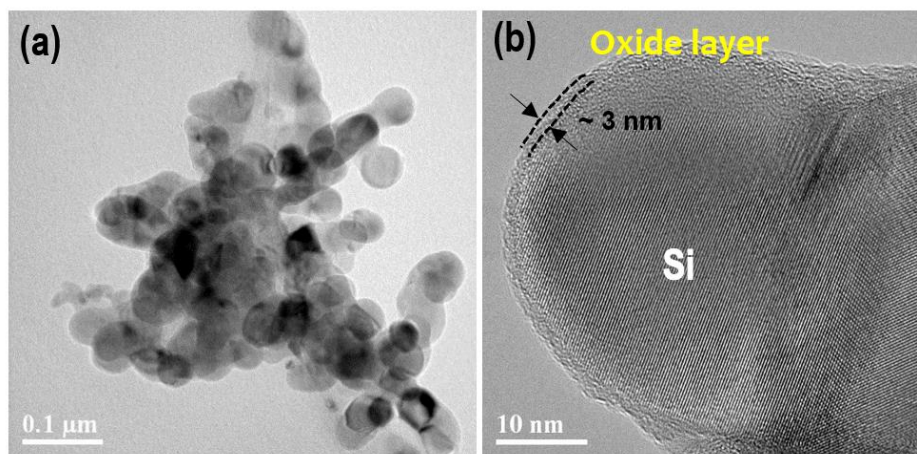


Figure (5.3) (a) TEM image of pure Si nanoparticles, (b) HRTEM image of the crystalline Si particle before coating with size of 50 to 70 nm showing a thin layer of SiO₂.

As confirmation, Si electrodes before and after SHT process were mapped by EELS as shown in **Figure 5.5** and (**Figure S5.3, Appendix A**). The distribution of oxygen before SHT is random and is not well concentrated around the edge of the Si particles as shown in **Figure 5.5a**. In contrast, after SHT, a clear concentration of oxygen film (red color) was found surrounding the edge of each Si particle, suggesting there is a SiO₂ layer over Si particles (**Figure 5.5b**). In addition, both carbon and nitrogen are found to be well distributed around the SiNPs. This illustrates that the SiNPs have a double coating of a thin layer of oxygen and amorphous carbon with nitrogen. We believe the abundance of oxygen species from the PAA and CMC polymer facilitated the oxidation of Si, while the nitrogen comes from the graphenized PAN.

Figure 5.6 displays the Fourier-transform infrared (FTIR) spectroscopy of the electrode materials. The FTIR spectra indicates that the original band of PAA at 1712 cm⁻¹, which corresponding to the C=O group, shifts to 1722 cm⁻¹ in PAA-CMC due to the formation of ester groups (COO) by the condensation reaction between the PAA and CMC, indicating the successful

cross-linking of the polymer network.^{139, 142, 143} Moreover, in the presence of the Si material with PAN polymer, the intensity of this band (COO) decreases significantly and shifted to 1720 cm^{-1} , indicating an interaction between polymer and the hydroxy groups on the Si surface.^{75, 144} After SHT, the C=O band completely disappeared, which may be due to the de-esterification reaction. A small stretching bond vibration at 2244 cm^{-1} is attributed to nitrile groups (C≡N) in the PAN structure.¹⁴⁵ This band also disappears after SHT due to the cyclization reaction of C≡N in the PAN chain, which confirmed that the cyclization reaction also took place inside the electrode materials during the SHT process.^{96, 98, 99} The DSC results of the electrode materials were consistent with the FTIR spectra. As shown in **Figure 5.7**, a sharp exothermic peak for the electrode materials at $\sim 300\text{ }^{\circ}\text{C}$ was related to the modification of PAN, which is the result of the cyclization reaction of C≡N in the PAN structure. This result is consistent with previous reports.^{96, 98, 99, 146-148} This is in good agreement with the TGA results of pure PAN for the initial weight loss at the same temperature (**Figure S5.4, Appendix A**). This also confirmed that the chain structure of PAN has changed from aliphatic linear to 2D structure analogical of the graphene-like structure due to the cyclization reaction.^{149, 150}

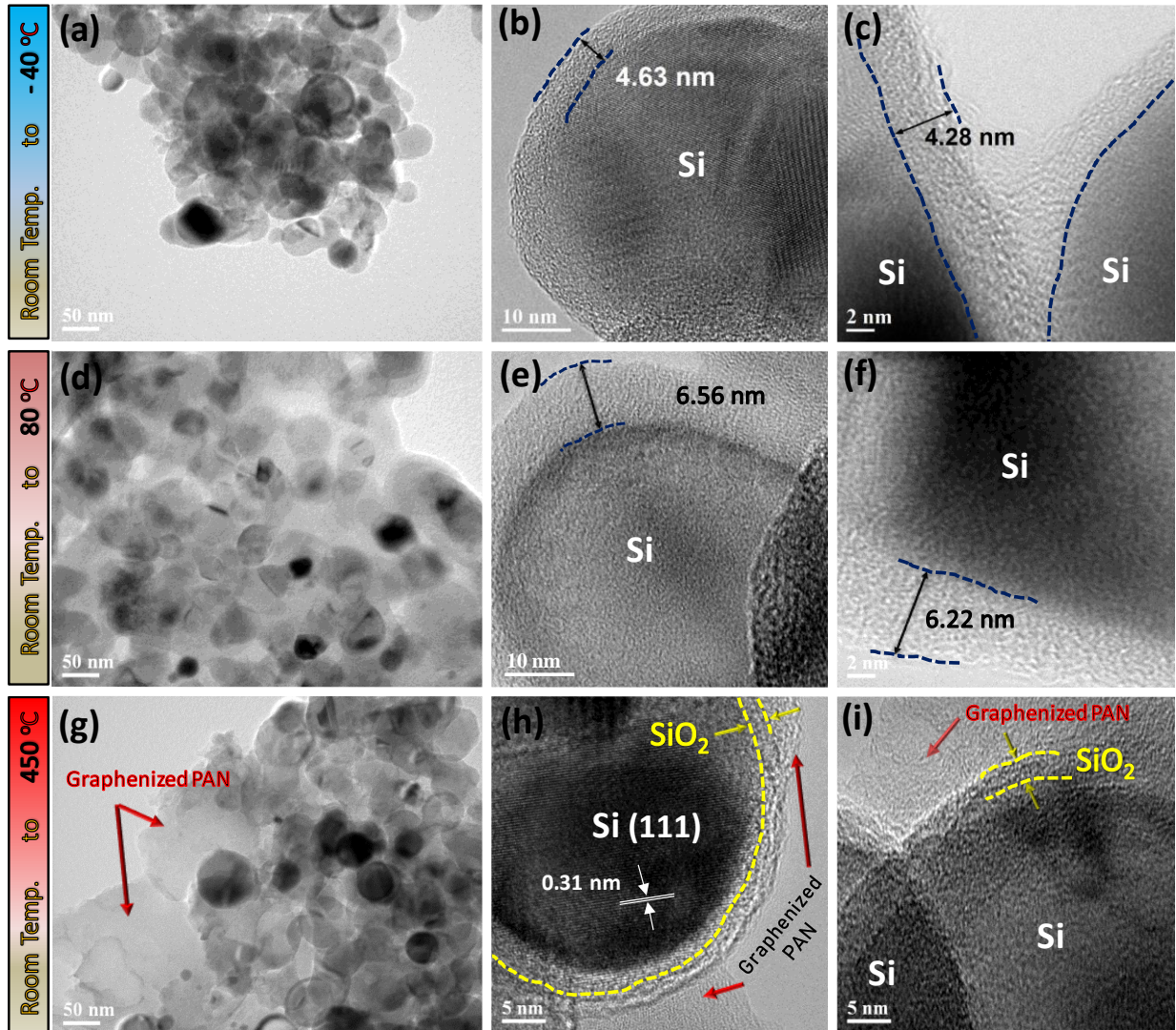


Figure (5.4) (a) TEM image of SiNPs covered by PAA/CMC polymers after freeze-drying, (b,c) HRTEM images of close Si particles wrapped by PAA/CMC layer, (d) TEM image of Si particles coated by PAA/CMC with PAN before the TIN, (e,f) HRTEM images of the NSi/PAA/CMC/PAN before SHT, (g) TEM image of NSi/PAA-CMC/g-PAN after SHT showing the Si particles wrapped by graphene nanosheets, and (h,i) HRTEM images of SiNPs coated by SiO₂ layer and graphenized PAN.

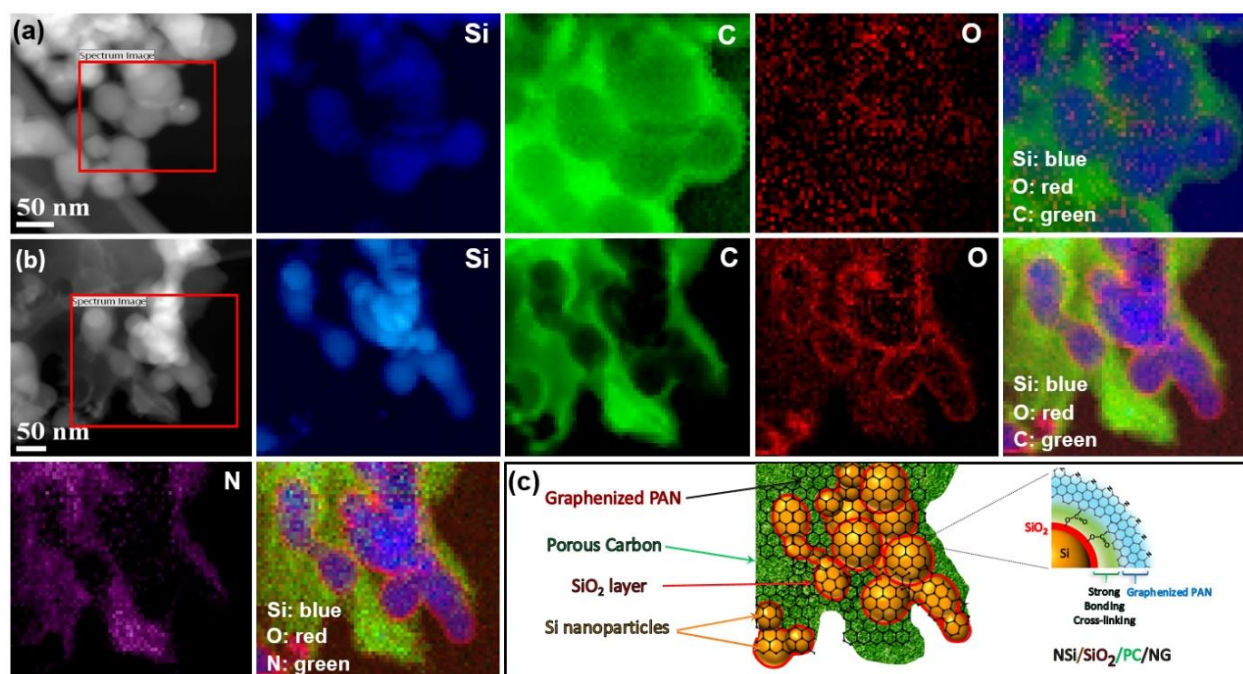


Figure (5.5) (a) HAADF-STEM image of the NSi/PAA/CMC/PAN material before SHT with its corresponding EELS mapping of (C, Si, O, and overlap elements) for the area selected in the red square in (a), (b) STEM image of NSi/PAA-CMC/g-PAN material after SHT with its corresponding EELS mapping for (C, Si, O, N and overlap elements), (c) a schematic illustration the composite layers around the SiNPs.

The structural change of our composite of PAA-CMC/g-PAN with Si active material was further investigated by X-ray photoelectron spectroscopy (XPS) before and after SHT. The high resolution of the deconvoluted C 1s spectrum of NSi/CMC/PAA, NSi/PAA/CMC/PAN, and NSi/PAA-CMC/g-PAN samples shows in **Figure 5.8a**. For NSi/PAA/CMC sample, the peak at 285.5 eV can be assigned to C–C bond.¹⁵¹ The peak at 286.6 eV relates to the C–O bond while the peak at 289.5 eV can be attributed to C=O bond.^{139, 152} For NSi/PAA/CMC/PAN sample before SHT, the peak at 284.5 eV is related to C–H bond.¹⁵³ Moreover, the peak at 286.8 eV proves the existence of the C–N bond.¹³⁹ For NSi/PAA-CMC/g-PAN sample before SHT, the peak located at

284.8 eV corresponds to the formation of sp^2 ordered carbon (C=C) bond.¹⁵⁴ Clearly, the dramatically increased intensity of C-N bond indicates the successful mixing of NSi/PAA/CMC with PAN.¹⁵⁵ After SHT, the intensity of C=O and C-N bond decreased as well as the intensity of C=C bond increased in XPS pattern, which indicates the successful carbonization of our polymer network.¹⁵⁴ Additionally, as shown in **Figure 5.8c**, the 400 eV binding energy of N 1s representing (C≡N) in the PAN structure¹⁵⁶ disappeared after SHT due to the cyclization of PAN and is replaced by the pyridinic N (398.2 eV) and pyrrolic N (399.6 eV) groups.^{157, 158} The presence of doped N atoms could produce more defects in the graphenized sheets, which can provide efficient pathways for Li-ions and electron transfer leading to dramatic enhancement in the electrochemical performance of the Si-based anode.^{159, 160} In alignment with the above results, Si 2p provide persuasive evidence of the SiO₂ layer after SHT. As shown in **Figure 5.8b**, the peaks centered at 103.2 eV are characteristic of SiO₂. During the mixing process of Si particles with the aqueous PAA/CMC solution, a reaction will occur between the water and the Si surface, which can result in forming more surface oxide on the Si particles. Peaks observed at bonding energies of 99.5 eV for all samples correspond to the bulk Si.¹⁶¹ It shows that the intensity ratio of SiO₂ to Si slightly increased after SHT at 450 °C, indicating the oxidation layer formed on the Si surface during the SHT process.¹⁶²

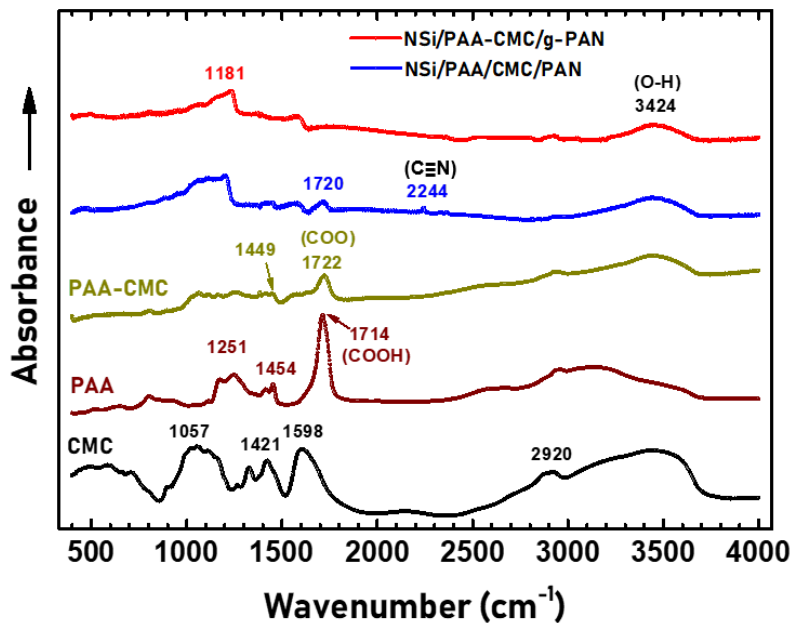


Figure (5.6) FTIR spectra of the composite materials, CMC, PAA, CMC-PAA, NSi/PAA-CMC/PAN, and NSi/PAA-CMC/g-PAN.

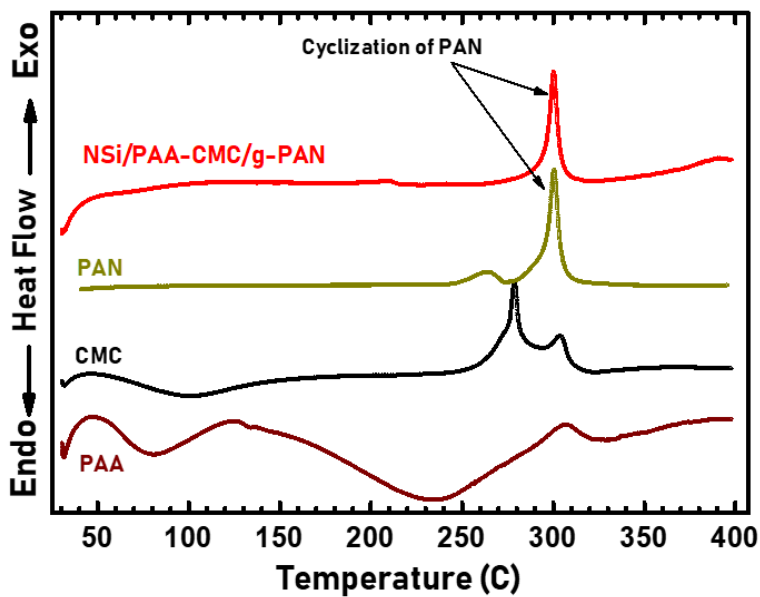


Figure (5.7) DSC analysis of the materials, CMC, PAA, PAN, and NSi/PAA-CMC/g-PAN.

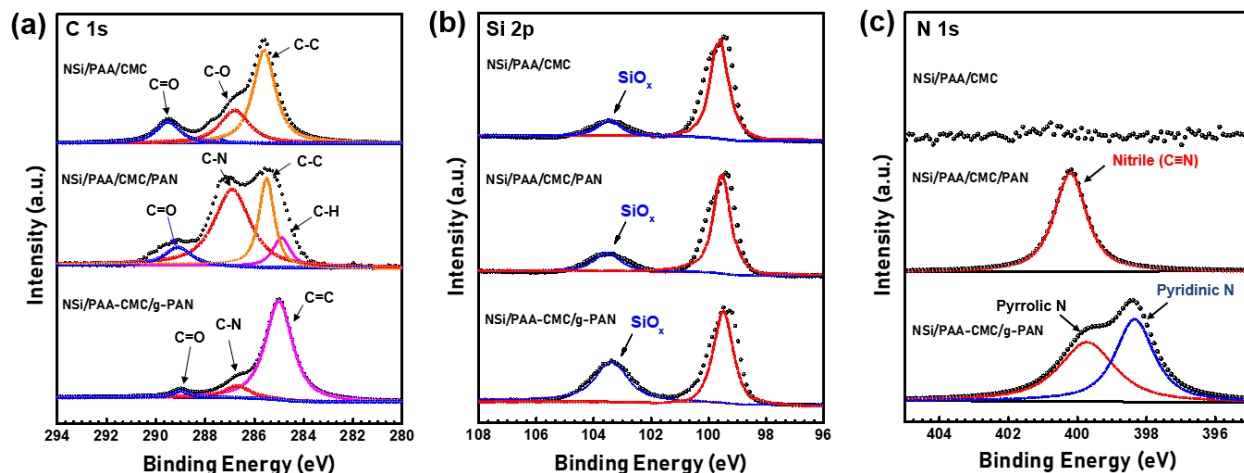


Figure (5.8) High-resolution XPS spectra of the composite materials at different stages: (a) C 1s, (b) Si 2p, and (f) N 1s.

Taken together we have designed a nano-architecting process that played a multifunctional role in the performance of the Si anode. Through the thermal decomposition process of SHT, and due to the abundance of oxygen atoms in water-soluble PAA and CMC polymers, these materials oxidized the Si surface to produce a thin layer of amorphous SiO₂ with a highly porous carbon (PC) layer over the Si surface.^{141, 163} These layer of SiO₂ and PC can work to allow the Li-ions and electrons to pass through. Notably, PAN is rich in nitrogen atoms that have a strong polarity and is considered as the most suitable polymer for LIBs due to its electronegative nitrogen.^{65, 164} During the SHT process, the nature of the chemical structure of PAN changed to form a π -conjugated ring structure by cyclization reaction.⁷⁷ At higher temperatures, the cyclized PAN transformed into a 2D graphenized carbon network with six-membered ring architecture hosting pyridine nitrogen atoms.⁷⁷ The graphenized nanosheets shelled and tethered SiNPs together forming channels through the modified structure network, which lead to the enhancement of the Li-ion diffusion and electron.^{77, 146} Also, this design engineered elastic void spaces for the volume expansion of Si

particles upon lithiation, which will effectively mitigate the aggregation of Si particles, thus reducing the electrode pulverization.¹⁴⁰

Most importantly, to illustrate the electrochemical performance of our Si anode, we tested coin-type half-cells of the Si electrode as the working electrode with a Li foil as the reference and counter electrode using galvanostatic charge/discharge test at room temperature with the potential range of 0.01-1.10 V (versus Li/Li⁺). **Figure 5.9a** displays the galvanostatic charge/discharge performance of the NSi/PAA-CMC/g-PAN nanocomposite at low current rates of 100 and 500 mA g⁻¹. At the first discharge curve, a flat plateau exhibits the alloying process of Li with crystalline silicon.^{136, 165} The subsequent cycles display different behavior due to amorphous Si formed after the first cycle. **Figure 5.9b** exhibits the electrode's specific capacity with Coulombic efficiency versus the cycle number of the coin cell shown in **Figure 5.9a**. This electrode delivers a high initial discharge capacity of 3515 mAh g⁻¹ at 100 mA g⁻¹ with the first cycle efficiency of 80.8%. **Figure 5.10a** shows the rate capability behavior of the NSi/PAA-CMC/g-PAN electrode at different current rates. This electrode shows excellent rate performance with highly stable capacities of 3063.3, 2910.1, 2696.2, 2464.8, 2258, and 2138.7 mAh g⁻¹ at current rates of 100, 1000, 2000, 3000, 4000, and 5000 mA g⁻¹, respectively. It also displays high capacity even under raised current density. More importantly, after discharge and charge at a high current rate of 5000 mA g⁻¹, this electrode can fully return its original capacity of about 2661.2 mAh g⁻¹ at the current rate of 2000 mA g⁻¹, which clearly demonstrates that our design strategy is sturdy enough for electrical and mechanical support. To further evaluate the performance of our design for the Si anode, we investigated its cyclic stability under raised Si loading. In this work, the NSi/PAA-CMC/g-PAN electrode indicates excellent cyclability with a high areal capacity of about 2.7 mAh cm⁻² at 1000 mA g⁻¹ during the battery operation (**Figure 5.10b**). This improvement in cyclability

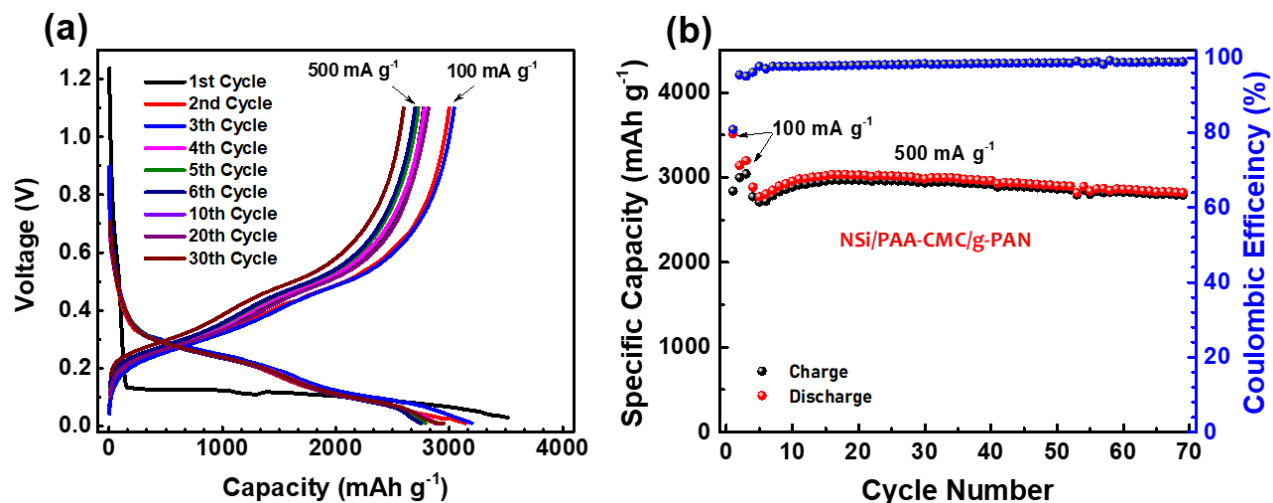


Figure (5.9) (a) Discharge/charge voltage profile of the NSi/PAA-CMC/g-PAN electrode tested at 100 and 500 mA g⁻¹, (b) the corresponding cycling stability of the NSi/PAA-CMC/g-PAN electrode.

for Si anode indicates the significance of the robust 3D structure network of the PAA-CMC and g-PAN polymer. Together with the ease of fabrication, this provides a promising avenue for commercial LIBs.

To fully understand the improved electrochemical performance of our electrode, we investigated the cyclic voltammetry (CV) for the first five cycles (**Figure 5.11a**). At the first cycle, a small cathodic peak appears at 0.44 V, which could be related to the formation of the SEI layer,^{166, 167} which disappears in the second cycle. At the second cycle, the peak appears at 0.2 V corresponding to the transformation from crystalline Si to amorphous phase Li_xSi. During the delithiation process, two peaks at 0.4 and 0.52 V appear, which correspond to the Li extraction process in Si material. All peaks become sharper and stronger with lithiation and delithiation processes due to their activation processes.

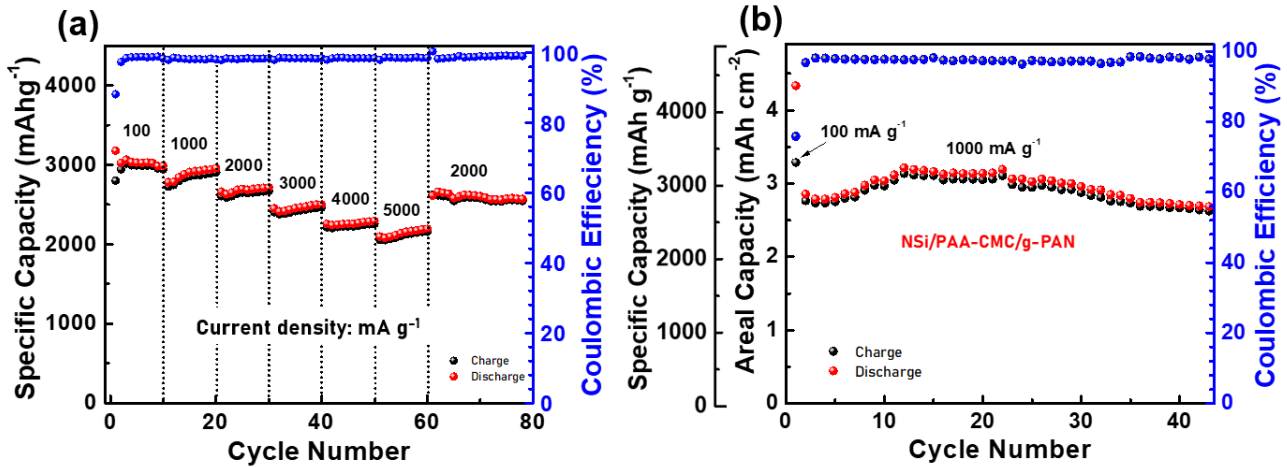


Figure (5.10) (a) Rate capability test of the NSi/PAA-CMC/g-PAN electrode at different current rates, (b) areal capacity for the NSi/PAA-CMC/g-PAN electrode with Si mass loading of 1.2 mg cm⁻².

In addition to the CV, we used the electrochemical impedance spectroscopy (EIS) to investigate the diffusion of Li-ion during lithiation/delithiation processes. **Figure 5.11b** demonstrates the impedance behavior of the three electrodes tested after 50 cycles and after the first cycle for the NSi/PAA-CMC/g-PAN. As estimated from the diameter of the semicircles, the NSi/PAA-CMC/g-PAN electrode has a relatively lower charge transfer resistance than other electrodes, while the NSi/PAA-CMC@450 °C without PAN has a higher charge resistance. This suggests that the conductive NG nanosheets (derived from PAN) accelerated the diffusion of Li ions and shorted Li insertion length during the lithiation and delithiation processes. This strongly supports that the cross-linking of PAA-CMC with the conductive NG has favored the Li-ion diffusion pathway into Si particles.

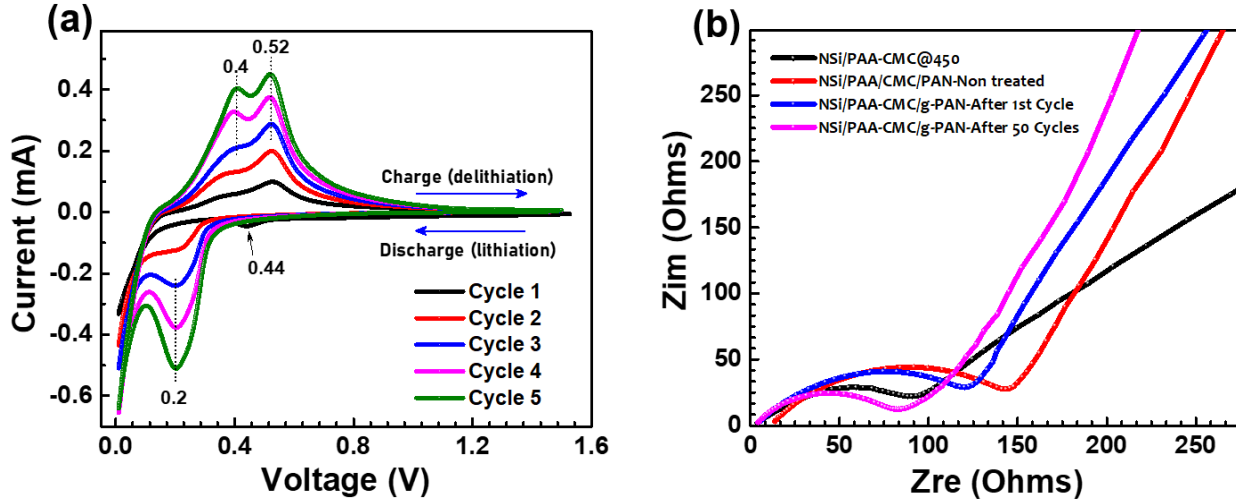


Figure (5.11) (a) Cycling voltammetry curves of a coin-type half-cell of the NSi/PAA-CMC/g-PAN, (b) Nyquist plots of impedance of the NSi/PAA-CMC/g-PAN in comparison with the non-treated NSi/PAA/CMC/PAN and NSi/PAA/CMC treated at 450°C.

Figure 5.12 reveals the long-term cycling stability with Coulombic efficiencies for the electrodes of NSi/PAA-CMC/g-PAN, non treated NSi/PAA/CMC/PAN, and NSi/PVDF/Super P. Obviously, our Si electrode with PAA-CMC and g-PAN displays excellent cycling performance compared with other electrodes due to the synthesis process of our novel architecture design. This electrode demonstrates first high charge and discharge capacities of 3093.9 mAh g⁻¹ of 3472.6 mAh g⁻¹, respectively, with high initial Coulombic efficiency of 89.1%. After two cycles, the Coulombic efficiency reaches to 97% and remains relatively stable at 99.8% in subsequent cycles. We believe this improvement mostly results from the synergy of the combined effect of the heat-treated binders. Also, the enhancement in cycling stability indicates the significance of a stable SEI film, which enhances the cycle life and improves the Coulombic efficiency of the Si-based anode. In comparison, the electrode of NSi/PAA/CMC/PAN without SHT reveals poor cycling performance (green curve, **Figure 5.12**). The discharge capacity quickly decreases after a few cycles, which is mainly associated with the weak adhesion strength of the binder and no conducting

sheets present to enhance the electrical conductivity. This indicates that the SHT process changes the polymers' structure over the Si particles leading to a robust stable structure, which accommodates the irreversible volume change of Si particles during lithiation/delithiation. Moreover, the Si electrode prepared with PVDF and Super P (6:2:2) displays fast capacity decay after several cycles, which may be associated with the plastic deformation of the PVDF binder due to the volume change of Si particles and unstable SEI formation upon cycling.¹³⁹ Other electrodes of NSi/PAA-CMC and NSi/g-PAN were fabricated with the same conditions of SHT to investigate their performance (**Figure 5.13**). Visibly, when the NSi/PAA-CMC electrode was fabricated without PAN and treated at 450 °C, it exhibited slow capacity fading with continuous cycling compared with the NSi/PAA-CMC/g-PAN electrode. This suggests that the composite with PAA-CMC alone is unable to prevent the degradation of Si electrode during repeated cycling and the g-PAN plays a critical role in providing conductive nanosheets that offer diffusion pathways of Li-ions. Also, the graphenized PAN acts both as structural support for mechanical integrity, as well as a conductive agent to improve the overall electrical conductivity of the composite.⁸ In addition, the architecture of the g-PAN allows the SiNPs to effectively utilize the void spaces between the particles within the electrode, which also moderates the volume change of Si particles and maintains a suitable contact with the current collector. When the electrode was fabricated from NSi with PAN and treated at 450 °C, it also showed poorer performance. This result emphasizes that 3D nature of the cross-linking architecture (PAA-CMC) provides a strong binding ability with Si particles, which offers high levels of adhesion and excellent mechanical strength and resistance to degradation.¹⁶⁸ All of these evidence prove that our novel nano-architecture significantly improves the electrochemical performance of the Si-based anode and keep the electrode maintain stable during long cycling.

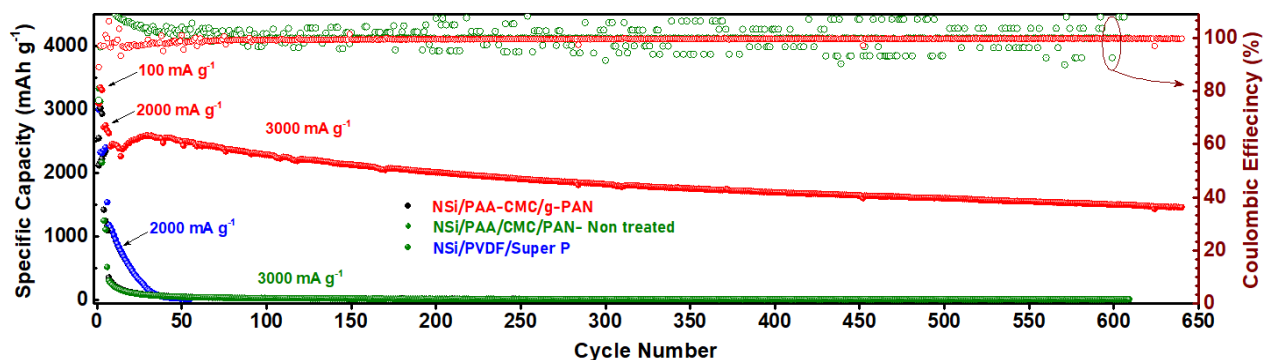


Figure (5.12) Long-term cycling stability for the electrodes of NSi/PAA-CMC/g-PAN, non-treated NSi/PAA/CMC/PAN, and NSi/PVDF/Super P tested at current rates of 100 and 2000 mA g⁻¹ for the first six cycles and 3000 mA g⁻¹ for the subsequent cycles.

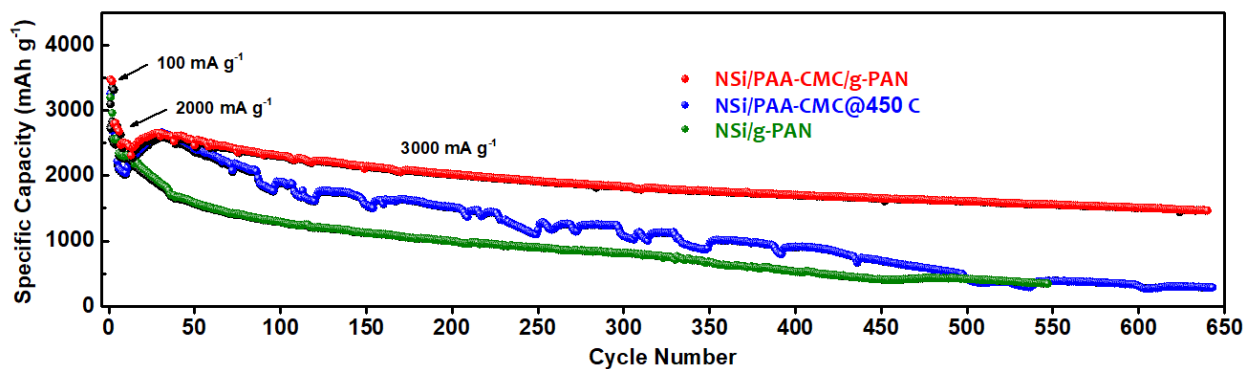


Figure (5.13) Cycling behavior of the reference electrodes compared to our electrode of NSi/PAA-CMC/g-PAN (red color). These electrodes were prepared and subjected to the same conditions of the SHT (450 C) and tested at the same conditions of the current densities (100, 2000, and 3000 mA g⁻¹). The electrode of NSi/PAA-CMC (blue color) was prepared using (60%) of NSi with (40%) of PAA/CMC. The electrode of NSi/g-PAN (green color) was prepared using NSi (60%) with PAN (40%).

After long cycling performance of the Si anode for 650 cycles, the coin cell was opened to investigate the surface morphology change of the composite electrode. **Figure 5.14** displays STEM of the surface electrode with its corresponding EELS mapping for the elements (Si, C, O, and N). The shape morphology of the Si electrode is changed to the amorphous wrinkles-like structure due to the volumetric changes of Si particles caused by the lithiation and delithiation processes, which are expected after long cycling. As a result of repeated cycling, the TEM characterization displays that the Si particles are still enclosed by the SiO₂ layer and wrapped by a framework of nitrogenized carbon nanosheets after carbonization of polymers. This indicates that the durability of this composite encapsulant structure plays a critical role in the high capacity with excellent cycling performance observed for the Si-based electrode. Also, the electrode design of this composite structure with the covalent bonding between the Si and ester group of PAA-CMC prevented the agglomeration of Si particles during long-term cycling. According to the results given above, we can attribute the improved cycling stability with high capacity of our Si electrode to the multifunctional nano-architected system.

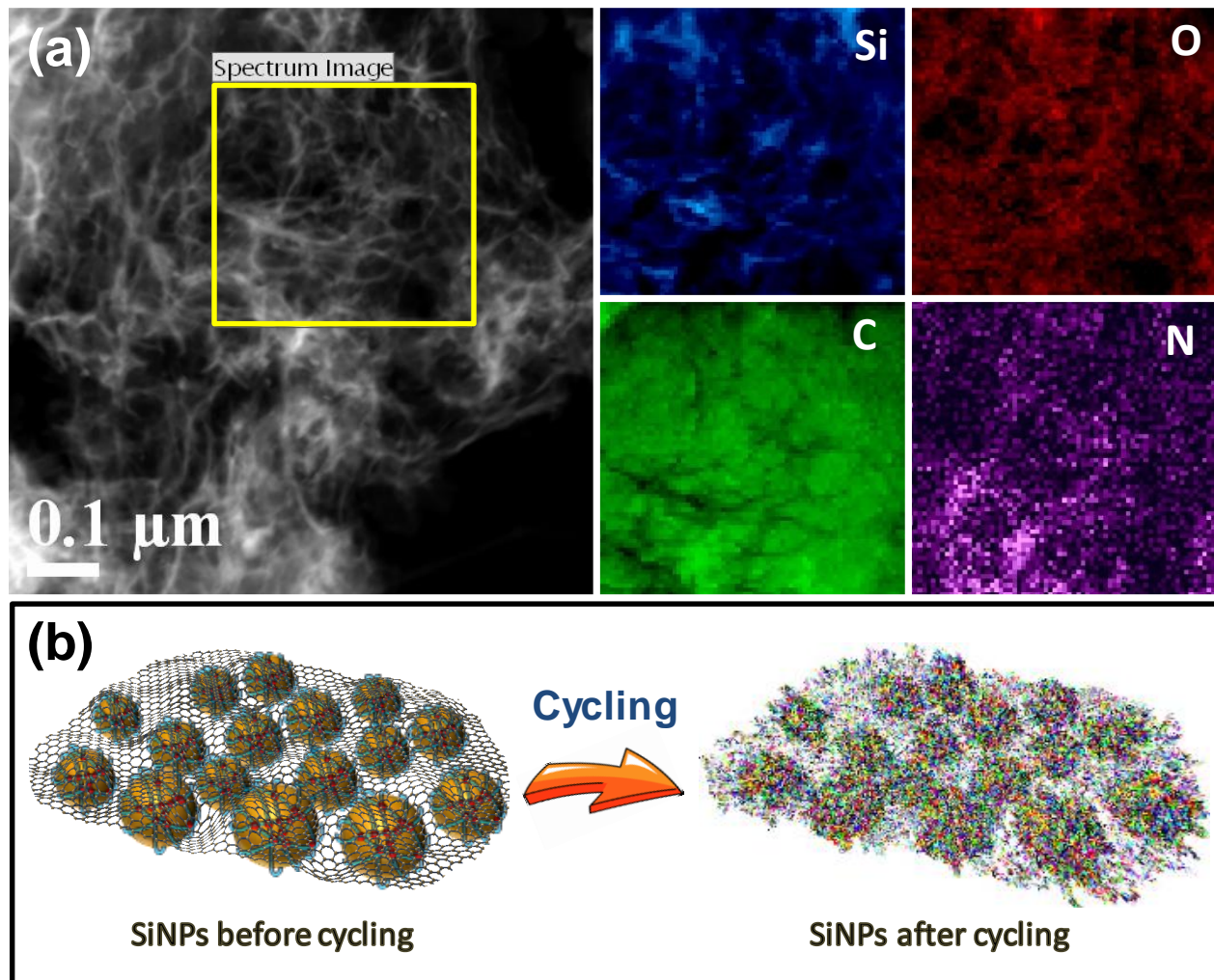


Figure (5.14) (a) HAADF-STEM image of Si electrode surface after 650 cycles with its corresponding EELS mapping of (C, Si, N, and O), and (b) a schematic showing the structure change of Si particles before and after cycling.

In conclusion, we have designed a multifunctional nano-architecture to improve the rate performance of Si-based anode for LIBs. This design was able to serve the role of a Si material while offering enhanced structural and transport properties. We found that by combining our materials PAA-CMC with g-PAN, a robust 3D structure constituting of Si particles with an oxidized shell wrapped with PC and nitrogen graphene sheets is formed. This nanoarchitecture

provides multi-point interactions with the Si, which efficiently limits the severe volume change and prevents the aggregation of Si particles. The intimate contact of Si particle with the conductive network significantly improves the electrical conductivity of the Si anode. Moreover, due to the flexibility and good mechanical properties, the nitrogen graphenized-like nanosheets provide multiple channels for fast ion and electron transportation, which greatly enhances the cycle life. This electrode delivers a high discharge specific capacity of 1563 mAh g⁻¹ after 650 cycles under a high current rate of 3000 mA g⁻¹. This significant performance improvement indicates that constructing the interconnected PAA-CMC and g-PAN structure is an efficient technique to design nanostructured Si-based anode for the next-generation of LIBs and other related energy storage systems.

Chapter 6. Grape Wrapped by Graphene: A New Concept for Smart Anode Design for Anti-aging Lithium-ion Batteries

This chapter is based on an unpublished manuscript by Elhadi Attia et al.

“Grape Wrapped by Graphene: A New Concept for Smart Anode Design for Anti-aging Lithium-ion Batteries”

6.1 Introduction

With the intensification of climate change and the shortage of energy resources, increasing concerns have been raised for the improvement of green renewable energy to replace fossil fuels in recent years. Rechargeable batteries are considered as one of the most promising technologies to enable efficient, clean, and sustainable sources of energy. Lithium-ion batteries are arguably the most currently developed energy storage technologies for different applications such as portobal devices and electric vehicles due to their high gravimetric and volumetric energy densities.^{24, 84, 85} For advanced energy storage systems, long cycle life is one of the key basic requirements. Silicon is a promising candidate material as a negative electrode for next-generation LIBs due to its plentiful availability, relatively low working potential (0.5V vs. Li/Li⁺), and exceptionally high theoretical specific capacity reaching 4200 mAh g⁻¹ compared to the commercial graphite anode.¹³⁻¹⁵ However, the poor cycle retention of Si-based anodes due to the massive volume expansion of Si particles during the alloying reaction with lithium remains to be a major hurdle against commercialization. Specifically, this leads to poor cycling stability, severe capacity loss and dissolution of electrochemical performance resulting in fast pulverization and contact losses of the active material, which is further complicated by the fact that Si is electrically insulative.^{15, 16, 89, 90} Also, the continuous reformation of SEI film on the Si surface leads to short cycle life and largely

irreversible capacities during cycling. These challenges make it hard for Si to meet the increasing demand in various conditions as one of the promising anode materials.¹⁶⁻¹⁹

Several strategies have been investigated to overcome the above issues by engineering the Si composites at the nanoscale.¹⁶⁹⁻¹⁷² Despite these efforts, these composites still suffer from rapid capacity fading. Design of three-dimensional (3D) nanostructure Si-based composites has recently attracted considerable attention to provide excellent electrochemical performance. One of the most promising approaches is the integration of carbon nanotube (CNT) materials with the Si nanoparticles in the electrodes. This approach has received tremendous reports and interest due to their high mechanical properties and superior long-range electrical conductivity at low proportions, which enhanced the capacity and cycling performance of LIBs.^{136, 173-175} However, the poor binding between the CNTs and Si materials during cycling due to the chemical inertness of CNTs, which ultimately results in fading of the electrode capacity.^{176, 177} Modifying nanocomposites by heteroatomic doping has been investigated to be an efficient strategy that improves the performance of Si anode, especially in terms of cyclability. Thus, nitrogen-doped is a key factor, has more attention due to its excellent stability, low cost, and high surface area, which could lead to improve the electrochemical property of the electrode. Moreover, the N-dopant has a higher electronegativity than carbon facilitates permanent dipoles at neutral graphitic surfaces, which can greatly improve the surface energy. Lee et al. found that the N-CNT encapsulated Si particles at room temperature, which can buffer the large volume change and provide excellent stability but still lacking stability of Si-based composite.¹⁷⁸ In addition, involving ladder polymers within the electrode components is a promising strategy, which could minimize the pulverization of Si particles and improve the electrical conductivity of the electrode due to their conjugated structure. Polyacrylonitrile (PAN) is considered a secondary source of nitrogen at a

low cost. Several studies have shown that graphene sheets rich in nitrogen atoms formed by cyclized PAN at low temperature, can provide elasticity and improve the structural stability of the silicon anode.^{77, 145, 149} However, there appears to be a lack of cooperation between the different components added into making Si composite that decrease the overall effectiveness of reported designs.

In this chapter, we developed a novel multi-leveled nanoarchitecture network by combining nano-sized silicon (NSi) active materials, nitrogen-doped multiwalled carbon nanotubes (N-CNTs), and graphenized PAN (g-PAN) to form a high-performance composite anode material through a slow heat treatment process. The SHT was employed to modify the PAN polymer structure within the composite. Therefore, in the NSi@N-CNT composite, the NSi particles were homogeneously deposited on the N-CNT surface by simple mixing with pH control. After incorporating this composite with modified 2D of g-PAN through the SHT, a flexible and self-standing web-like morphology of NSi@N-CNT/g-PAN was further prepared. Through this convenient approach, two forms of nitrogen doping, 1D of N-CNTs and 2D of g-PAN nanosheets, are prepared to provide a 3D architecture that can support the Si structure. The 1D of N-CNTs structure effectively provides channels and highways for electron transport. Furthermore, the 2D nature of g-PAN nanosheets produces a flexible structure network that alleviates the large volume expansion of NSi particles during the lithiation processes as well as builds a stable SEI film. Significantly, with rich N active sites, this network provides conductive transport paths with rich electrochemical activity sites, thus greatly enhancing the conductivity, which shows a remarkably enhanced performance of the Si anode in battery operation. As a result, the NSi@N-CNT/g-PAN composite showed improved reversible capacity and excellent rate capabilities at low and higher Si areal mass loadings.

6.2 Experimental Section

6.2.1 Synthesis of N-doped CNT

In a typical experiment, the nitrogen-doped carbon nanotube (N-CNT) materials have been prepared using urea (Sigma Aldrich) with commercial Multi-Walled Carbon Nanotubes (MWCNT-COOH) with a diameter of about 20 to 40 nm and an average length of 10 to 30 μm (Nanostructured & Amorphous Materials, Inc., Houston, TX) by well grinding. The sample was then subjected to flash heat treatment (FHT) using a quartz tube, which was inserted into a long tube furnace and kept outside the heating zone until the temperature reached 1000 $^{\circ}\text{C}$. Then, the sample moved slowly into the heating zone and remained for about 30 min under Ar atmosphere, followed by slow cooling.

6.2.2 Fabrication and testing of composite electrodes

The electrodes fabrication was achieved by a simple and easy method with low cost of mixing an aqueous dispersion including commercially nanosized Si with an average diameter of 50 to 70 nm with N-CNTs. In order to disperse the N-CNTs uniformly around the Si nanoparticles, 20 mg of a homogenous solution of N-CNTs was firstly achieved by efficient dispersion in deionized distilled water (DDI) of alkaline aqueous solution under stirring and ultrasonic irradiation at room temperature for $\sim 2\text{h}$. Subsequently, 120 mg of Si nanoparticles were added slowly into the mixing solution of N-CNT with controlled pH value of ~ 7.7 under ultrasonication for 60 min then frozen directly in liquid nitrogen to fix the morphology of composites followed by a freeze-drying process for about 72 h. For the working electrode, about 70 wt.% of NSi@N-CNT composite mixed well with 28 wt.% of PAN solution in dimethylformamide (DMF). We added 2 wt.% as a small amount of GO, which was prepared by a modified Hummer's method in order to motivate the cyclization

reaction of PAN during the SHT. To achieve a uniform distribution of the whole composite components, this mixture was mixed under ultrasonic irradiation for about 10 min and a planetary centrifugal mixer (THINKY, AR-100) at a high speed of 10000 rpm for about 10 min followed by alternating magnetic stirring for 10 min at room temperature. The slurry was then cast on the copper foil as a current collector using a doctor-blading and dried for about 1h in a convection oven at 70 °C, then followed by degassed in a vacuum oven at ~ 80 °C for about 10 h to achieve better adhesion of the slurry to the copper foil. Subsequently, the copper foil punched into circular discs of 1.2 cm. Finally, the electrodes were thermally treated at 500 °C in Argon atmosphere for 10 min followed by slow heating. All reference electrodes (NSi@N-CNT, NSi/g-PAN, and N-CNT/g-PAN composites) were prepared through similar procedures.

6.3 Results and Discussion

The synthesis strategy of the NSi@N-CNT/g-PAN composite electrode is schematically demonstrated in **Figure 6.1**. The DDI solution of N-CNTs was firstly ultrasonicated to achieve a high dispersion in a controlling pH of an alkaline aqueous solution. The N-doping helps to produce a homogenous dispersion and enhances the surface charge of CNTs as well as to improve the wettability of the interface between the carbon materials to the electrolyte.¹⁷⁹⁻¹⁸² The NSi particles were slowly added to the mixing N-CNT solution, and this possibly allows for deposition sites of Si particles to the walls of N-CNTs. This could reveal to the electrostatic interactions between the positively charged of N-CNTs and negatively charged of silanol groups (native oxide layer, SiO₂) on the surface of the Si particles.^{178, 183-185} The high-resolution TEM image (**Figure 6.2b**) clearly displays a native oxide layer of SiO₂ with about 3 nm of thickness on the Si particle surface.

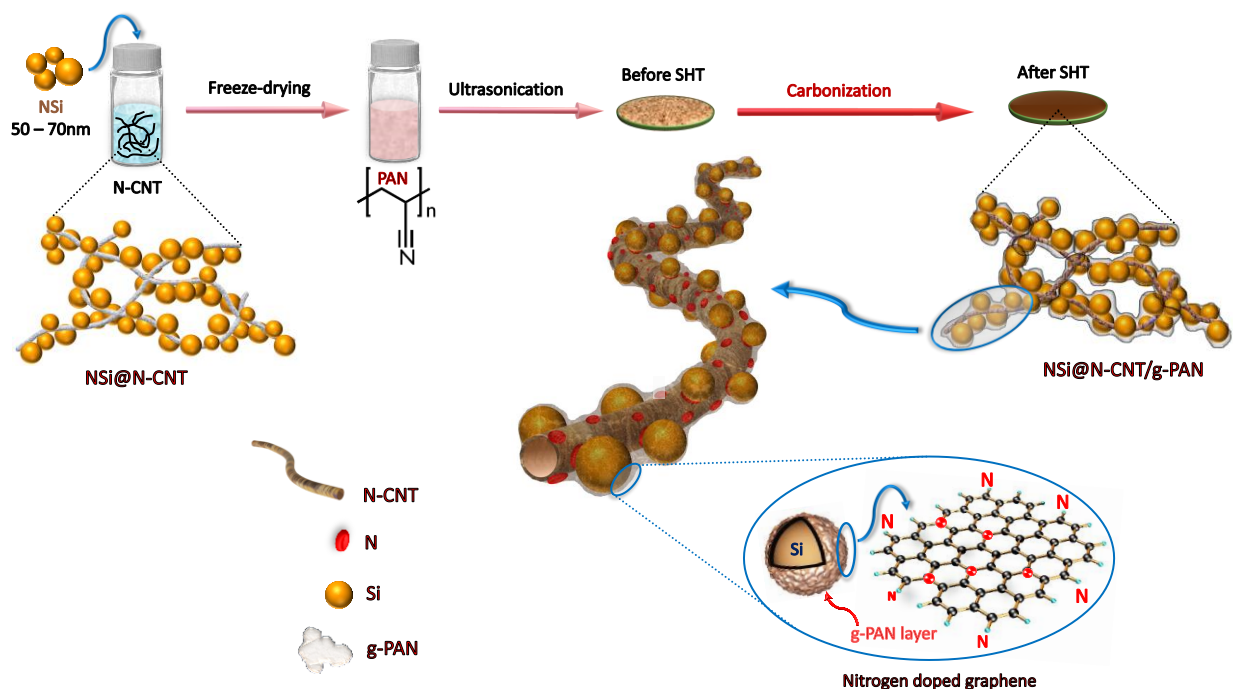


Figure (6.1) A schematic illustration of the design procedure of the NSi@N-CNT/g-PAN composite.

In addition, XPS for pure Si materials (**Figure 6.2c**) shows two peaks, which corresponding to Si and SiO₂. This oxide layer plays a significant role in the electrostatic bonding with the graphitic materials due to its negative surface charge.^{186, 187} These negative surface charges can attract the counterparts with positive surface charges which can participate in electrostatic attraction. In addition to the interaction between Si nanoparticles and N-CNTs, a flexible conductive framework is employed as encapsulation to prevent electrical contact loss during volume expansion. A graphenized PAN as a carbon and nitrogen source provides elasticity to form an electric conductive skeleton of this composite during the slow-heat treatment protocol. During the SHT, the chemistry and structure of the original PAN changed and converted to a conjugated network structure *via* a cyclization reaction, which provided a 2D elastic nanostructure of g-PAN wrapped the surface of

NSi@N-CNT as well as improve the adhesion of the Si particles to the N-CNT structure. This conjugated network forms a conductive network, which could accommodate the volume expansion of Si particles and facilitates the fast transfer of electrons during lithiation and delithiation as well as maintains the structural stability of the electrode, thus enhanced the long-term cycling stability.

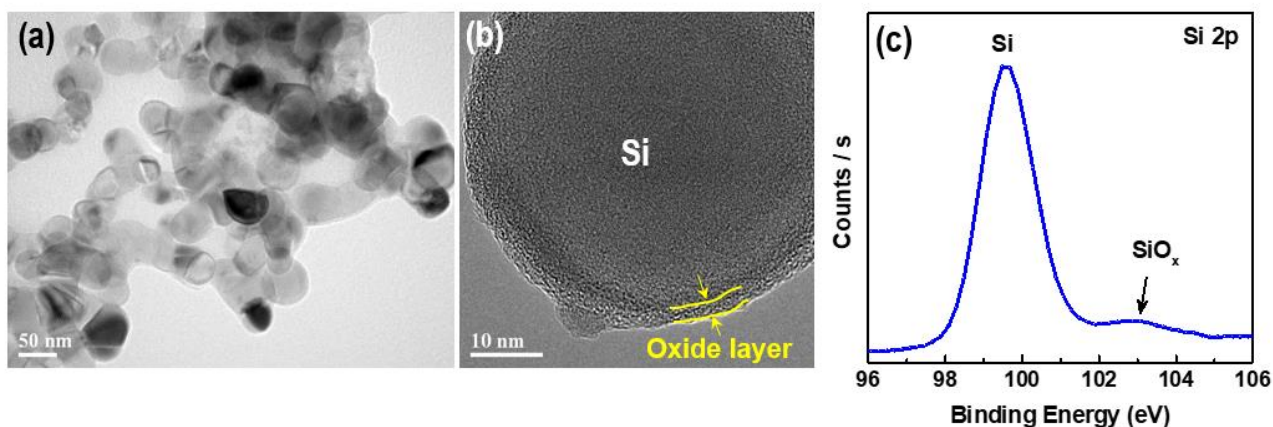


Figure (6.2) (a) TEM image of few Si particles shows the average diameter of about 50 to 70 nm, (b) HRTEM image of the crystalline Si particle shows the oxide layer (b) XPS of Si 2p of pure Si shows the SiO_x peak.

Figure 6.3a shows the morphology of the prepared N-CNTs materials characterized by SEM. As shown in **Figure 6.3b**, the low-resolution TEM result demonstrates that the N-CNTs with a diameter range from 20 to 40 nm. In addition, the N-CNTs were mapped by energy dispersive spectroscopy (EDS) to prove the presence of C, N, and O as shown in **Figure 6.4**. Moreover, the SEM image in **Figure 6.3c** shows the morphology of NSi@N-CNT after freeze-drying process, which suggests that the Si particles are homogeneously distributed and connected to walls of N-CNTs, preserving the electrode structure as a robust matrix. Furthermore, the Si particles appear

to be physically adhered to the N-CNT, as shown in TEM image (**Figure 6.3d**), which can act as electron highways. Since the surface of Si particles has a thin layer of SiO₂, the surface is negatively charged, which can bound with N-CNTs by electrostatic attraction.¹⁸³ After the SHT, the NSi@N-CNT is encapsulated by homogeneous nanosheets of g-PAN forms web-like morphology of 3D flexible structure (as seen in the HR-SEM studies, **Figure 6.3e**). This network interlaces the NSi particles inside the structure and binds them to the N-CNTs, which is expected to not only prevent Si degradation during repeated cycling but also could provide a high elasticity of the whole structure and further improve the electrical conductivity. For further support, the TEM characterization (**Figure 6.3f**) clearly shows that the NSi@N-CNT composite is well-wrapped and by nanosheets matrix forming a multi-layered g-PAN. The graphene layer over the Si particle could limit direct contact with the electrolyte, which would limit side reaction. Moreover, EDS elemental mapping of the NSi@N-CNT/g-PAN electrode displays the homogeneous dispersion of carbon, nitrogen, and oxygen elements within the composite as shown in **Figure 6.5**. This indicates that the Si nanoparticles are homogeneously distributed with these elements in the electrode. In addition, our composite network inherited good flexibility caused by graphenized PAN and N-CNTs, which could be mechanically bended without breaking (**Figure 6.6**).

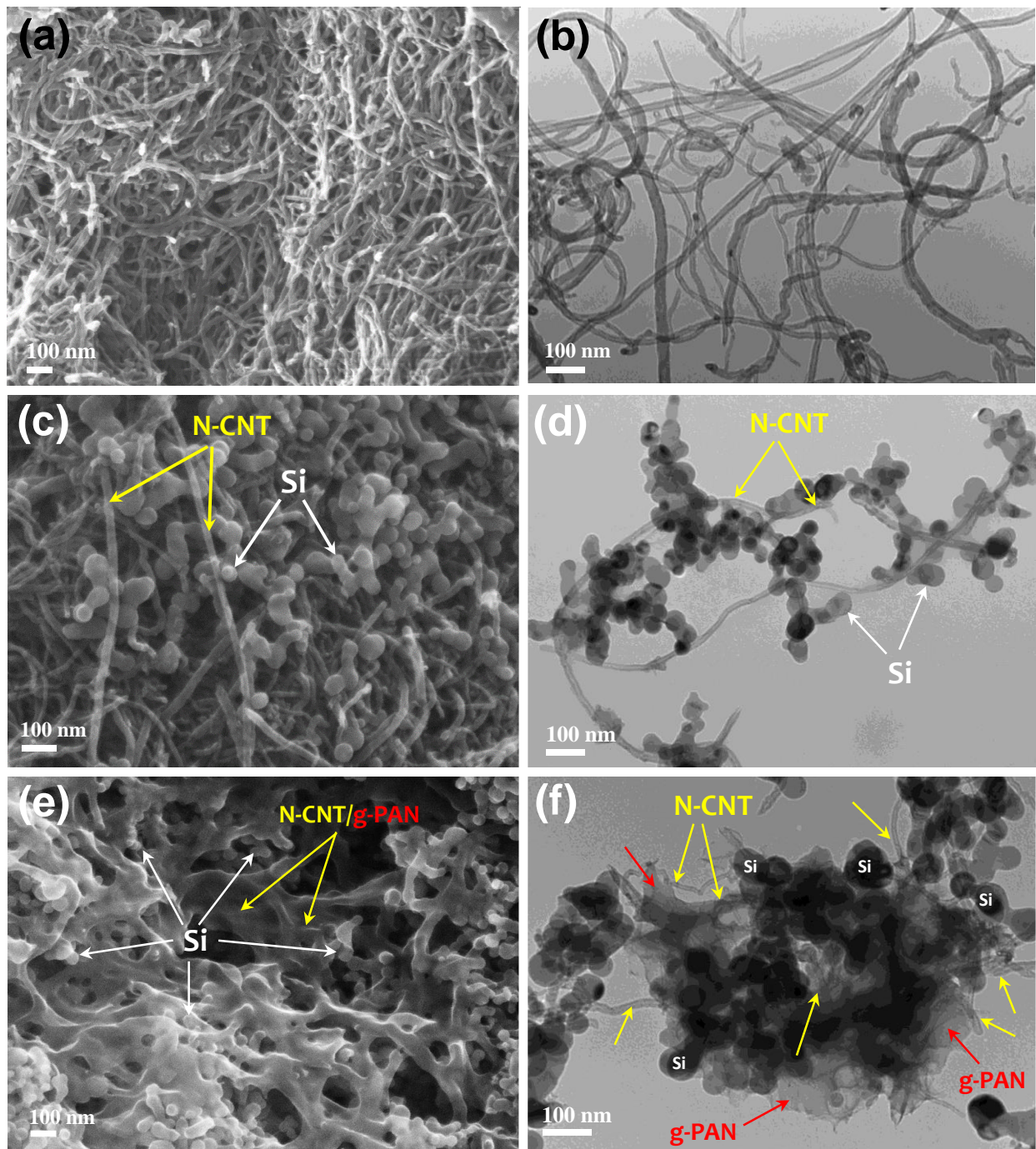


Figure (6.3) (a) HR-SEM image of NSi@N-CNT shows Si particles connected to the N-CNTs, (b) TEM image of NSi@N-CNT shows the Si particles connected to the N-CNTs, (c) HR-SEM image shows g-PAN covered the NSi@N-CNT network, and (d) TEM image of NSi@N-CNT/g-PAN nanocomposite shows the g-PAN covered the NSi@N-CNT.

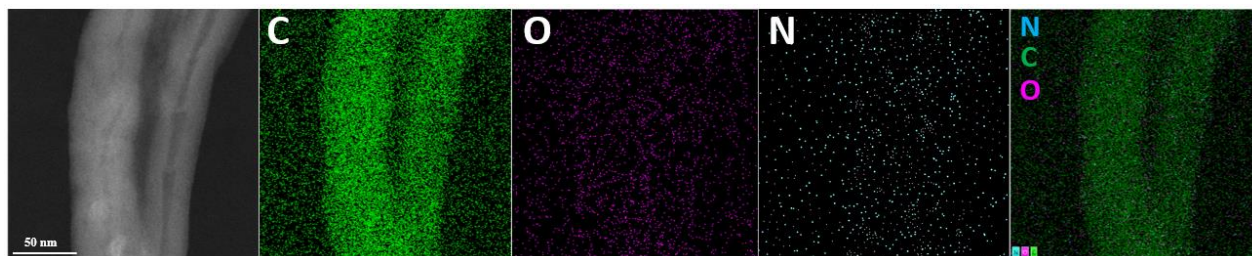


Figure (6.4) (a) TEM image of N-CNT with its corresponding EDX elemental mapping for (C, O, N and overlap elements).

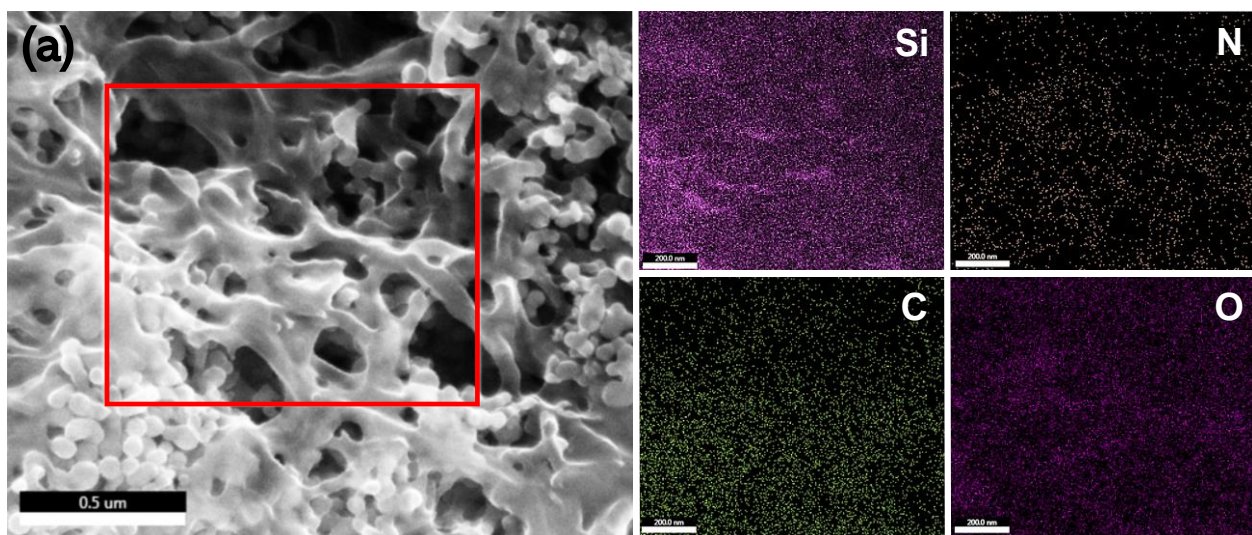


Figure (6.5) (a) HR-SEM image of NSi@N-CNT/g-PAN electrode with its corresponding EDS mapping of Si, N, C, and O.

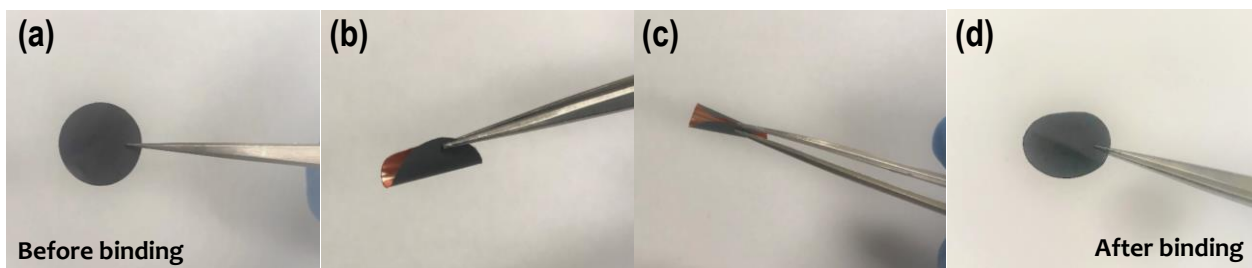


Figure (6.6) Digital photos of the NSi@N-CNT/g-PAN electrode before and after bending showing keep adhered with no detachments.

In order to obtain further information about the composition of our material, XRD and Raman spectroscopy were conducted. **Figure 6.7** displays the XRD patterns of g-PAN, N-CNT, and NSi@N-CNT with the pattern of NSi@N-CNT/g-PAN composite. The observed peaks at 28.7, 47.6, 56.4, 69.4, and 76.7° in the pattern of NSi@N-CNT/g-PAN composite corresponding to the (111), (220), (311), (400), and (331) plane of crystalline Si, respectively. Two broad graphitic peaks are observed at ~ 26° and weak peaks at ~ 43° for both g-PAN and N-CNT, which corresponding to the crystal planes of (002) and (101), respectively.¹⁸⁸ Especially, these peaks together with the ones from the g-PAN and N-CNT are still observed in the pattern of the NSi@N-CNT/g-PAN composite, which indicates that there is no intrinsic change to the nature of each composite component and the material is indeed a composite that is cleverly blended. To identify the graphitic level and structural changes of the composite, Raman spectroscopy was investigated (**Figure 6.8**). The N-CNT shows two peaks located at 1345 and 1580 cm⁻¹, which are related to D and G bands, respectively (I_D/I_G ratio of 0.82). These peaks were observed in the NSi@N-CNT electrode with a slight shift to 1347 cm⁻¹ for D band and 1597 cm⁻¹ for G band as shown in **Figure 6.9a**, which could be related to the electrostatic attractions between Si and N-doped sites at CNT. In addition, g-PAN observes two peaks of D-band at 1370 and G-band at 1587 cm⁻¹ with a higher I_D/I_G ratio of 3.62, which is higher than that of N-CNTs. This indicating a higher degree of defects in g-PAN, which could be result from the higher nitrogen content. Obviously, the intensity of D-band in g-PAN is higher than G-band, which indicates that there are a higher number of defects sites and disorder sp³ carbon atoms.^{77, 145} The higher intensity of the D-band peak is resulting from the original carbon defects from sp³-carbon atoms in a two-dimensional lattice of g-PAN and the N-CNT walls, while the G-band peak is reflecting the plane vibration of sp²-carbon atoms.^{77, 189} As expected, a similar Raman spectrum was observed in our electrode of NSi@N-CNT/g-PAN

with more intense of D-band, which confirmed the increasing the number of defects in the electrode structure. Also, this composite has a higher I_D/I_G ratio of 2.72, which could be due to the higher nitrogen content compared to NSi@N-CNT composite. In addition, the NSi@N-CNT/g-PAN shows that D-band shifted to lower wavenumber (1355 cm^{-1}), while G-band shifted to 1575 cm^{-1} (**Figure 6.9a**), which possibly due to the change in the electronic structure of the electrode caused by the higher nitrogen content.¹⁹⁰ These results are in good alignment with the EDS mapping. Besides the D and G bands, a sharp characteristic peak was observed at around 512 cm^{-1} related to crystalline Si. This peak is slightly shifted to lower wavenumbers of NSi@N-CNT/g-PAN composite (509 cm^{-1}) with low intensity as shown in **Figure 6.9b**. This downshift is generally associated with surface stresses on the surface of Si particles which could result in an entire wrapping of Si particles by the graphene sheets,^{191, 192} confirming the success of our composite design.

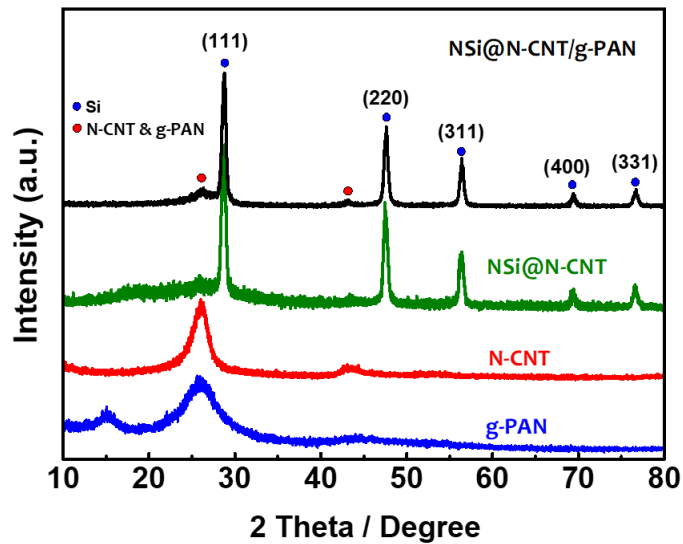


Figure (6.7) XRD patterns of g-PAN, N-CNT, NSi@N-CNT, and NSi@N-CNT/g-PAN nanocomposite.

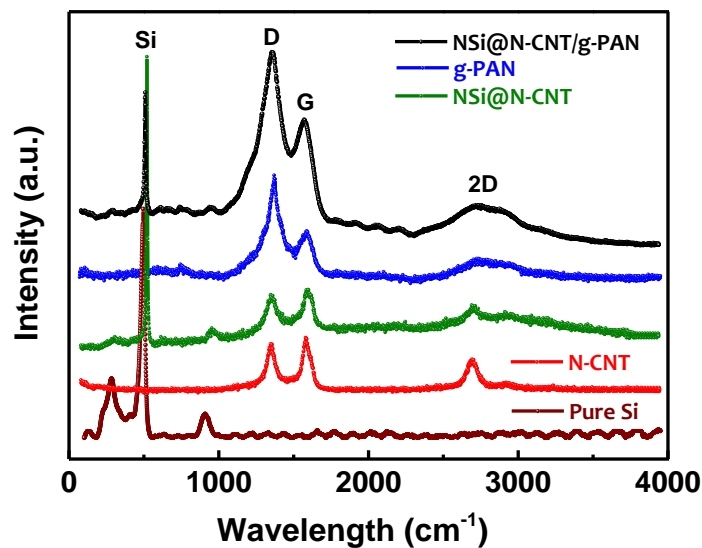


Figure (6.8) Raman spectrum of pure Si, N-CNT, NSi@N-CNT, g-PAN, and NSi@N-CNT/g-PAN nanocomposite.

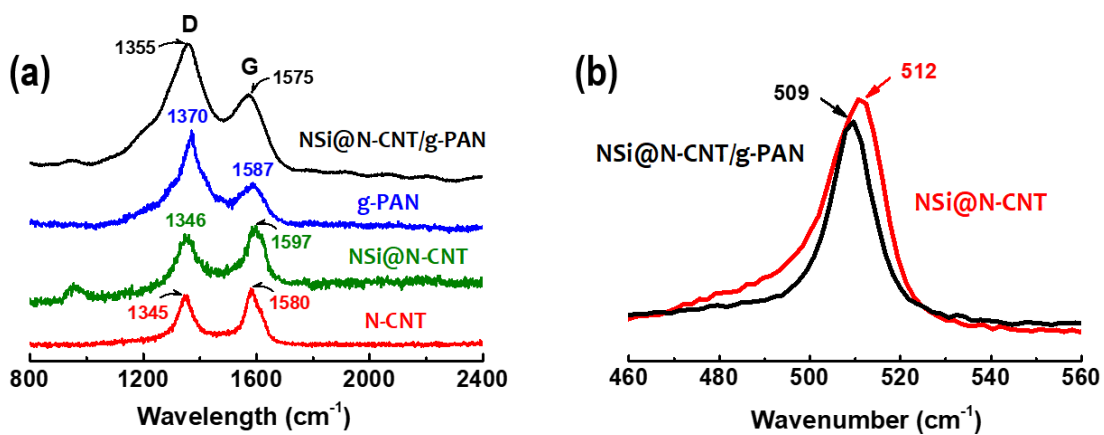


Figure (6.9) (a) Raman spectra of D and G bands of N-CNT, g-PAN, NSi@N-CNT and NSi@N-CNT/g-PAN with their relative shifts and (b) Raman spectra Si peak of NSi@N-CNT and NSi@N-CNT/g-PAN composites shows the shift of Si peak.

Further identification of the elemental composition and surface properties of the electrode were obtained using XPS. Based on the XPS survey spectra in **Figure 6.10**, the NSi@N-CNT/g-PAN composite has higher nitrogen content compared to NSi@N-CNT as were expected, while no nitrogen peak appears in the CNT as shown in **Figure S6.1, Appendix A**. In addition, the high-resolution N 1s XPS spectra of N-CNT (**Figure 6.11a**) shows three peaks at 398.48, 399.78, and 401.28 eV, which are attributed to pyridinic-N, pyrrolic-N, and graphitic-N, respectively.¹⁷⁸ These peaks confirm that the doping of nitrogen atoms doped at the edge of graphite planes of CNTs. The presence of pyridinic-N structure in N-CNTs is attributed to a nitrogen atom that bonded to two adjacent carbon atoms, while the pyrrolic-N structure attributed to that nitrogen atoms that are bonded to two carbon atoms and contribute to the π system with two π -electrons.¹⁹³ Therefore, the nitrogen atoms partially replace a part of carbon atoms in the graphitic side wall of CNTs, which provide more active sites for binding with Si.¹⁹⁴ Moreover, the electron-rich N could enhance the surface energy of the CNTs as well as the conductivity.¹⁹⁵ Same peaks also observed in the N-CNT/g-PAN composite with an additional peak at 404.88 eV which can be related to oxidized-N formed in presence of oxygen during the SHT.^{196, 197} Interestingly, when g-PAN is added to the N-CNTs, the nitrogen content is increased to 13.79% as shown in **Table 6.1**. In addition, the peaks of pyridinic-N slightly shifted to 398.39 eV and pyrrolic-N to 400.1 eV in the N-CNT/g-PAN composite with a higher intensity of pyridinic-N due to the higher nitrogen content, which caused by N-rich graphene formed by g-PAN.^{158, 198, 199} All of these peaks together are still observed in the pattern of the NSi@N-CNT/g-PAN composite, with a slight shift of pyridinic-N to 398.58 eV and pyrrolic-N to 399.98 eV as shown in **Figure 6.11a**. In addition to these peaks, the NSi@N-CNT/g-PAN composite shows a peak centered at 397.88 eV which corresponds to Si-N bond.^{200, 201} The appearance of this bond related to that nitrogen has a higher electronegativity than carbon

which proves the exists of an intimate contact between the N-CNTs with Si particles. More interesting, the oxidized peak shifted to higher binding energy of 405.6 eV, which could result from the oxygenated Si. The relative amount of the N species in the NSi@N-CNT/g-PAN composite is 50.3% for pyridinic-N and 14.3% for pyrrolic-N, which is consistent with the above Raman results. The presence of pyridinic-N atoms was believed to provide an effective electron transfer. This would be beneficial for improving the reversible capacity of the composite through interaction with Si. This evidence is strongly supported the successful incorporation of nitrogen on the g-PAN in the electrode by the cyclization reaction and converted the triple bond structure of the nitrile groups ($C\equiv N$) to double bond structure ($C=N$) in the PAN structure during the SHT (**Figure 6.11b**). The onset temperature for the cyclization reaction was proved using DSC (**Figure S6.2, Appendix A**), which shows a sharp exothermic peak of pure PAN at 300 °C and the initial weight loss of TGA results of pure PAN at the same temperature (**Figure S6.3, Appendix A**). Therefore, during the slow heating protocol, the chemistry of PAN structure has changed from aliphatic linear to 2D structure analogical of graphenized PAN, which is related to the changes in the type of the chemical binding of nitrogen with six-membered cyclic of pyridinic N-rich aromatic ladder structure.^{77, 202, 203} This structure provides an architecture of nitrogen-doped graphene nanosheets, which can compensate the low electrical conductivity of the Si electrode and maintain the stabilization of the whole composite structure thereby contribute to improve the reversible capacity.^{77, 150} These results are supported by previous reports that investigated how PAN undergoes a structural transition to form a thermally stable conjugated ladder structure of NG, acting as both a binder and conductive support for Si electrode.^{145, 204} The high-resolution XPS scan for C 1s shows several peaks in **Figure 6.11c**. The two peaks located at 284.4 and 285.2 eV indicate the presence of sp^2 hybridized graphitic type carbon ($C=C$) and sp^3 bonded carbon ($C-C$),

respectively.^{77, 108} The peak located at 286.5 eV is associated with the carbon atoms bonded to the nitrogen atoms in C-N bond, which likely stems from the edge-nitrogen atoms on the edge of the g-PAN and N-CNTs.^{114, 205} While the peak located at 289.6 eV is attributed to O=C-O group.¹¹⁶ The XPS spectra of Si 2p (**Figure 6.11d**) shows a sharp peak at 99.68 eV corresponds to Si-Si bond, with a minor peak observed at 101.2 eV could be related to the Si-N bond.^{200, 206} At higher binding energies, peaks centered at 102.7 could correspond to Si-N-O and 103.4 eV related to oxygenated Si.^{206, 207} The decomposition temperature and weight loss of the composite materials, thermogravimetric analysis (TGA) were performed for N-CNTs, pure PAN, and NSi@N-CNT/g-PAN composite (**Figure S6.3, Appendix A**). The TGA of pure PAN confirms a two steps of mass loss at about 300 and 470 °C, which corresponding to the cyclization and the graphenization processes.¹⁸⁶ While the N-CNTs remain stable during the heating up to 550 °C, after which they begin losing gradually.

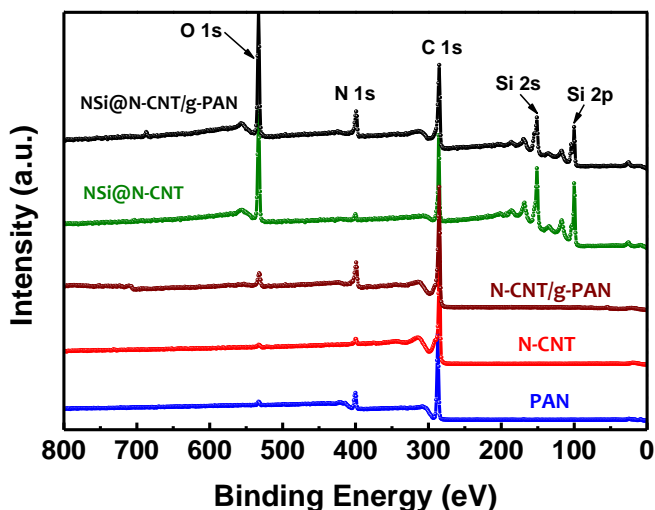


Figure (6.10) XPS spectrum of the PAN, N-CNT, N-CNT/g-PAN, NSi@N-CNT, and NSi@N-CNT/g-PAN nanocomposite.

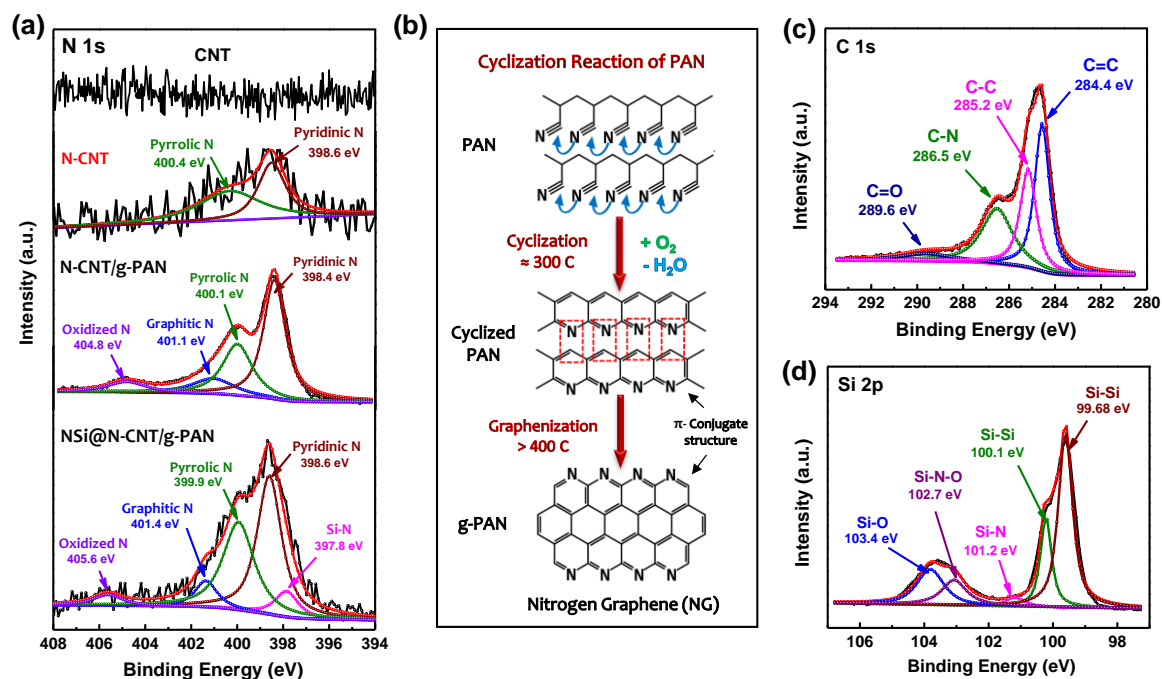


Figure (6.11) (a) The high-resolution XPS of N 1s of CNT, N-CNT, N-CNT/g-PAN, and NSi@N-CNT/g-PAN nanocomposite, (b) cyclization reaction of PAN, (c) XPS of C 1s of NSi@N-CNT/g-PAN nanocomposite, and (d) XPS spectrum of Si 2p of NSi@N-CNT/g-PAN nanocomposite.

Table (6.1) Elemental compositions of N-CNT/g-PAN composite from XPS analysis.

Name	Peak BE	Area (N)	Atomic %
C1s	284.78	1310.85	80.8
N1s	398.49	223.79	13.79
O1s	531.83	87.65	5.4

To investigate the electrochemical performance of the NSi@N-CNT/g-PAN composite, a coin-type half-cell system of Si composite as a working electrode with a lithium foil was used as reference and counter electrodes using galvanostatic lithiation/delithiation over the voltage range of 0.01-1.10 V versus Li/Li⁺. **Figure 6.12** shows the galvanostatic discharge/charge profile of the NSi@N-CNT/g-PAN composite anode measured at a low current density of 500 mA g⁻¹ for about 50 cycles. As shown, a flat plateau is observed at the first discharge curve due to the alloying process of crystalline Si with lithium ion.^{136, 165} The subsequent cycles exhibit various behavior, indicating a transformation from crystalline Si to amorphous Si formed after the first cycle.^{122, 208} This composite anode exhibits discharge and charge capacities of approximately 3511 and 2967 mAh g⁻¹, respectively, with an initial Coulombic efficiency of 84.5%, indicating a stable SEI formation. **Figure 6.12b** shows the capacity behavior of this composite anode measured at a low current density of 500 mA g⁻¹. Apparently, this composite delivers an excellent cyclability with an average capacity of ~ 2950 mAh g⁻¹ (~ 3 mAh cm⁻² of areal capacity) up to 50 cycles. This enhancement in cycling stability refers to the sturdy structure of our design with the conductive network of N-doping in CNT and g-PAN. To investigate the role of g-PAN in the electrochemical performance of our composite, we compared the rate capability performance of the NSi@N-CNT/g-PAN composite electrode against the NSi@N-CNT electrode (without g-PAN) was compared (**Figure 6.13**). Both electrodes were cycled at various current densities starting from 100 mA g⁻¹ for the first cycles, then the current densities were increased stepwise to 6000 mA g⁻¹ for more than 60 cycles. With the increased current densities, NSi@N-CNT/g-PAN electrode shows an excellent rate performance with high stable capacities of 3560.5, 2825.6, 2228.6, 1814.1, 1685.9, 1551.8, and 1216.6 mAh g⁻¹ at current densities of 100, 1000, 2000, 3000, 4000, 5000, and 6000 mA g⁻¹, respectively. More important, this composite exhibit highly reversible capacity even

under a high current density of 6000 mA g^{-1} and able to revert the reversible capacity to $2189.2 \text{ mAh g}^{-1}$ after the current density was returned to 2000 mA g^{-1} , which is very close to the above original capacity of $2228.6 \text{ mAh g}^{-1}$. In contrast, the NSi@N-CNT cannot resume its original capacity at 2000 mA g^{-1} of current density after testing at a high current density of 6000 mA g^{-1} .

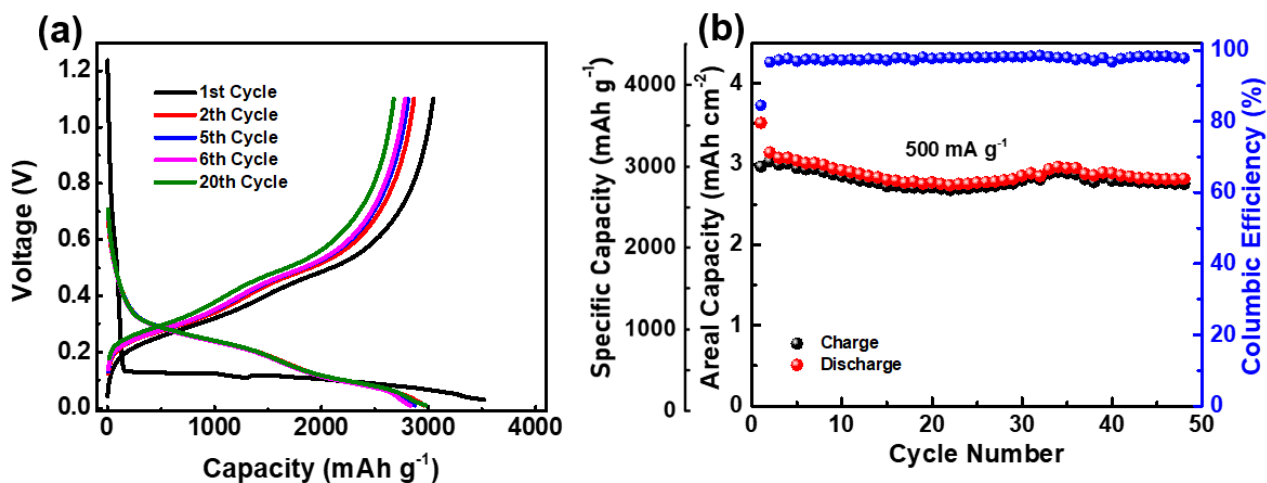


Figure (6.12) (a) Discharge/charge profile of the NSi@N-CNT/g-PAN nanocomposite tested at low current rate of 500 mA g^{-1} , (b) Cycling stability and the areal capacity of the NSi@N-CNT/g-PAN composite in (a).

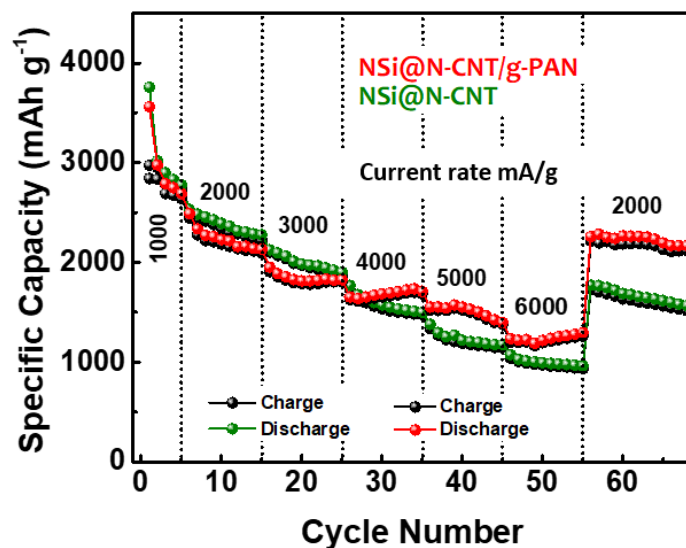


Figure (6.13) Rate capability of NSi@N-CNT and NSi@N-CNT/g-PAN tested at different current rates (100 to 6000 mA g⁻¹).

Furthermore, we compared the long-term cycling stability of the NSi@N-CNT/g-PAN electrode with NSi@N-CNT and NSi/g-PAN electrodes, which was tested at current densities of 100, 2000, and 3000 mA g⁻¹ as shown in **Figure 6.14**. Apparently, the NSi@N-CNT electrode displays poor cycling performance after delivering a high initial capacity of 3148 mAh g⁻¹. The capacity drops quickly to ~ 2000 and ~ 280 mAh g⁻¹ after the second cycle and 450 cycles, respectively. It seems that the N-CNTs alone are not sufficient for the stabilization of the electrode. Also, the capacity fading can be attributed to the degradation of the Si structure due to the volume expansion of Si particles during cycling leads to the separation from the N-CNT network. Similarly, the performance of the NSi/g-PAN (N-CNT-free) composite anode also did not perform as well. This result emphasizes the critical role of the bonding between the N-CNT and Si particles. In contrast, the NSi@N-CNT/g-PAN composite anode significantly delivers much better cycling

stability where a reversible capacity of $\sim 1370 \text{ mAh g}^{-1}$ can be maintained after 1100 cycles at a high current density of 3000 mA g^{-1} . Significantly, this electrode delivers a high initial Coulombic efficiency of 85.2% at the first cycle, which increased and remained stable at $\sim 99.8\%$ for the subsequent cycles. Overall, these electrochemical results suggest that when both N-CNT and g-PAN are incorporated in the anode, the performance observed a significant boost. The impressively enhanced performance of NSi@N-CNT/g-PAN composite can be attributed to the specific roles of each composite component and the following reasons. First, the stable electrostatic interaction between the N-CNTs and the surface of Si particles contributes the enhanced rate performance. Second, the g-PAN offers a 2D highly conductive flexible network of N-rich graphene framework, which host the Si particles and accommodate the volume expansion of Si particles during repeating cycling as well as build stable of SEI layer. Third, the flexible network of N-CNT provides electrochemically stable structure as electrically conductive highways for electron transport, facilitating high electrode capacity at a large charge and discharge current. Finally, the higher pyridinic nitrogen content in the composite was showed to have a critical impact in improving the direct electron transport leading to enhance overall electrical conductivity. **Figure 5.16** shows a comparison for the composite before and after SHT. As shown, the electrode before SHT provided poor performance compared to the electrode after SHT.

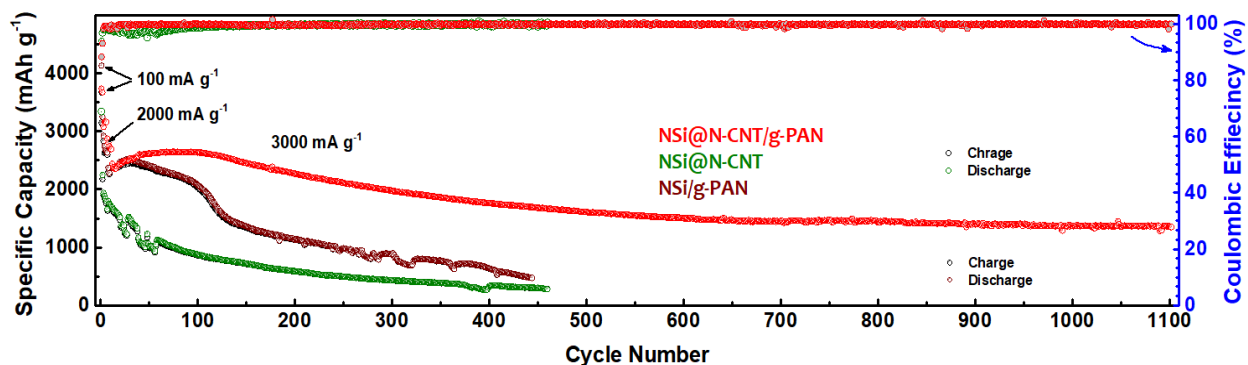


Figure (6.14) Long-term cycling stability of NSi@N-CNT, NSi/g-PAN, and NSi@N-CNT/g-PAN composites tested at current rates of 100 and 2000 mA g^{-1} for the first ten cycles followed by 3000 mA g^{-1} for the subsequent cycles.

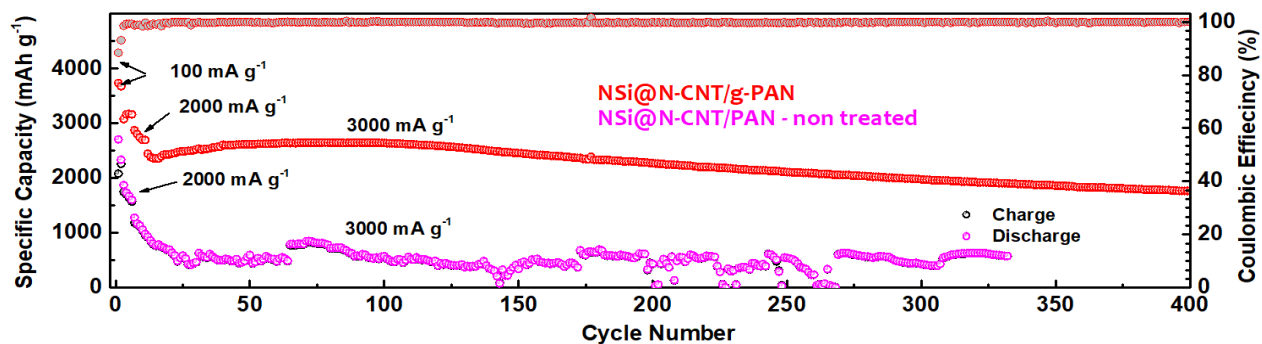


Figure (6.15) Cycling performance of our NSi@N-CNT/g-PAN electrode (red color) compared with the electrode of NSi@N-CNT/g-PAN electrode without SHT.

Additionally, the incorporation of nitrogen doping could be the major cause in the enhancement of the reversible capacity of the electrode. These contributions of N-doping interacting with Si facilitate stabilization of the NSi@N-CNT/g-PAN electrode, which clearly indicates that our design strategy of 3D multi-leveled nanoarchitecture is sturdy enough for electrical and mechanical support. Moreover, to investigate the role of both N-CNTs and g-PAN, reference electrodes were fabricated using N-CNT with g-PAN (60:40) under the same conditions and tested at different current densities as shown in **Figure 6.16**. As shown in **Figure 6.16a** and **b**, the N-CNT/g-PAN electrode tested at a low current density of 100 mA g^{-1} provides excellent cycling performance with an average reversible capacity of 430 mAh g^{-1} for about 400 cycles. In addition, the N-CNT/g-PAN electrode is shown in **Figure 6.16c** and **d** is tested at 100, 2000 mA g^{-1} then followed by a high current density of 3000 mA g^{-1} . This electrode reveals stable cyclability for more than 1000 cycles with an average reversible capacity of 378 mAh g^{-1} as shown in **Figure 6.16d**. These results indicate the important role of the corporation of both N-CNT and g-PAN in the design of the robust structure of our composite which reflects in the improved electrode stability and long cycle life. These results also confirm that the majority of the reversible capacity in the Si composite anodes stems from the Si material and that N-CNT and g-PAN mostly serve the role of structural support.

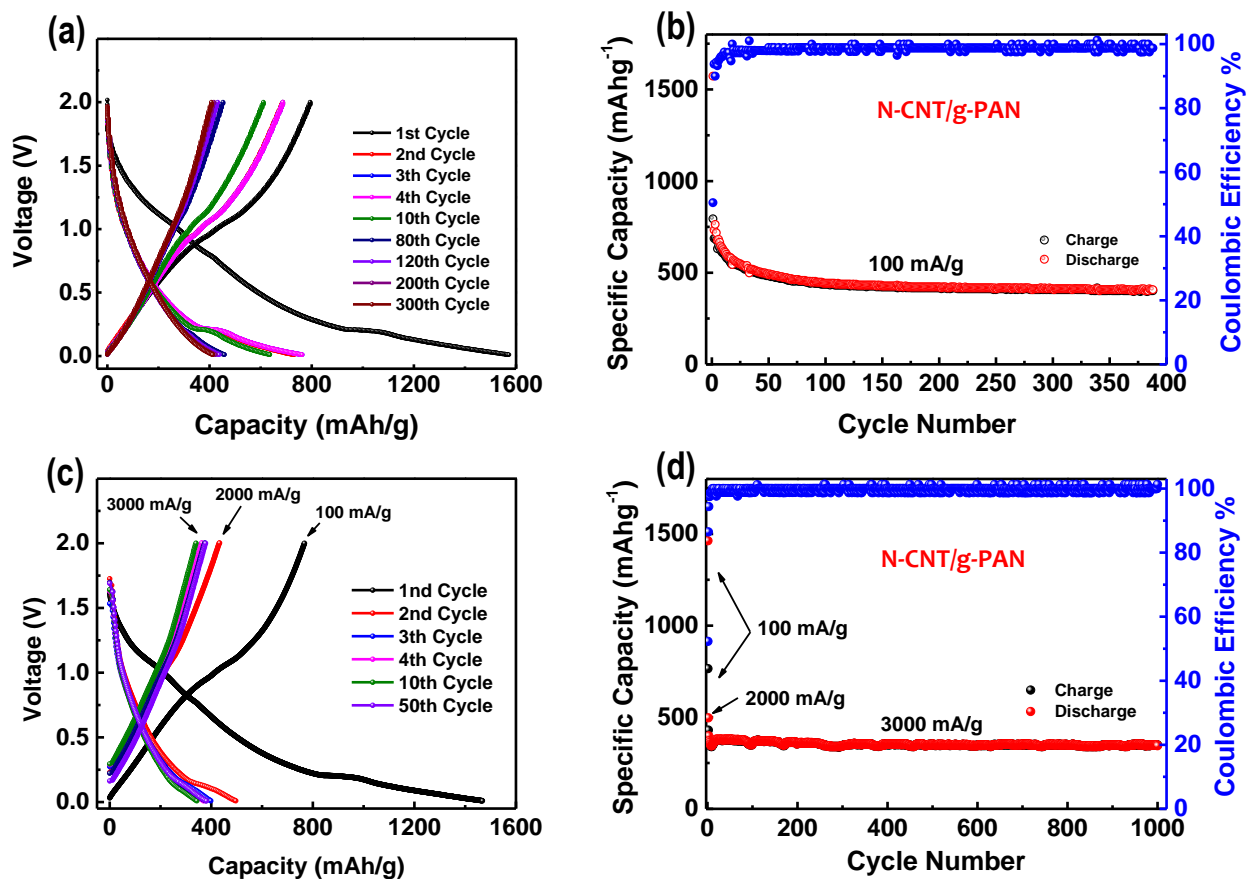


Figure (6.16) Voltage profile and corresponding the cycling stability of N-CNT/g-PAN electrodes (a-b) cycled at low current rate of 100 mA g⁻¹ for 400 cycles, and (c-d) cycled at a high current density of 3000 mA g⁻¹ for long cycling of 1000 cycles.

To further study the lithiation/delithiation electrochemistry of our composite, cyclic voltammetry (CV) was recorded. **Figure 6.17a** reveals the initial five cycles of the NSi@N-CNT/g-PAN composite at a scanning rate of 0.05 mV s⁻¹ over the voltage range of 0.01 to 1.5 V. During the initial lithiation process, a broad cathodic peak appearing from 0.6 to 1.05 V is associated with the formation of the SEI layer, and disappears in the second cycle, which indicates the SEI layer is relatively stable.^{166, 209} In the following cycles, a peak appears at ~ 0.19 V,

suggesting the conversion from crystalline Si to amorphous phase Li_xSi .²¹⁰ During the delithiation process, two distinctive peaks were observed at 0.38 and 0.53 V representing the dealloying process from Li_xSi phase to Si.²¹¹ In addition, the later cycles reveal a gradual increase in the curves' area with lithiation and delithiation processes. In the other hand, CV curves for NSi@N-CNT electrode without g-PAN (**Figure 6.17b**) show similar behavior but with smaller activation peaks due to the lower nitrogen content compared to the NSi@N-CNT/g-PAN electrode, which indicates that incorporation of g-PAN with N-CNT provide high electronic conductivity. We believe this is because after activation, Si becomes more electrochemically active. This is likely due to the highly interconnected network of our design, allowing for high contact of Si with our designed carbon support even after the initial pulverization.

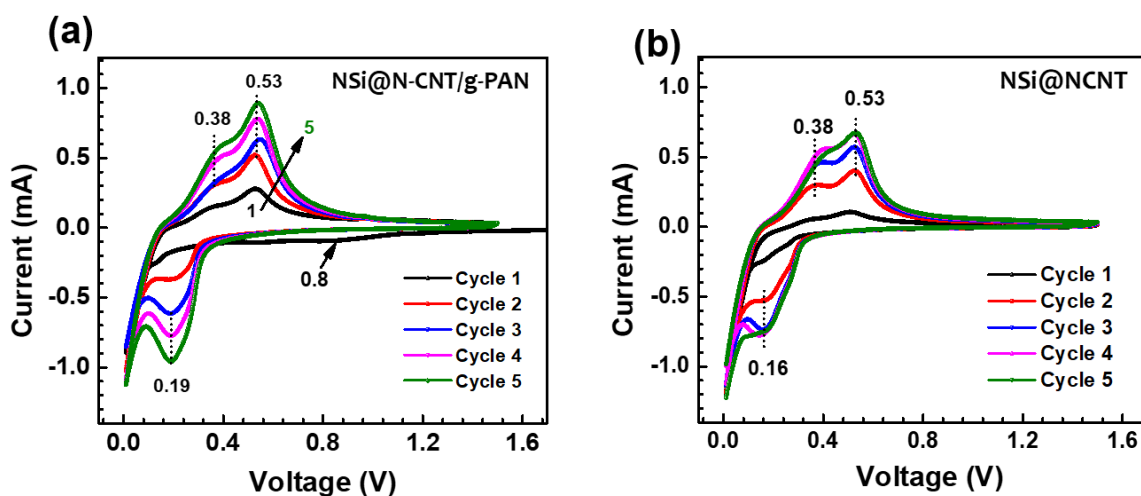


Figure (6.17) Cycling voltammetry curves of a coin-type half-cell: (a) for the NSi@N-CNT/g-PAN electrode, and (b) for the NSi@N-CNT electrode.

For further investigation of the enhancement in the electrical conductivity, the as-prepared composite of NSi@N-CNT/g-PAN was characterized using electrochemical impedance spectroscopy (EIS), with results compared for NSi@N-CNT, NSi/PVDF/Super P, and NSi/g-PAN electrodes after 10 cycles as shown in **Figure 6.18**. The semicircles are associated with charge-transfer resistance, whereas the straight sloping lines represent the diffusion resistance through the bulk of the Si material. The charge-transfer resistance of the NSi@N-CNT/g-PAN electrode is lower than all the other electrodes, which is attributed to the higher electronic conductivity due to the high-level of N-doping materials (N-CNT and g-PAN) in the electrode structure. Also, the Si is attached to the surface of long N-CNTs, which improve the charge transfer and enhance the conductivity. On the contrary, both electrodes of NSi@N-CNT without g-PAN and NSi/g-PAN without N-CNT have lower electron transport. This improvement of the lithium storage properties of the electrode further supports that the 3D network of flexible sheets of g-PAN and long channels of N-CNTs accelerated the electron and lithium ions diffusion during repeating cycling.

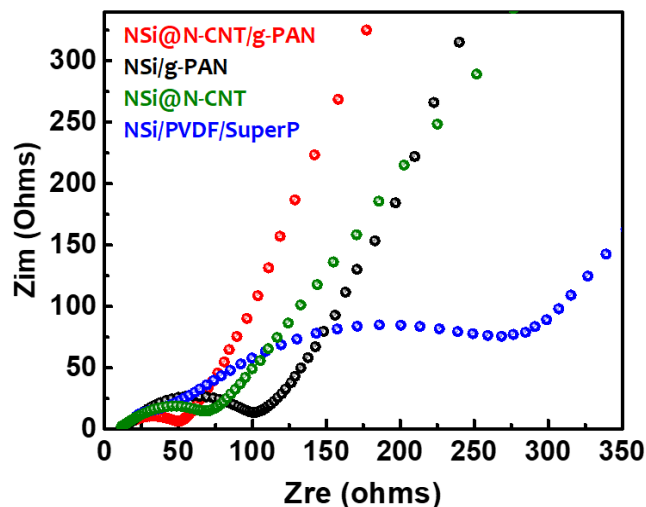


Figure (6.18) Electrochemical impedance of the NSi@N-CNT, NSi/g-PAN, NSi/PVDF/Super P, and NSi@N-CNT/g-PAN electrodes after 10 cycles.

For further characterization of our design, the different morphology of composite electrodes was characterized before and after cycling by TEM characterization to see the electrode structure evolves with the number of cycles (**Figure 6.19**). For the TEM image (**Figure 6.19b**) after 50 cycles, the electrode still has almost the same morphology and Si particles are still attached to the N-CNTs and wrapped by g-PAN. In contrast, after long cycling, the morphology of the electrode surface is changed to a wrinkle-like morphology due to the irreversible volume expansion caused by repeated cycling. It shows that the Si nanoparticles are still encased by a framework of g-PAN nanosheets and appears to be still physically connected with N-CNTs. We attribute this to the bond between the Si particles and N-CNTs. It demonstrates that the efficiently engineered structure of our electrode design, which is associated with the incorporation of nitrogen, is critical for the high stable cyclability of the electrode. Also, the stable interaction between the Si particles and N-CNTs supported the electron transfer and lithium ion diffusion between the whole electrode structure.

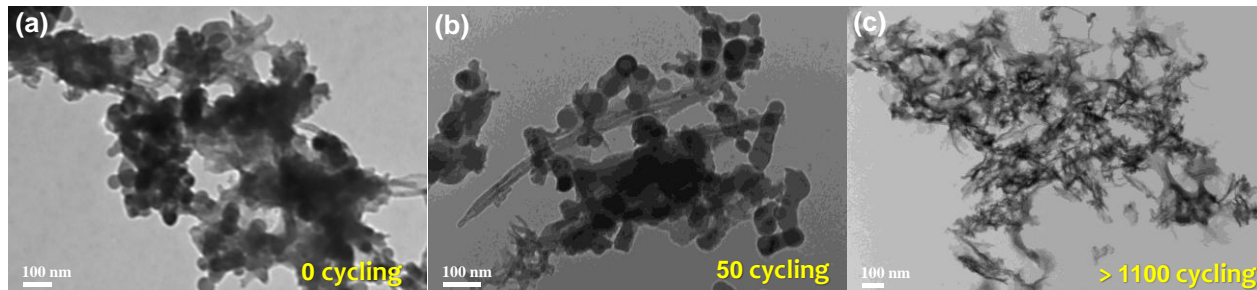


Figure (6.19) TEM images of the NSi@N-CNT/g-PAN nanocomposite before cycling, after 50 cycles, and after more than 1100 cycles.

In conclusion, a novel design of a 3D robust multi-leveled architecture of NSi@N-CNT/g-PAN was developed. This design was able to serve the role of the self-assembly structure of Si material while offering enhanced structural and transport properties. This unique network of N-CNT/g-PAN function as structural reinforcement, which enhances the electron transfer and lithium diffusion and maintains the whole integrity of the electrode as well as building of stable SEI layer. The Si particles were tightly linked to the N-CNT walls by stable interaction and shielded by flexible nanosheets of g-PAN, which can accommodate the volume expansion of Si particles during lithiation and delithiation. Significantly, the impedance of our composite decreased with the incorporation of graphenized PAN, thus significantly improving the high rate discharge capacity and prolonging the long cycle-life performance of the anode. As a result, the unique structure of this composite provides long-term cycling stability for about 1100 cycles with high capacity cycled at a high current rate of 3000 mA g^{-1} , revealing a significant improvement in cycle life compared with that NSi@N-CNT electrode without g-PAN.

Conclusions and Future Work

7.1 Conclusion and Summary

In this thesis, the Si material was chosen to be the research topic to improving the energy density of LIBs. Different strategies were used to overcome the practical operation problems of Si anode by designing novel electrode materials with a flexible structure to maintain electrode integrity. Based on the results conducted in this thesis, advanced electrode structures were successfully designed to address the issues associated with Si-based anodes in LIBs.

In chapter four, a novel polymer composite of PVP and PAN was designed to use as a conductive binder for Si anodes. The excellent performance of the electrode was attributed to the synergistic effect of polymer composite chemistry and post-treatment of the electrodes. Also, the distribution of polymeric materials within the composite electrode is the principal parameter, which affects the electrode morphology. The polymeric binders distribution within the electrode depends mainly on the slurry preparation and mixing methods. Therefore, strong chemical bonds can be formed around the Si particles by reacting the copolymer with the polar groups on the Si particles surface during the slurry preparation. Moreover, we treated the electrodes at different annealing temperatures, and we found that the best electrochemical performance and stability for 600 cycles at 750 °C. In addition, controlling polymers' structure with a sufficiently high capacity and reasonable stability has been obtained. Different characteristics of the electrodes with and without PVP elucidated interesting mechanisms of the coatings formation process over Si particles. We found that the self-assembled PVP layer around the Si nanoparticles allowed for an amplified oxidation of Si producing a SiO₂ shell while the decomposition of PAN introduced a nitrogen-rich porous carbon coating derived from PAN over the SiO₂ layer. When combined PVP with the

network of conductive N-graphene nanosheets, this material was able to deliver excellent cycle stability for 600 cycles at a higher current density of 3000 mA g^{-1} as well as an excellent rate capability.

In chapter five, we successfully designed a multifunctional composite binder of cross-linking PAA and CMC spine with graphenized PAN followed by a facile and economical slow heat treatment process to improve the cycling performance of Si-based anode for LIBs. This design was able to serve the role of an Si-interactive material while offering enhanced structural and transport properties. The chemically modified polymers will change the scaffold environment around the Si nanoparticles in the electrode architecture, making it a highly stable and conductive. We found that by combining PAA-CMC with g-PAN, a robust 3D structure constituting of Si nanoparticles with an oxidized shell wrapped with porous carbon and N-doped graphene nanosheets is formed. This nanoarchitecture provides multi-point interactions with the Si particles, which efficiently limits the volume change and prevents the aggregation of Si particles during cycling. The cross-linked carboxyl groups from PAA and CMC offered a robust 3D cross-linked network, anchoring SiO_2 coated Si nanoparticles onto a highly-porous carbon scaffold, forming a stable solid electrolyte interphase. Also, the intimate contact of Si particle with the conductive network significantly improves the electrical conductivity of the Si anode. Moreover, due to the flexibility and good mechanical properties, the nitrogen graphenized-like nanosheets provide multiple channels for fast ion and electron transportation, which greatly enhances the cycle life. Benefiting from this novel structural design, excellent mechanical stability, good conductivity, and superior cyclic stability was achieved. This composite anode not only exhibits a high initial capacity of $3472.6 \text{ mAh g}^{-1}$ with an initial Coulombic efficiency of 89.1%, but also provides a high discharge specific capacity of 1563 mAh g^{-1} after 650 cycles under a high current density of 3000 mA g^{-1} .

This performance improvement indicates that constructing the interconnected PAA-CMC and g-PAN structure is an efficient technique to design nanostructured Si-based anode for the next-generation of LIBs and other related energy storage systems.

Finally, in chapter six, we have successfully designed a 3D robust multi-leveled architecture of NSi@N-CNT/g-PAN to improve the cycle life of Si anode. This design was able to serve the role of a Si material while offering enhanced structural and transport properties. By systematically combining N-CNT with g-PAN nanosheets, a 3D web-like structure of flexible and self-standing NSi@N-CNT/g-PAN composite anode was fabricated. This unique network function as structural reinforcement which improves the electron diffusion and maintain the whole integrity of the electrode. The Si particles were tightly attached to the N-CNT walls and shielded by flexible nanosheets of g-PAN, which overcome mechanical breaking during the volume expansion of Si particles and build SEI films on the surface. Significantly, the impedance of the composite decreased with the incorporation of graphenized PAN, thus improved the high rate discharge capacity and long cycle-life performance of the electrode. As a result, the unique morphology and structure of this composite provide superior electrochemical performance of long-term cycling stability for about 1100 cycles at a high current rate revealing a significant improvement in cycle life compared with that NSi@N-CNT electrode without g-PAN. Also, it reveals remarkable improvement in rate capabilities compared to NSi@N-CNT electrode. These improvements could be attributed to the robust 3D carbon network with the incorporation of N doping in N-CNT and g-PAN. These results indicate that the incorporation of g-PAN with N-CNTs provides a strong and flexible network, which probably helps to prevent Si decrepitation and greatly improve the electrochemical performance of Si-based flexible anode.

7.2 Suggestions for Future Work

Based on the excellent results that were revealed in this thesis, excellent performances of the Si anodes were successfully confirmed. However, in order to facilitate the commercialization of Si-based anodes in LIBs, it is necessary to have long-term cycling stability, low cost of production, and high energy and power density. Therefore, further advancements in electrode structures are needed. This, in addition to the stability, will provide a breathable environment that compensates for the mechanical instability of the Si anode during the charge/discharge processes and maintains a stable SEI leading to improvements in the performance and an increase in the stability of the batteries. To make these fabrication procedures more attractive from an economic point of view, future work will focus on improving the electrochemical performance of Si anodes comprehensively, using high performance nanostructured materials with efficient low-cost techniques, as follows:

- 1) Preparing 3D of cross-linking (PAA-CMC) with g-PAN that supported Si nanoparticles has proven to be a facile and effective method for enhancing the cycling stability of Si-based anode for LIBs as shown in chapter 5. However, the high loading with long cycling need to improve. To stabilize the entrapped Si nanoparticles and improve the loading in this structure, the N-CNT materials can be added to the composite in future work. We believe this nanoarchitecture will provide high stability and long cycle life with high loading. Different temperatures of SHT will apply to investigate the effect of these temperatures on the electrode structure.

- 2) Based on the long cycling with excellent stability of N-CNT/g-PAN electrode materials that were conducted in the last work, we are looking to add different ratios of Si nanoparticles to this structure in order to increase the specific capacity of the anode. We will use different temperatures of SHT, starting from 300 °C, which is related to the cyclization reaction of PAN, to investigate

the effect of these temperatures on the electrode structure. We believe also this nanoarchitecture will provide high stability and long cycle life.

3) Optimizing the post-treatment method to treat the Si-based anodes, will lead to changes in the electrode nanoarchitectures and provide significant performance. To further investigate the binder carbonization and the interaction with the Si nanoparticles, the future research in this area could modify the SHT conditions such as different temperatures, and atmosphere, and different heating rates to the freshly prepared electrodes.

4) Applying the chemical modification of blend binders to the metallurgical silicon. While different techniques have been used to fabricate Si anode using Si nanoparticles (< 70nm) to achieve excellent performance in LIBs, some of these techniques require expensive materials or complicated reaction environments. Therefore, an urgent challenge is to develop Si anodes using a cost-effective technique with low-cost raw materials while being capable of maintaining its high capacity during the cycling process. The ultimate challenge is to use large-sized silicon called the metallurgical silicon (SiMP) as an active material. This material is abundant and inexpensive, which can reduce the overall cost of battery production. In future work, we will apply the above concept of chemical modification of PVP/g-PAN, PAA-CMC/g-PAN, and N-CNT/g-PAN polymer composites to the SiMP as an alternative raw material due to its low cost, easy commercial availability, and more promising electrode materials towards practical industrial applications. Similar techniques of electrode fabrication described in previous approaches will be used. The SiMP/binders composite will be annealed using the same slow heat treatment technique with different temperatures to produce carbon coating on the Si surface.

5) Applying reinforcement additives for high performance of Li-ion batteries: Si is a semiconductor and has poor conductivity. Also, during the alloying processes with lithium, the

electron is not easy to insert into the Si particles, which causes the alloying process to slow down. Therefore, improving the conductivity of the Si electrode is very important for the lithiation and delithiation processes. Therefore, we will apply different heteroatoms such as selenium (Se) or boron (B) into the carbon nanotube (Se-CNT or B-CNT) or graphene oxide (SeGO or BGO), which can modify the charge redistribution among carbon atoms. This will lead to the improvement of the charge transfer, thus we expected it to enhance the electrical conductivity of the electrode. This will open a new direction for the development of the Si-based anode. These additives will be used with the previous composites that have been mentioned above. The reasons for adding these reinforcements are:

- a) Improving the conductivity of the electrode which will allow faster charge and discharge.
- b) Enhancing the cycle stability and rate capability of the Si electrode.
- c) Forming an elastic and flexible skeleton around the Si particles.
- d) Forming anchor sites through doping with heteroatoms, to which Si will covalently attract.

References

1. R. Marom, S. F. Amalraj, N. Leifer, D. Jacob and D. Aurbach, *J. Mater. Chem.*, 2011, **21**, 9938-9954.
2. X. Su, Q. Wu, J. Li, X. Xiao, A. Lott, W. Lu, B. W. Sheldon and J. Wu, *Adv. Energy Mater.*, 2014, **4**, 1300882.
3. M. M. Thackeray, C. Wolverton and E. D. Isaacs, *Energy Environ. Sci.*, 2012, **5**, 7854-7863.
4. N.-S. Choi, Z. Chen, S. A. Freunberger, X. Ji, Y.-K. Sun, K. Amine, G. Yushin, L. F. Nazar, J. Cho and P. G. Bruce, *Angew. Chem. Int. Ed.*, 2012, **51**, 9994-10024.
5. G.-A. Nazri and G. Pistoia, *Lithium batteries: science and technology*, Springer Science & Business Media, 2008.
6. V. Etacheri, R. Marom, R. Elazari, G. Salitra and D. Aurbach, *Energy Environ. Sci.*, 2011, **4**, 3243-3262.
7. W.-J. Zhang, *J. Power Sources*, 2011, **196**, 13-24.
8. C. Zhang, F. Yang, D. Zhang, X. Zhang, C. Xue, Y. Zuo, C. Li, B. Cheng and Q. Wang, *RSC Adv.*, 2015, **5**, 15940-15943.
9. M. Winter and R. J. Brodd, *Chem. Rev.*, 2004, **104**, 4245-4270.
10. F. Cheng, J. Liang, Z. Tao and J. Chen, *Adv. Mater.*, 2011, **23**, 1695-1715.
11. H. Li, Z. Wang, L. Chen and X. Huang, *Adv. Mater.*, 2009, **21**, 4593-4607.
12. B. Xu, D. Qian, Z. Wang and Y. S. Meng, *Materials Science and Engineering: R: Reports*, 2012, **73**, 51-65.
13. C. K. Chan, H. Peng, G. Liu, K. McIlwrath, X. F. Zhang, R. A. Huggins and Y. Cui, *Nat Nano*, 2008, **3**, 31-35.
14. S. Y. Reece, J. A. Hamel, K. Sung, T. D. Jarvi, A. J. Esswein, J. J. H. Pijpers and D. G. Nocera, *Science*, 2011, **334**, 645-648.
15. H. Wu and Y. Cui, *Nano Today*, 2012, **7**, 414-429.
16. D. Aurbach, *J. Power Sources*, 2000, **89**, 206-218.
17. H. Kim, M. Seo, M.-H. Park and J. Cho, *Angewandte Chemie International Edition*, 2010, **49**, 2146-2149.
18. J. Yang, M. Winter and J. O. Besenhard, *Solid State Ionics*, 1996, **90**, 281-287.
19. M. Winter and J. O. Besenhard, *Electrochim. Acta*, 1999, **45**, 31-50.
20. M. Ashuri, Q. He and L. L. Shaw, *Nanoscale*, 2016, **8**, 74-103.
21. F.-S. Li, Y.-S. Wu, J. Chou, M. Winter and N.-L. Wu, *Adv. Mater.*, 2015, **27**, 130-137.

22. A. Volta, *Philos. Trans. R. Soc. London*, 1800, **90**, 403-431.
23. M. R. Palacin, *Chem. Soc. Rev.*, 2009, **38**, 2565-2575.
24. Thomas B. Reddy and D. Linden, *HANDBOOK OF BATTERIES*, McGraw-Hill Education., 4th edn., 2011.
25. Y. Nishi, *J. Power Sources*, 2001, **100**, 101-106.
26. N. Nitta, F. Wu, J. T. Lee and G. Yushin, *Mater. Today*, 2015, **18**, 252-264.
27. H. Lee, M. Yanilmaz, O. Toprakci, K. Fu and X. Zhang, *Energy Environ. Sci.*, 2014, **7**, 3857-3886.
28. R. Hausbrand, G. Cherkashinin, H. Ehrenberg, M. Gröting, K. Albe, C. Hess and W. Jaegermann, *Materials Science and Engineering: B*, 2015, **192**, 3-25.
29. C. Sigala, D. Guyomard, A. Verbaere, Y. Piffard and M. Tournoux, *Solid State Ionics*, 1995, **81**, 167-170.
30. H. Fang, Z. Wang, B. Zhang, X. Li and G. Li, *Electrochem. Commun.*, 2007, **9**, 1077-1082.
31. M. Wohlfahrt-Mehrens, in *Encyclopedia of Electrochemical Power Sources*, Elsevier, Amsterdam, 2009, 2, 318-327.
32. T. Zhang, D. Li, Z. Tao and J. Chen, *Prog. Nat. Sci.: Mater. Int.*, 2013, **23**, 256-272.
33. J. Molenda and M. Molenda, in *Metal, Ceramic and Polymeric Composites for Various Uses*, ed. J. Cuppoletti, InTech, Rijeka, 2011, 10.5772/21635, p. Ch. 30.
34. S. Yang, P. Y. Zavalij and M. Stanley Whittingham, *Electrochem. Commun.*, 2001, **3**, 505-508.
35. S.-Y. Chung, J. T. Bloking and Y.-M. Chiang, *Nat. Mater.*, 2002, **1**, 123-128.
36. K. Yan, H.-W. Lee, T. Gao, G. Zheng, H. Yao, H. Wang, Z. Lu, Y. Zhou, Z. Liang, Z. Liu, S. Chu and Y. Cui, *Nano Lett.*, 2014, **14**, 6016-6022.
37. H. Ye, S. Xin, Y.-X. Yin, J.-Y. Li, Y.-G. Guo and L.-J. Wan, *J. Am. Chem. Soc.*, 2017, **139**, 5916-5922.
38. M. Inaba, in *Encyclopedia of Electrochemical Power Sources*, Elsevier, Amsterdam, 2009, 1, 198-208.
39. M. N. Obrovac and V. L. Chevrier, *Chem. Rev.*, 2014, **114**, 11444-11502.
40. M. N. Obrovac and L. Christensen, *Electrochem. Solid-State Lett.*, 2004, **7**, A93-A96.
41. C. J. Wen and R. A. Huggins, *J. Solid State Chem.*, 1981, **37**, 271-278.
42. T. H. Hwang, Y. M. Lee, B.-S. Kong, J.-S. Seo and J. W. Choi, *Nano Lett.*, 2012, **12**, 802-807.
43. Y. Oumellal, N. Delpuech, D. Mazouzi, N. Dupre, J. Gaubicher, P. Moreau, P. Soudan, B. Lestriez and D. Guyomard, *J. Mater. Chem.*, 2011, **21**, 6201-6208.
44. X. H. Liu, L. Zhong, S. Huang, S. X. Mao, T. Zhu and J. Y. Huang, *ACS Nano*, 2012, **6**, 1522-1531.

45. D. Larcher, S. Beattie, M. Morcrette, K. Edström, J. C. Jumas and J. M. Tarascon, *J. Mater. Chem.*, 2007, **17**, 3759-3772.
46. *ECS Meeting Abstracts*, 2014.
47. B. A. Boukamp, G. C. Lesh and R. A. Huggins, *J. Electrochem. Soc.*, 1981, **128**, 725-729.
48. J. W. Choi and D. Aurbach, *Nature Reviews Materials*, 2016, **1**, 16013.
49. K. Xu, *Chem. Rev.*, 2014, **114**, 11503-11618.
50. K. Xu, *Chem. Rev.*, 2004, **104**, 4303-4418.
51. S. Hu, Y. Li, J. Yin, H. Wang, X. Yuan and Q. Li, *Chem. Eng. J.*, 2014, **237**, 497-502.
52. J. Xu, Q. Zhang and Y.-T. Cheng, *J. Electrochem. Soc.*, 2016, **163**, A401-A405.
53. L. Wei and Z. Hou, *J. Mater. Chem, A*, 2017, **5**, 22156-22162.
54. C. C. Nguyen, T. Yoon, D. M. Seo, P. Guduru and B. L. Lucht, *ACS Appl. Mater. Interfaces*, 2016, **8**, 12211-12220.
55. S.-L. Chou, Y. Pan, J.-Z. Wang, H.-K. Liu and S.-X. Dou, *Phys. Chem. Chem. Phys.*, 2014, **16**, 20347-20359.
56. J. Liu, Q. Zhang, T. Zhang, J.-T. Li, L. Huang and S.-G. Sun, *Adv. Funct. Mater.*, 2015, **25**, 3599-3605.
57. Y. K. Jeong, T.-w. Kwon, I. Lee, T.-S. Kim, A. Coskun and J. W. Choi, *Nano Lett.*, 2014, **14**, 864-870.
58. S.-B. Son, B. Kappes and C. Ban, *Isr. J. Chem.*, 2015, **55**, 558-569.
59. G. Liu, S. Xun, N. Vukmirovic, X. Song, P. Olalde-Velasco, H. Zheng, V. S. Battaglia, L. Wang and W. Yang, *Adv. Mater.*, 2011, **23**, 4679-4683.
60. E. Panjaitan, A. Manaf, B. Soegijono and E. Kartini, *Procedia Chem.*, 2012, **4**, 60-64.
61. S. Komaba, K. Shimomura, N. Yabuuchi, T. Ozeki, H. Yui and K. Konno, *The Journal of Physical Chemistry C*, 2011, **115**, 13487-13495.
62. H.-K. Park, B.-S. Kong and E.-S. Oh, *Electrochem. Commun.*, 2011, **13**, 1051-1053.
63. S. Komaba, T. Ozeki, N. Yabuuchi and K. Shimomura, *Electrochemistry*, 2011, **79**, 6-9.
64. A. Magasinski, B. Zdyrko, I. Kovalenko, B. Hertzberg, R. Burtovyy, C. F. Huebner, T. F. Fuller, I. Luzinov and G. Yushin, *ACS Appl. Mater. Interfaces*, 2010, **2**, 3004-3010.
65. L. Gong, M. H. T. Nguyen and E.-S. Oh, *Electrochem. Commun.*, 2013, **29**, 45-47.
66. S. Huang, J. Ren, R. Liu, M. Yue, Y. Huang and G. Yuan, *International Journal of Energy Research*,
67. J. Li, R. B. Lewis and J. R. Dahn, *Electrochem. Solid-State Lett.*, 2007, **10**, A17-A20.

68. J. Li, L. Christensen, M. N. Obrovac, K. C. Hewitt and J. R. Dahn, *J. Electrochem. Soc.*, 2008, **155**, A234-A238.
69. W.-R. Liu, Z.-Z. Guo, W.-S. Young, D.-T. Shieh, H.-C. Wu, M.-H. Yang and N.-L. Wu, *J. Power Sources*, 2005, **140**, 139-144.
70. J. Li, R. Doig, H. Liu, G. Botton and J. R. Dahn, *J. Electrochem. Soc.*, 2016, **163**, A2841-A2848.
71. M. He, L.-X. Yuan, W.-X. Zhang, X.-L. Hu and Y.-H. Huang, *The Journal of Physical Chemistry C*, 2011, **115**, 15703-15709.
72. U. Kasavajjula, C. Wang and A. J. Appleby, *J. Power Sources*, 2007, **163**, 1003-1039.
73. N. S. Hochgatterer, M. R. Schweiger, S. Koller, P. R. Raimann, T. Wöhrle, C. Wurm and M. Winter, *Electrochem. Solid-State Lett.*, 2008, **11**, A76-A80.
74. J. S. Bridel, T. Azaïs, M. Morcrette, J. M. Tarascon and D. Larcher, *J. Electrochem. Soc.*, 2011, **158**, A750.
75. I. Kovalenko, B. Zdyrko, A. Magasinski, B. Hertzberg, Z. Milicev, R. Burtovyy, I. Luzinov and G. Yushin, *Science*, 2011, **334**, 75-79.
76. M. Ling, Y. Xu, H. Zhao, X. Gu, J. Qiu, S. Li, M. Wu, X. Song, C. Yan, G. Liu and S. Zhang, *Nano Energy*, 2015, **12**, 178-185.
77. F. M. Hassan, R. Batmaz, J. Li, X. Wang, X. Xiao, A. Yu and Z. Chen, *Nat. Commun.*, 2015, **6**, 8597.
78. H. Zhao, A. Du, M. Ling, V. Battaglia and G. Liu, *Electrochim. Acta*, 2016, **209**, 159-162.
79. S.-J. Park, H. Zhao, G. Ai, C. Wang, X. Song, N. Yuca, V. S. Battaglia, W. Yang and G. Liu, *J. Am. Chem. Soc.*, 2015, **137**, 2565-2571.
80. S. Xun, B. Xiang, A. Minor, V. Battaglia and G. Liu, *J. Electrochem. Soc.*, 2013, **160**, A1380-A1383.
81. H. Zhao, Y. Wei, R. Qiao, C. Zhu, Z. Zheng, M. Ling, Z. Jia, Y. Bai, Y. Fu, J. Lei, X. Song, V. S. Battaglia, W. Yang, P. B. Messersmith and G. Liu, *Nano Lett.*, 2015, **15**, 7927-7932.
82. G. S. Bumbrah and R. M. Sharma, *Egyptian Journal of Forensic Sciences*, 2016, **6**, 209-215.
83. R. Müller, *Industrial & Engineering Chemistry Analytical Edition*, 1941, **13**, 667-754.
84. M. Armand and J. M. Tarascon, *Nature*, 2008, **451**, 652-657.
85. J. M. Tarascon and M. Armand, *Nature*, 2001, **414**, 359-367.
86. C. Zhang, F. Yang, D. Zhang, X. Zhang, C. Xue, Y. Zuo, C. Li, B. Cheng and Q. Wang, *RSC Advances*, 2015, **5**, 15940-15943.
87. F. M. Hassan, Q. Hu, J. Fu, R. Batmaz, J. Li, A. Yu, X. Xiao and Z. Chen, *ACS Appl. Mater. Interfaces*, 2017, **9**, 20603-20612.

88. H. Li, Z. Wang, L. Chen and X. Huang, *Adv. Mater.*, 2009, **21**, 4593-4607.
89. J. R. Szczech and S. Jin, *Energy Environ. Sci.*, 2011, **4**, 56-72.
90. J. O. Besenhard, J. Yang and M. Winter, *J. Power Sources*, 1997, **68**, 87-90.
91. C.-Y. Chou and G. S. Hwang, *J. Power Sources*, 2014, **263**, 252-258.
92. K. Feng, W. Ahn, G. Lui, H. W. Park, A. G. Kashkooli, G. Jiang, X. Wang, X. Xiao and Z. Chen, *Nano Energy*, 2016, **19**, 187-197.
93. D. C. Marcano, D. V. Kosynkin, J. M. Berlin, A. Sinitskii, Z. Sun, A. Slesarev, L. B. Alemany, W. Lu and J. M. Tour, *ACS Nano*, 2010, **4**, 4806-4814.
94. F. M. Hassan, V. Chabot, A. R. Elsayed, X. Xiao and Z. Chen, *Nano Lett.*, 2014, **14**, 277-283.
95. H. Niu, J. Zhang, Z. Xie, X. Wang and T. Lin, *Carbon*, 2011, **49**, 2380-2388.
96. Y. Liu, Y. Liu, J.-H. Lee, C. Lee, M. Park and H.-Y. Kim, *Compos. Sci. Technol.*, 2015, **117**, 404-409.
97. K. Tang, Y. Li, H. Cao, C. Su, Z. Zhang and Y. Zhang, *Electrochim. Acta*, 2016, **190**, 678-688.
98. R. F. Ribeiro, L. C. Pardini, N. P. Alves and C. A. R. Brito Júnior, *Polímeros*, 2015, **25**, 523-530.
99. R. Devasia, C. P. R. Nair, P. Sivadasan, B. K. Katherine and K. N. Ninan, *J. Appl. Polym. Sci.*, 2003, **88**, 915-920.
100. H. Zhang, L. Quan and L. Xu, *Fibers and Polymers*, 2015, **16**, 263-270.
101. Y. T. Yeo, S. H. Goh and S. Y. Lee, *J. Macromol. Sci., Part A*, 1997, **34**, 597-603.
102. Q. Guo, J. Huang and X. Li, *Eur. Polym. J.*, 1996, **32**, 423-426.
103. Y. Jiang, D. Fang, G. Song, J. Nie, B. Chen and G. Ma, *New J. Chem.*, 2013, **37**, 2917-2924.
104. C. Li, C. Liu, W. Wang, J. Bell, Z. Mutlu, K. Ahmed, R. Ye, M. Ozkan and C. S. Ozkan, *Chem. Commun.*, 2016, **52**, 11398-11401.
105. G. D. Sorarù, S. Modena, P. Bettotti, G. Das, G. Mariotto and L. Pavesi, *Appl. Phys. Lett.*, 2003, **83**, 749-751.
106. F. M. Hassan, R. Batmaz, J. Li, X. Wang, X. Xiao, A. Yu and Z. Chen, *Nat. Commun.*, 2015, **6**, 8597.
107. L. Y. Yang, H. Z. Li, J. Liu, Z. Q. Sun, S. S. Tang and M. Lei, *Sci. Rep.*, 2015, **5**, 10908.
108. M. Beidaghi and C. Wang, *Adv. Funct. Mater.*, 2012, **22**, 4501-4510.
109. T. Hu, L. Chen, K. Yuan and Y. Chen *Chem. - Eur. J.*, 2014, **20**, 17178-17184.
110. S. H. Choi, D. S. Jung, J. W. Choi and Y. C. Kang, *Chemistry (Weinheim an der Bergstrasse, Germany)*, 2015, **21**, 2076-2082.
111. S.-H. Kim, S.-H. Yook, A. G. Kannan, S. K. Kim, C. Park and D.-W. Kim, *Electrochim. Acta*, 2016, **209**, 278-284.

112. J. Yu, J. G. Shapter, J. S. Quinton, M. R. Johnston and D. A. Beattie, *Phys. Chem. Chem. Phys.*, 2007, **9**, 510-520.
113. J. Li, D. Zhang, J.-b. Guo and J. Wei, *Chin. J. Chem. Phys.*, 2014, **27**, 718-724.
114. M. Thakur, S. L. Sinsabaugh, M. J. Isaacson, M. S. Wong and S. L. Biswal, *Sci. Rep.*, 2012, **2**, 795.
115. J. S. Kim, D. Byun and J. K. Lee, *Current Applied Physics*, 2014, **14**, 596-602.
116. J. Yan, Q. Wang, T. Wei, L. Jiang, M. Zhang, X. Jing and Z. Fan, *ACS Nano*, 2014, **8**, 4720-4729.
117. S. Some, P. Bhunia, E. Hwang, K. Lee, Y. Yoon, S. Seo and H. Lee, *Chem. - Eur. J.*, 2012, **18**, 7665-7670.
118. S. Stankovich, D. A. Dikin, R. D. Piner, K. A. Kohlhaas, A. Kleinhammes, Y. Jia, Y. Wu, S. T. Nguyen and R. S. Ruoff, *Carbon*, 2007, **45**, 1558-1565.
119. Z. Xing, Z. Ju, Y. Zhao, J. Wan, Y. Zhu, Y. Qiang and Y. Qian, *Sci. Rep.*, 2016, **6**, 26146.
120. L. G. Bulusheva, M. A. Kanygin, V. E. Arkhipov, K. M. Popov, Y. V. Fedoseeva, D. A. Smirnov and A. V. Okotrub, *The Journal of Physical Chemistry C*, 2017, **121**, 5108-5114.
121. M. Zhong, E. K. Kim, J. P. McGann, S.-E. Chun, J. F. Whitacre, M. Jaroniec, K. Matyjaszewski and T. Kowalewski, *J. Am. Chem. Soc.*, 2012, **134**, 14846-14857.
122. M. Ge, J. Rong, X. Fang and C. Zhou, *Nano Lett.*, 2012, **12**, 2318-2323.
123. G. E. Blomgren, *J. Electrochem. Soc.*, 2017, **164**, A5019-A5025.
124. M. Li, J. Lu, Z. Chen and K. Amine, *Adv. Mater.*, 2018, **30**, 1800561.
125. A. S. Aricò, P. Bruce, B. Scrosati, J.-M. Tarascon and W. van Schalkwijk, *Nature Materials*, 2005, **4**, 366.
126. J. Cho, *J. Mater. Chem.*, 2010, **20**, 4009-4014.
127. T. D. Hatchard and J. R. Dahn, *J. Electrochem. Soc.*, 2004, **151**, A838-A842.
128. K. Zhao, M. Pharr, Q. Wan, W. L. Wang, E. Kaxiras, J. J. Vlassak and Z. Suo, *J. Electrochem. Soc.*, 2012, **159**, A238-A243.
129. M. N. Obrovac and L. J. Krause, *J. Electrochem. Soc.*, 2007, **154**, A103-A108.
130. L. Y. Beaulieu, T. D. Hatchard, A. Bonakdarpour, M. D. Fleischauer and J. R. Dahn, *J. Electrochem. Soc.*, 2003, **150**, A1457-A1464.
131. E. Peled, *J. Electrochem. Soc.*, 1979, **126**, 2047-2051.
132. E. Peled and S. Menkin, *J. Electrochem. Soc.*, 2017, **164**, A1703-A1719.
133. J. Christensen and J. Newman, *J. of Solid State Electrochem.*, 2006, **10**, 293-319.
134. C. K. Chan, H. Peng, G. Liu, K. McIlwrath, X. F. Zhang, R. A. Huggins and Y. Cui, *Nat. Nanotechnol.*, 2007, **3**, 31.

135. Y. Yao, M. T. McDowell, I. Ryu, H. Wu, N. Liu, L. Hu, W. D. Nix and Y. Cui, *Nano Lett.*, 2011, **11**, 2949-2954.
136. A. Magasinski, P. Dixon, B. Hertzberg, A. Kvit, J. Ayala and G. Yushin, *Nat Mater*, 2010, **9**, 353-358.
137. W.-R. Liu, J.-H. Wang, H.-C. Wu, D.-T. Shieh, M.-H. Yang and N.-L. Wu, *J. Electrochem. Soc.*, 2005, **152**, A1719-A1725.
138. W. Porcher, S. Chazelle, A. Boulineau, N. Mariage, J. P. Alper, T. Van Rompaey, J.-S. Bridel and C. Haon, *J. Electrochem. Soc.*, 2017, **164**, A3633-A3640.
139. B. Koo, H. Kim, Y. Cho, K. T. Lee, N.-S. Choi and J. Cho, *Angew. Chem. Int. Ed.*, 2012, **51**, 8762-8767.
140. J. S. Bridel, T. Azaïs, M. Morcrette, J. M. Tarascon and D. Larcher, *Chem. Mater.*, 2010, **22**, 1229-1241.
141. A. Magasinski, B. Zdyrko, I. Kovalenko, B. Hertzberg, R. Burtovyy, C. F. Huebner, T. F. Fuller, I. Luzinov and G. Yushin, *ACS Appl. Mater. Interfaces*, 2010, **2**, 3004-3010.
142. S. Jiangxuan, Z. Mingjiong, Y. Ran, X. Terrence, G. M. L., T. Duihai, Y. Zhaoxin, R. Michael and W. Donghai, *Adv. Funct. Mater.*, 2014, **24**, 5904-5910.
143. K. Feng, M. Li, Y. Zhang, W. Liu, A. G. Kashkooli, X. Xiao and Z. Chen, *Electrochim. Acta*, 2019, **309**, 157-165.
144. L. Wei, C. Chen, Z. Hou and H. Wei, *Sci. Rep.*, 2016, **6**, 19583.
145. E. Attia, F. M. Hassan, M. Li, R. Batmaz, A. Elkamel and Z. Chen, *J. Mater. Chem. A*, 2017, **5**, 24159-24167.
146. L. Luo, Y. Xu, H. Zhang, X. Han, H. Dong, X. Xu, C. Chen, Y. Zhang and J. Lin, *ACS Appl. Mater. Interfaces*, 2016, **8**, 8154-8161.
147. Z. Wangxi and L. Jie, *Journal of Wuhan University of Technology-Mater. Sci. Ed.*, 2006, **21**, 26-28.
148. Y.-X. Wang, C.-G. Wang, J.-W. Wu and M. Jing, *J. Appl. Polym. Sci.*, 2007, **106**, 1787-1792.
149. R. Batmaz, F. M. Hassan, D. Higgins, Z. P. Cano, X. Xiao and Z. Chen, *J. Power Sources*, 2018, **407**, 84-91.
150. G. S. Krishnan, P. Thomas and N. Murali, *RSC Adv.*, 2016, **6**, 6182-6190.
151. T. Takahagi, I. Shimada, M. Fukuhara, K. Morita and A. Ishitani, *J. Polym. Sci. Part A: Polym. Chem.*, 1986, **24**, 3101-3107.
152. S. Kim, J. Choi, C. Choi, J. Heo, D. W. Kim, J. Y. Lee, Y. T. Hong, H.-T. Jung and H.-T. Kim, *Nano Lett.*, 2018, **18**, 3962-3968.

153. B. Liang, W. Zhan, G. Qi, S. Lin, Q. Nan, Y. Liu, B. Cao and K. Pan, *J. Mater. Chem. A*, 2015, **3**, 5140-5147.
154. S. Lu, J. Yu, Y. Cheng, Q. Wang, A. Barras, W. Xu, S. Szunerits, D. Cornu and R. Boukherroub, *Appl. Surf. Sci.*, 2017, **411**, 163-169.
155. L.-B. Xing, K. Xi, Q. Li, Z. Su, C. Lai, X. Zhao and R. V. Kumar, *J. Power Sources*, 2016, **303**, 22-28.
156. Y. Xie and P. M. A. Sherwood, *Surf. Sci. Spectra*, 1992, **1**, 367-372.
157. Z. Yue, K. R. Benak, J. Wang, C. L. Mangun and J. Economy, *J. Mater. Chem.*, 2005, **15**, 3142-3148.
158. T. Takahagi, I. Shimada, M. Fukuhara, K. Morita and A. Ishitani, *J. Polym. Sci., Part A: Polym. Chem.*, 1986, **24**, 3101-3107.
159. W. Fan, Y.-Y. Xia, W. W. Tjiu, P. K. Pallathadka, C. He and T. Liu, *J. Power Sources*, 2013, **243**, 973-981.
160. Z. Xing, Z. Ju, Y. Zhao, J. Wan, Y. Zhu, Y. Qiang and Y. Qian, *Sci. Rep.*, 2016, **6**, 26146.
161. T. Kennedy, M. Brandon, F. Laffir and K. M. Ryan, *J. Power Sources*, 2017, **359**, 601-610.
162. T. Ma, X. Yu, H. Li, W. Zhang, X. Cheng, W. Zhu and X. Qiu, *Nano Lett.*, 2017, **17**, 3959-3964.
163. A. Toudjine, M. Morcrette, M. Courty, C. Davoisne, M. Lejeune, N. Mariage, W. Porcher and D. Larcher, *J. Electrochem. Soc.*, 2015, **162**, A1466-A1475.
164. M.-S. Song, G. Chang, D.-W. Jung, M.-S. Kwon, P. Li, J.-H. Ku, J.-M. Choi, K. Zhang, G.-R. Yi, Y. Cui and J. H. Park, *ACS Energy Lett.*, 2018, **3**, 2252-2258.
165. H. Wu, G. Chan, J. W. Choi, I. Ryu, Y. Yao, M. T. McDowell, S. W. Lee, A. Jackson, Y. Yang, L. Hu and Y. Cui, *Nat. Nanotechnol.*, 2012, **7**, 310.
166. X. Zhou, Y.-X. Yin, L.-J. Wan and Y.-G. Guo, *Chem. Commun.*, 2012, **48**, 2198-2200.
167. B. Xu, H. Wu, C. X. Lin, B. Wang, Z. Zhang and X. S. Zhao, *RSC Adv.*, 2015, **5**, 30624-30630.
168. S.-Y. Jang and S.-H. Han, *Sci. Rep.*, 2016, **6**, 38050.
169. N. Liu, Z. Lu, J. Zhao, M. T. McDowell, H.-W. Lee, W. Zhao and Y. Cui, *Nat. Nanotechnol.*, 2014, **9**, 187-192.
170. H. Wu, G. Chan, J. W. Choi, I. Ryu, Y. Yao, M. T. McDowell, S. W. Lee, A. Jackson, Y. Yang, L. Hu and Y. Cui, *Nat. Nanotechnol.*, 2012, **7**, 310-315.
171. A. Magasinski, P. Dixon, B. Hertzberg, A. Kvit, J. Ayala and G. Yushin, *Nature Materials*, 2010, **9**, 461-461.
172. M.-H. Park, M. G. Kim, J. Joo, K. Kim, J. Kim, S. Ahn, Y. Cui and J. Cho, *Nano Lett.*, 2009, **9**, 3844-3847.

173. L. Hu, H. Wu, S. S. Hong, L. Cui, J. R. McDonough, S. Bohy and Y. Cui, *Chem. Commun.*, 2011, **47**, 367-369.
174. H. Wu, G. Zheng, N. Liu, T. J. Carney, Y. Yang and Y. Cui, *Nano Lett.*, 2012, **12**, 904-909.
175. N. Liu, H. Wu, M. T. McDowell, Y. Yao, C. Wang and Y. Cui, *Nano Lett.*, 2012, **12**, 3315-3321.
176. W. Wang and P. N. Kumta, *ACS Nano*, 2010, **4**, 2233-2241.
177. R. Epur, M. Ramanathan, M. K. Datta, D. H. Hong, P. H. Jampani, B. Gattu and P. N. Kumta, *Nanoscale*, 2015, **7**, 3504-3510.
178. W. J. Lee, T. H. Hwang, J. O. Hwang, H. W. Kim, J. Lim, H. Y. Jeong, J. Shim, T. H. Han, J. Y. Kim, J. W. Choi and S. O. Kim, *Energy Environ. Sci.*, 2014, **7**, 621-626.
179. H. Chen, M. Zhou, Z. Wang, S. Zhao and S. Guan, *Electrochim. Acta*, 2014, **148**, 187-194.
180. M. Fang, Z. Wang, X. Chen and S. Guan, *Appl. Surf. Sci.*, 2018, **436**, 345-353.
181. S. L. Candelaria, B. B. Garcia, D. Liu and G. Cao, *J. Mater. Chem.*, 2012, **22**, 9884-9889.
182. Y. Zhai, Y. Dou, D. Zhao, P. F. Fulvio, R. T. Mayes and S. Dai, *Adv. Mater.*, 2011, **23**, 4828-4850.
183. L. Xiao, Y. H. Sehleier, S. Dobrowolny, H. Orthner, F. Mahlendorf, A. Heinzl, C. Schulz and H. Wiggers, *ChemElectroChem*, 2015, **2**, 1983-1990.
184. C. Martin, O. Crosnier, R. Retoux, D. Bélanger, D. M. Schleich and T. Brousse, *Adv. Funct. Mater.*, 2011, **21**, 3524-3530.
185. F. Hauquier, G. Pastorin, P. Hapiot, M. Prato, A. Bianco and B. Fabre, *Chem. Commun.*, 2006, 4536-4538.
186. E. Attia, F. Hassan, M. Li, D. Luo, A. Elkamel and Z. Chen, *J. Electrochem. Soc.*, 2019, **166**, A2776-A2783.
187. R. Raiteri, B. Margesin and M. Grattarola, *Sensors Actuators B: Chem.*, 1998, **46**, 126-132.
188. L. Zhang, W. Hao, H. Wang, L. Zhang, X. Feng, Y. Zhang, W. Chen, H. Pang and H. Zheng, *J. Mater. Chem. A*, 2013, **1**, 7601-7611.
189. D. C. Higgins, D. Meza and Z. Chen, *The Journal of Physical Chemistry C*, 2010, **114**, 21982-21988.
190. Z. Chen, D. Higgins, H. Tao, R. S. Hsu and Z. Chen, *The Journal of Physical Chemistry C*, 2009, **113**, 21008-21013.
191. C. Jingbo, H. Xingkang, Z. Guihua, C. Shumao, H. P. B., J. Junwei, H. P. T. and C. Junhong, *Adv. Mater.*, 2014, **26**, 758-764.
192. Y.-S. Hu, R. Demir-Cakan, M.-M. Titirici, J.-O. Müller, R. Schlögl, M. Antonietti and J. Maier, *Angew. Chem. Int. Ed.*, 2008, **47**, 1645-1649.
193. D. Higgins, Z. Chen and Z. Chen, *Electrochim. Acta*, 2011, **56**, 1570-1575.

194. W. J. Lee, D. H. Lee, T. H. Han, S. H. Lee, H.-S. Moon, J. A. Lee and S. O. Kim, *Chem. Commun.*, 2011, **47**, 535-537.
195. R. Czerw, M. Terrones, J. C. Charlier, X. Blase, B. Foley, R. Kamalakaran, N. Grobert, H. Terrones, D. Tekleab, P. M. Ajayan, W. Blau, M. Rühle and D. L. Carroll, *Nano Lett.*, 2001, **1**, 457-460.
196. K. Stańczyk, R. Dziembaj, Z. Piwowarska and S. Witkowski, *Carbon*, 1995, **33**, 1383-1392.
197. Z. Chen, D. Higgins and Z. Chen, *Carbon*, 2010, **48**, 3057-3065.
198. H. Wang, T. Maiyalagan and X. Wang, *ACS Catalysis*, 2012, **2**, 781-794.
199. Y. Zhang, W.-J. Jiang, L. Guo, X. Zhang, J.-S. Hu, Z. Wei and L.-J. Wan, *ACS Appl. Mater. Interfaces*, 2015, **7**, 11508-11515.
200. J. Guo, K. Song, B. Wu, X. Zhu, B. Zhang and Y. Shi, *RSC Advances*, 2017, **7**, 22875-22881.
201. C. Zou, C. Zhang, B. Li, S. Wang, Z. Xie and Y. Song, *Materials Science and Engineering A-structural Materials Properties Microstructure and Processing*, 2015, **620**, 420-427.
202. A. V. Korobeinyk, R. L. D. Whitby and S. V. Mikhalovsky, *Eur. Polym. J.*, 2012, **48**, 97-104.
203. M. S. A. Rahaman, A. F. Ismail and A. Mustafa, *Polym. Degrad. Stab.*, 2007, **92**, 1421-1432.
204. R. Janus, P. Natkański, A. Wach, M. Drozdek, Z. Piwowarska, P. Cool and P. Kuśtrowski, *J. Therm. Anal. Calorim.*, 2012, **110**, 119-125.
205. M. Thakur, S. L. Sinsabaugh, M. J. Isaacson, M. S. Wong and S. L. Biswal, *Sci. Rep.*, 2012, **2**, 795.
206. X. Hu, C. Shao, J. Wang and H. Wang, *J. Mater. Sci.*, 2017, **52**, 7555-7566.
207. X. Sun, H. T. Liu and H. F. Cheng, *RSC Advances*, 2017, **7**, 47833-47839.
208. M. Ge, Y. Lu, P. Ercius, J. Rong, X. Fang, M. Mecklenburg and C. Zhou, *Nano Lett.*, 2014, **14**, 261-268.
209. X. Wu, Z. Wang, L. Chen and X. Huang, *Electrochem. Commun.*, 2003, **5**, 935-939.
210. B. Liu, P. Soares, C. Checkles, Y. Zhao and G. Yu, *Nano Lett.*, 2013, **13**, 3414-3419.
211. X. Zhou, Y.-X. Yin, L.-J. Wan and Y.-G. Guo, *Chem. Commun.*, 2012, **48**, 2198-2200.

Appendix A

Supporting Information:

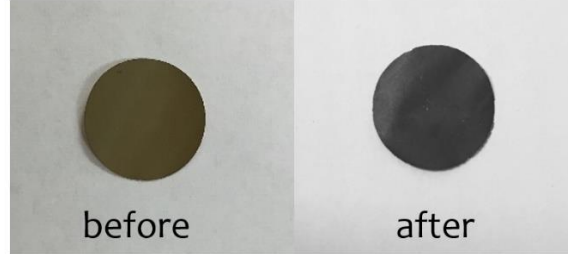


Figure (S4.1) Optical images of the Si electrode before and after SHT.

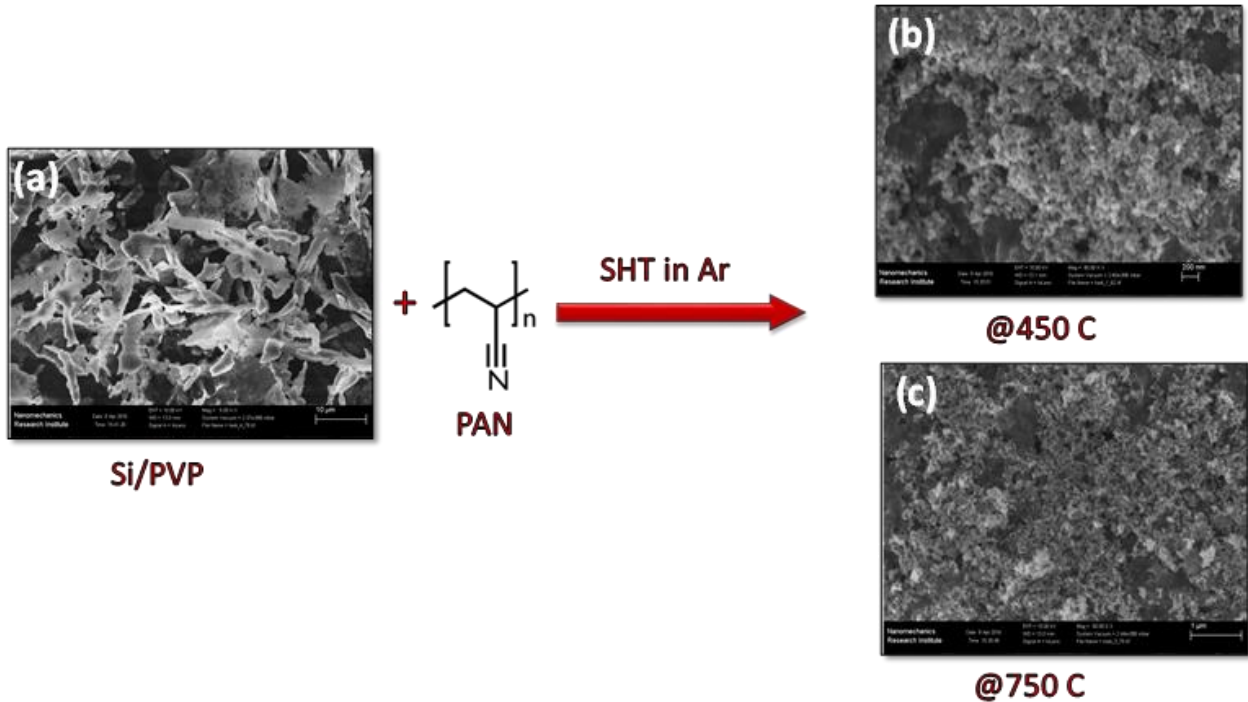


Figure (S4.2) (a) SEM image shows the SiNPs with PVP are embedded in the matrix of PVP polymer and self-assemble in a leaf morphology, (b) SEM image of the Si electrode treated at 450 °C shows the carbon layer shielding the SiNPs and forming breathable shell and their distribution around the SiNPs, and (c) SEM image of Si electrode treated at 750 °C shows the distribution of the carbon layers around the SiNPs.

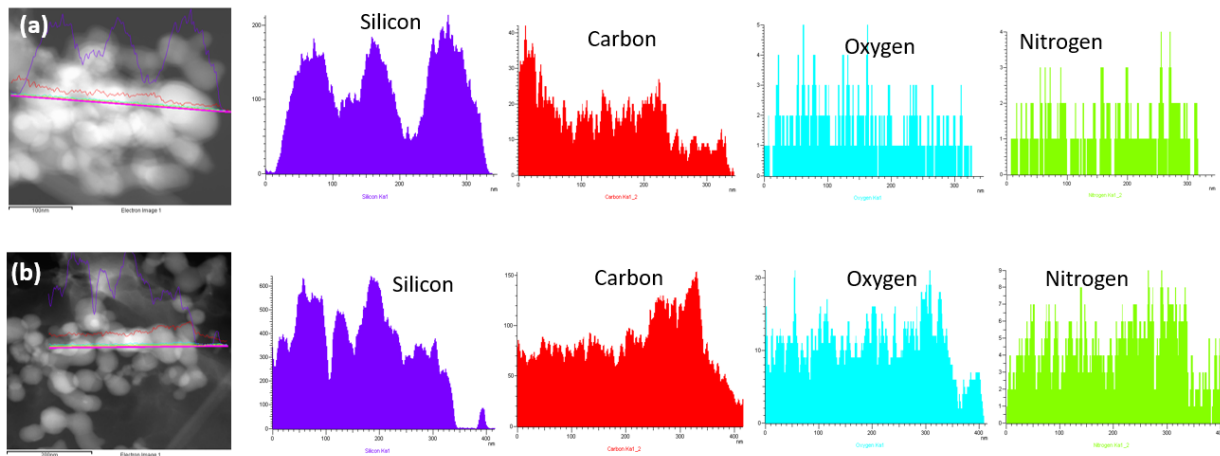


Figure (S4.3) HAADF-STEM across Si particles of the Si/PVP/g-PAN electrode with their associated EDS elemental line scan results across the Si particles as marked lines, (a) electrode treated at 450 C, (b) electrode treated at 750 C.

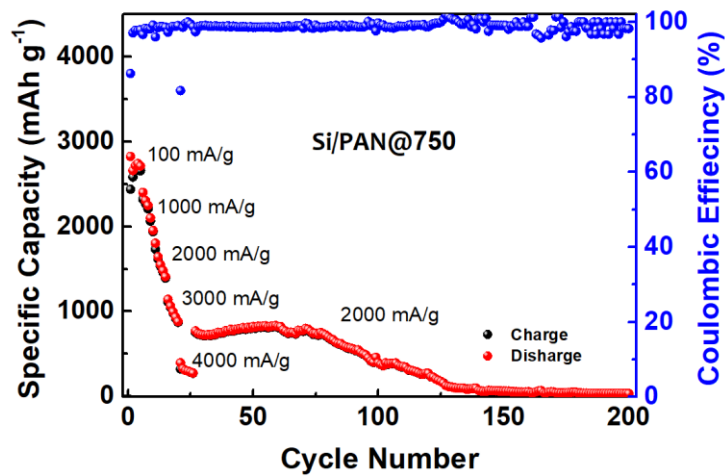


Figure (S4.4) Rate capability behavior of Si/PAN electrode without PVP treated at 750 °C.

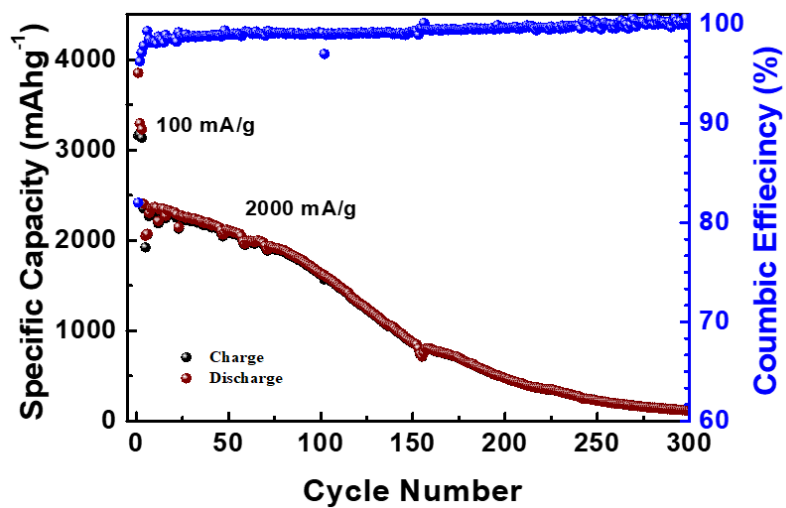


Figure (S4.5) Cycling behavior of Si/PVP electrode without PAN treated at 750 °C.

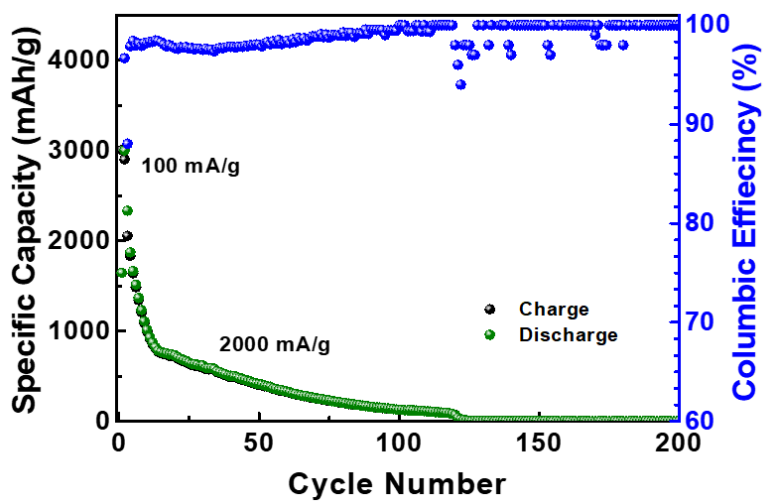


Figure (S4.6) Cycling behavior of Si/PVP/PAN electrode without SHT.

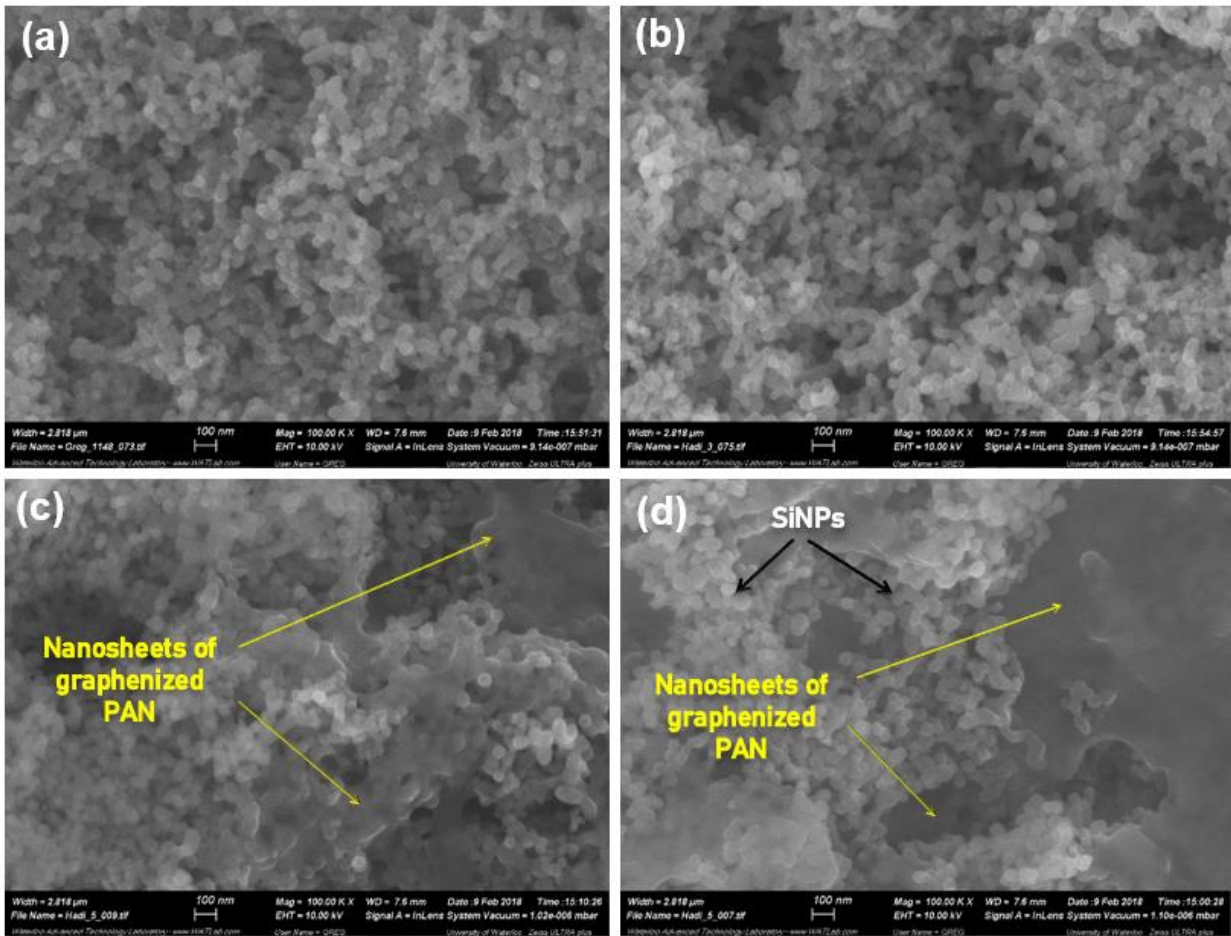


Figure (S5.1) SEM images of the Si electrode: (a) SiNPs coated by PAA/CMC copolymer after freeze drying, (b) SiNPs coated by the PAA/CMC/PAN before SHT, and (c, d) SiNPs after SHT wrapped by nanosheets of graphenized PAN (g-PAN).

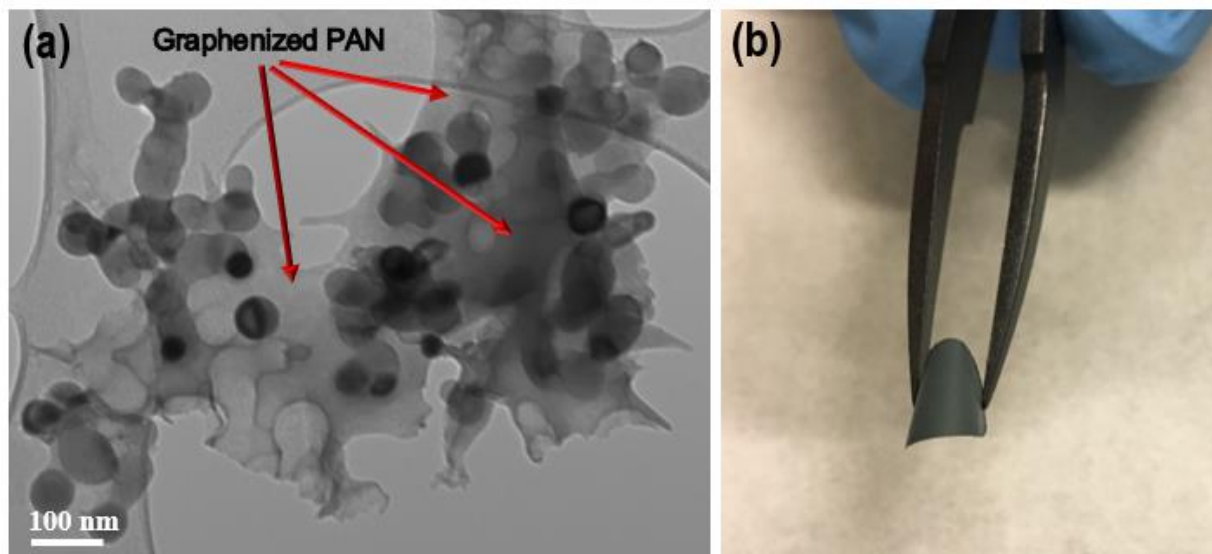


Figure (S5.2) (a) Low magnification TEM images of the NSi/PAA-CMC/g-PAN electrode treated at 450 °C showing a few Si particles well-wrapped by graphenized nanosheets and (b) digital image of the Si electrode after SHT. Even the electrode wound by lab tweezers, there is no any physical cracks are observed.

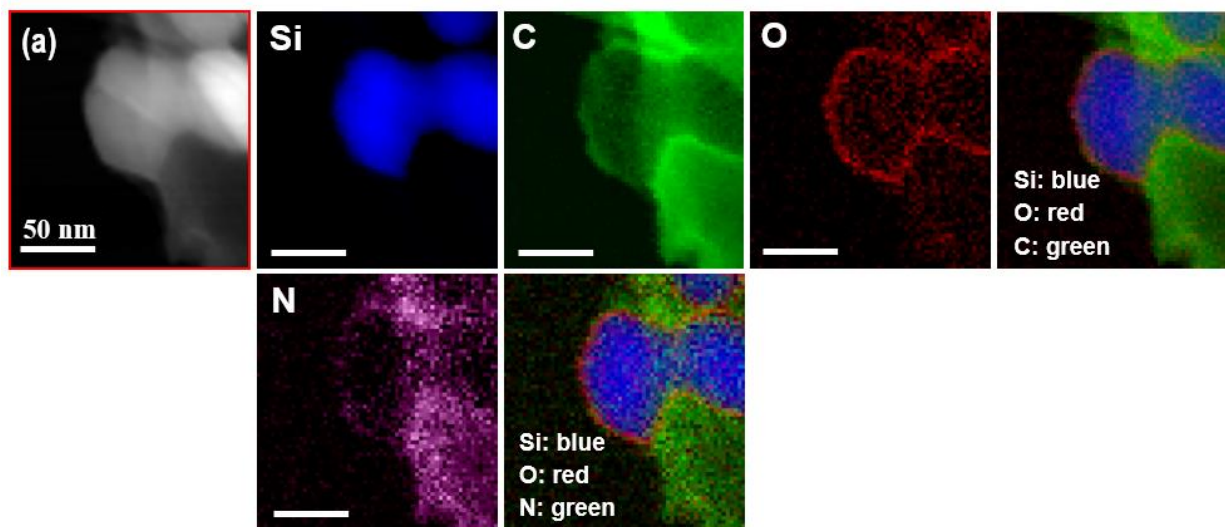


Figure (S5.3) (a) HAADF-STEM image of another electrode of NSi/PAA-CMC/g-PAN after SHT with its corresponding EELS mapping for (Si, C, O, N and overlap elements) for the image (a).

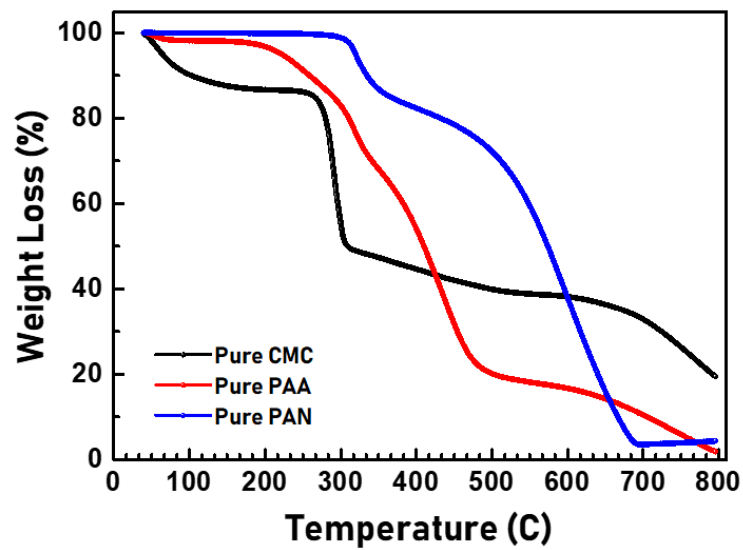


Figure (S5.4) Thermogravimetric analysis (TGA) curves analysis for pure PAN, pure CMC, and pure PAA in nitrogen atmosphere with a ramp rate of $10\text{ }^{\circ}\text{C min}^{-1}$.

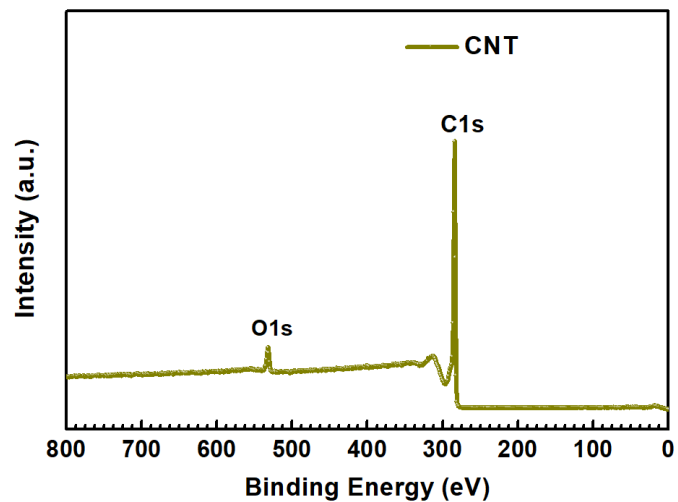


Figure (S6.1) XPS spectrum of CNT materials.

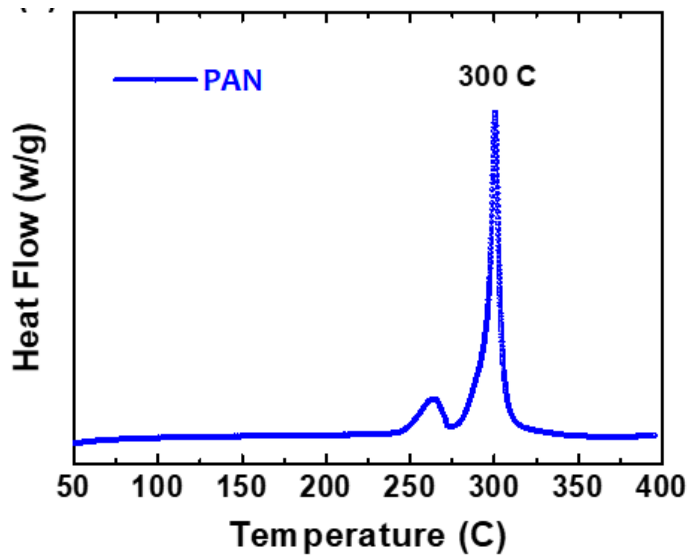


Figure (S6.2) DSC analysis for pure PAN in nitrogen showing a sharp peak at ~ 300 °C, which corresponding to the cyclization reaction of the nitrile group ($C\equiv N$) in PAN structure.

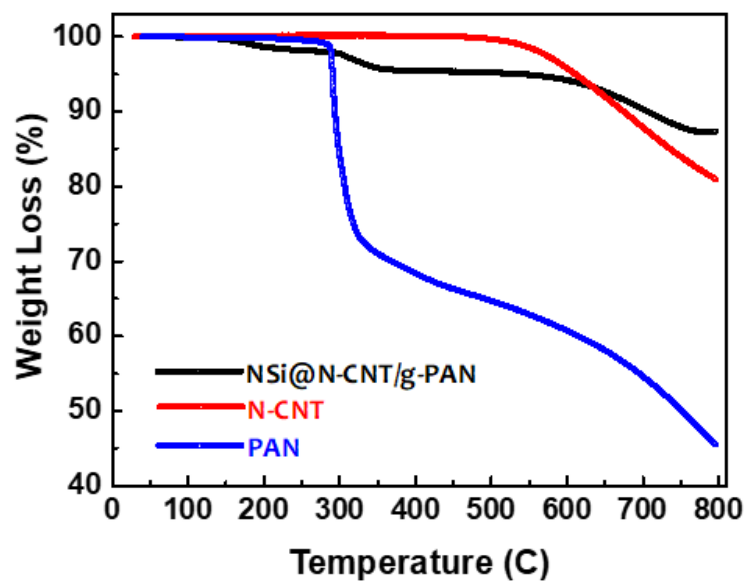


Figure (S6.3) Thermogravimetric analysis (TGA) curves of pure PAN, N-CNT, and NSi@N-CNT/g-PAN in nitrogen atmosphere with a ramp rate of 10 °C min⁻¹.

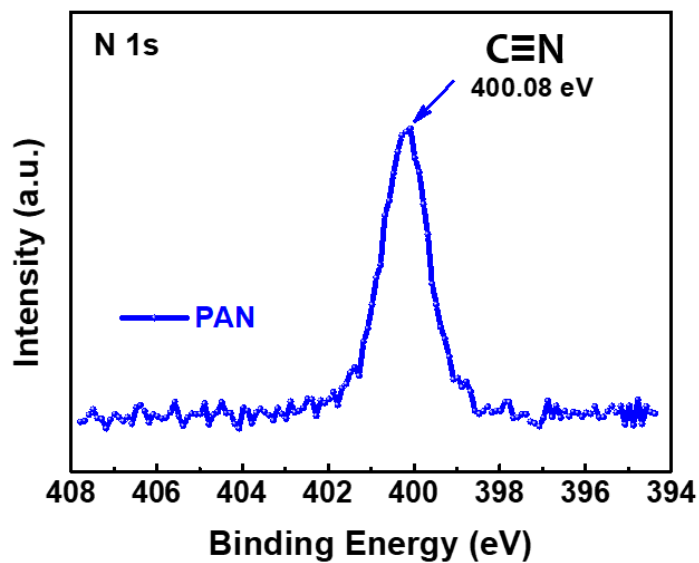


Figure (S6.4) high-resolution XPS of N 1s spectra of pure PAN showing the nitrile groups (C≡N) in PAN structure.

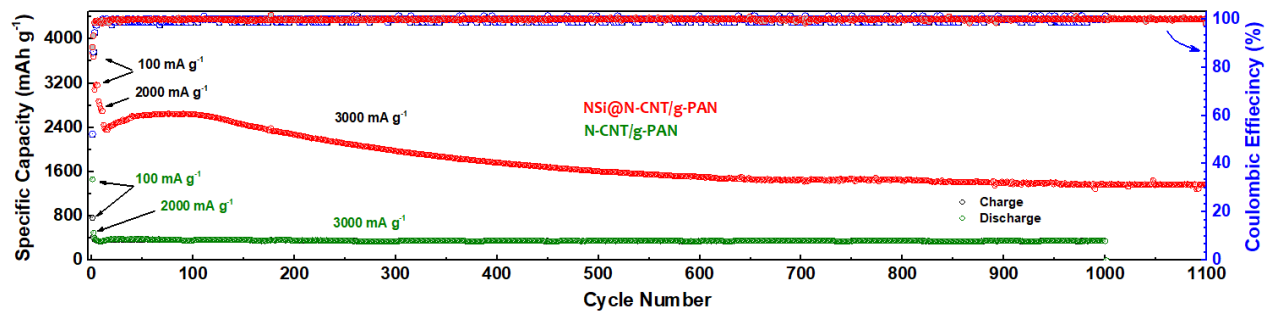


Figure (S6.5) Long cycling stability of the NSi@N-CNT/g-PAN electrode compared with N-CNT/g-PAN electrode cycled at the same current rates of 100, 2000 mA g⁻¹ for the first cycles then continued at 3000 mA g⁻¹.